# Mass Spectrometry with Hydrogen Plasma Driven Chemical Ionization for Investigating Atmospheric Processes

**Dissertation**

zur Erlangung des akademischen Grades

Doktor der Naturwissenschaften (Dr. rer. nat.)

Vorgelegt von

Md Fakrul Islam

Bergische Universität Wuppertal

Fakultät für Mathematik und Naturwissenschaften

Physikalische und Theoretische Chemie

Unter der Leitung von

Prof. Dr. Thorsten Benter

Wuppertal, April 2026

**Acknowledgement**

I would like to express my deepest gratitude to my supervisor, Prof. Dr. Thorsten Benter, and Dr. Hendrik Kersten, for their continuous support, patience, and insightful guidance throughout my PhD journey. Their expertise and encouragement have been invaluable to my research and professional growth.

I am also grateful to Dr. Ralf Kurtenbach, for his constructive feedback and critical insights that greatly enhanced the quality of this work.

I would like to express my gratitude to Prof. Dr. Peter Wiesen for his guidance throughout this study.

I am also grateful to Prof. Dr. Md. Mominul Islam, who was one of the driving forces behind the research and taught me so many things.

Special thanks to my lab colleagues at the Atmospheric Chemistry Research Lab for their cooperation and technical assistance over the years.

On a personal note, I am deeply thankful to my parents and family, especially to my beloved wife, for her unwavering love, patience, and encouragement throughout this long journey.

## Abstract

This thesis presents the development, optimization, and analytical characterization of a hydrogen plasma driven chemical ionization (HPCI) source integrated into a triple quadrupole mass spectrometer (TQ MS) for the soft ionization of atmospheric relevant trace gases. The work addresses the limitations of classical filament based EI/CI sources—short filament lifetimes in oxygen rich matrices, elevated source temperatures, and extensive fragmentation—by replacing the filament with a low power helical resonator hydrogen plasma operated at 1 – 15 mbar. Hydrogen is used to generate $H_3^+$ as a primary reagent ion, which is converted into secondary reagents such as $N_2H^+$ and $H_3O^+$ by controlled admixtures.

A central part of the study is the systematic optimization of the plasma gas composition, pressure, and flow, as well as the conductance of the reaction chamber and the plasma source distance (PSD) relative to the reaction chamber. Using combined mass spectrometric and optical (UV–NIR) diagnostics, an optimum $N_2$ fraction of 9 – 12% in $H_2$ and plasma gas flows around 5.5 – 6.5 sccm were identified, maximizing $N_2H^+$ formation at reaction chamber pressures near 8 mbar while suppressing parasitic $NH_4^+$ formation via heterogeneous $NH_3$ chemistry. Reactant ion losses due to wall interactions in the glass transfer tube were quantified by varying PSD, analyte inlet position, and transfer line temperature, demonstrating that short ion paths, co localized reactant and analyte beams, and low transfer line temperatures favor high protonation efficiency.

The ionization behavior of aromatic compounds (benzene, toluene, o xylene, BTX) with $N_2/H_2$ reagent gas is governed by proton transfer from $N_2H^+$ and $H_3O^+$, complemented by charge transfer and VUV driven photoionization from $O_2^+$ and plasma emission. At optimized conditions, BTX yields comparable fractions of $MH^+$ and $M^+$, with fragmentation ($(M(–H)^+$, $M(–CH_3^+)$) largely controlled by the excess energy of $H_3^+$ and $N_2^+$ reactions, enabling soft but sensitive detection. Full scan (FS) and selected ion monitoring (SIM) measurements show that SIM profile data enhance sensitivity by roughly two orders of magnitude, yielding $MH^+$ sensitivities up to $2.4 \times 10^5$ cps/ppbV and LODs of 3–7 ppbV for BTX.

Small oxygenated VOCs could not be measured satisfactorily with $N_2/H_2$ alone, and a methanol/synthetic air dopant was therefore introduced to generate $CH_3OH_2^+$ and methanol clusters as tailored reactants. This enabled adduct ion formation $M{\cdot}CH_3OH_2^+$ for ethanol, iso propanol, and n butanol, with linear calibration and ppbV level LODs for multi carbon alcohols,

as confirmed by CID experiments in Q2. Detailed background studies revealed that high voltage Penning gauges and dopant related cluster signals dominate noise at critical m/z values, and the instrument must be operated with the Penning gauge off and with carefully chosen reagent conditions to achieve optimal performance. Overall, the HPCI TQMS system is shown to be a practical, filament free alternative to classical CI, capable of soft and sensitive analysis of aromatic and oxygenated compounds under atmospheric like conditions.

# Contents

*List of Figures*

*List of Tables*

**List of abbreviations**

| | |
|---|---|
| APCI | atmospheric pressure chemical ionization |
| API-TOF | atmospheric pressure interfaced time-of-flight |
| BTX | mixing of benzene, toluene and xylene |
| CC | collision cell |
| cf | refer to |
| CI | chemical ionization |
| CID | collision induced dissociation |
| CIMS | chemical ionization mass spectrometry |
| cps | count per second |
| DL | Debye length |
| EI | electron ionization |
| FI | field ionization |
| GB | gas phase basicity |
| GC | gas chromatography |
| GC-MS | gas chromatography mass spectrometry |
| HR | helical resonator |
| HPCI | hydrogen plasma-driven chemical ionization |
| HIA | hydride ion affinity |
| ICP | inductively coupled plasma |
| LOD | limit of detection |
| log | logarithmic |
| M | molecular ion |
| MeOH | methanol |
| mm | millimeter / $10^{-3}$ meter |
| MS | mass spectrometry |
| ms | millisecond / $10^{-3}$ second |
| mTorr | millitorr ( 1mTorr = 1.33 mbar) |

| | |
|---|---|
| m/z | mass-to-charge ratio |
| nm | nanometer / $10^{-9}$ meter |
| norm. | normalize |
| PA | proton affinity |
| PG | plasma gas |
| PID | photoionization detector |
| PS | plasma source |
| PSD | plasma source distance |
| PTFE | polytetrafluoroethylene |
| RF | radio frequency |
| sccm | standard cubic centimeter per minute |
| SA | synthetic air |
| SIP | sample inlet position |
| TIC | total ion current |
| TQ-MS | triple quadrupole mass spectrometry |
| TOF-MS | time-of-flight mass spectrometry |
| WL | wavelength |
| VUV | visible and ultraviolet |

# 1 Aim of this work

Mass spectrometry (MS) is a technique that can analyze a wide range of compounds based on their m/z charge ratio. The common ionization method of MS, electron ionization (EI) at 70 eV, has been developed with high ionization efficiency. This high-energy EI ionization often results in substantial fragmentation. Therefore, fragile analytes might not be unambiguously detected and the increasing complexity of mixtures might not be deconvoluted without prior chromatographic separation. However, unstable compounds in atmospheric conditions are very essential to be identified without fragmentation and separation to further understand atmospheric processes. To address the limitation of the EI sources, various soft ionization techniques, such as soft EI [1,2] and chemical ionization (CI) [3], have been introduced. According to the literature on classical CI sources, a reagent gas is used in an ionization chamber and maintains chamber pressure of approximately 1 mbar. Accelerated electrons from a heated filament primarily ionize the reagent gas, which subsequently transfers charges to the analytes. However, the significant limitation of filament-based ion sources is that they experience a reduction in lifespan when operated in an elevated oxygen atmosphere, which is always the case when atmospheric samples are being introduced [4,5]. Consequently, the filament necessitates routine cleaning and system maintenance, which are time-consuming procedures owing to the necessity of venting the system prior to shutdown and awaiting the ion source to attain ambient temperature. Moreover, the applied power to the filament increases the chamber temperature, which may often lead to fragmentation. It was reported that the filament-based ion source was replaced with the Townsend ion source [6] and the glow discharge ion source [7], which were not accepted as CI methods. However, a helical resonator radio frequency hydrogen-driven plasma chemical ionization (HPCI) source was introduced and integrated into the GC-TOFMS by Bräkling *et al.* [8] Hydrogen gas is used to generate $H_3^+$ reactant ions, and secondary reactant ions may also be produced, depending on the proton affinity (PA) of the molecules. Hence, molecules with lower PA can protonate molecules with higher PA. Building on this concept, the HPCI source was introduced into a Gas Chromatography triple quadrupole mass spectrometer (GC-TQ-MS) system by Mr. Sackmann in his master's thesis [9] to investigate hydrocarbons. The aim of this work is to optimize the HPCI source for a (TQ-MS) and investigate atmospheric samples using HPCI-TQ-MS, without fragmentation.

# 2 Introduction

## 2.1 Chemical Ionization

Ionization is a fundamental step of the MS system that transforms neutral atoms or molecules into charged species (ions). This process of a sample can be affected not only by electrons, but also by (atomic) ions or photons, energetic neutral atoms, and electronically excited atoms [10]. A variety of ionization techniques, depending on applications, have been developed to analyze a wide range of neutral molecules. EI is commonly used for the ionization of compounds for mass analysis in MS systems.

The EI source in mass spectrometry emits electrons thermionically from a high-resistivity filament in high-vacuum conditions. The EI ionization process achieves its highest efficiency at an electron energy of 70 eV [11]. These high-energy electrons generate a wide variety of ion types (molecular ions, fragment ions, multiply charged ions, metastable ions and rearrangements) [12]. Due to the degree of fragmentation associated with 'hard' ionization processes, the molecular ion can disappear [13]. One effective method to minimize the fragmentation of molecular ions is to lower the electron energy from the standard 70 eV to 12–15 eV [1,2]. However, this reduction in electron energy also leads to a decreased ionization efficiency [13]. Due to these reasons, other “soft” ionization techniques such as field ionization (FI) [14,15], CI [3], photo ionization (PI) [16,17], atmospheric pressure chemical ionization (APCI) [18], helical resonator plasma chemical ionization (HRPCI) [8] (cf. *section 2.5*) have been introduced. Chemical ionization mass spectrometry is used to analyze gas-phase molecules by inducing ionization via a gas-phase ion-molecule reaction using selected reagent ions.

The CI technique may involve the transfer of an electron, proton, or other ions between the reactants [19], and the neutral analyte, M. The reagent ions $BH^+$ are generated from the reagent gas [20]. The possible ion-molecule reactions within positive ion chemical ionization (PICI) [11] are as follows:

| | | | | | | | | |
|---|---|---|---|---|---|---|---|---|
| M | + | $BH^+$ | → | $MH^+$ | + | B | *proton transfer* | (*Rn 1*) |
| M | + | $B^+$ | → | $MB^+$ | | | *electrophilic addition* | (*Rn 2*) |
| M | + | $B^+$ | → | $M(-A)^+$ | + | AB | *anion abstraction* | (*Rn 3*) |
| M | + | $B^+$ | → | $M^+$ | + | B | *charge transfer* | (*Rn 4*) |

In the reaction, M, B, and A are molecules, reagents, and anions, respectively.

However, the proton transfer reaction, no *Rn 1*, is the common ionization reaction in PICI. The reagent ion has to act as a Brønsted acid [11]; consequently, proton transfer yields protonated analyte molecules, $MH^+$. In the electrophilic reaction *Rn 2*, the analyte molecule may receive a charge by adduct formation via electrophilic addition. Electrophilic addition of $B^+$ occurs by attachment of the entire reagent ion to an analyte molecule if protonation of M is not feasible. For example, $(M+NH_4)^+$ ions are often formed when ammonia reagent gas is used. Thus, even-electron ions are detected at an m/z value above M, the exact position of which depends on the adduct actually formed. In the reaction *Rn 3*, the hydride abstraction is a commonly occurring case of anion abstraction, e.g., aliphatic alcohols rather yield $M(–H)^+$ ions, $M^+$, than $MH^+$ ions [21,22]. The hydride abstraction may become dominant when the hydride ion affinity (HIA) of $B^+$ is greater than the HIA of $M(-A)^+$. The HIA of a gaseous cation $B^+$ is defined as the negative enthalpy change for the hydride transfer reaction. Charge transfer (CT), also known as charge exchange (CE), it yields molecular ions, $M^+$, i.e., odd-electron species. Although being positive radical ions, the products of charge transfer (*Rn 4*) tend to provide notably less fragmentation than those formed upon electron ionization, because the average ion internal energy from CT is much lower than after EI.

## 2.2 Thermodynamics of Proton Transfer Reactions

The reactant ion in chemical ionization is protonated to produce an analyte, depending on its gas-phase basicity (GB) and proton affinity (PA) [11]. The reaction *Rn 1* in previous section describes the proton transfer from the donor ion to the neutral molecules. In this reaction, the donor ion $BH^+$ transfers a proton to the molecule M with an overall change in Gibbs free energy $\Delta G$. This quantity essentially determines the direction of this process. In case of a negative value, the reaction proceeds as shown in *Rn 1*. In order to calculate $\Delta G$ for a potential proton donor and acceptor pair, the gas-phase basicities GB for many compounds are listed in databases. GB is simply the negative change in Gibbs free energy for the hypothetical reaction

$$M_{(g)} + H^+_{(g)} \rightarrow MH^+_{(g)} \qquad (Rn\ 5)$$

$$GB_{(M)} = -\Delta G^0_{(Rn\ 5)} \qquad (1)$$

Therefore, comparing the gas-phase basicity values in these lists for two compounds provides an unambiguous thermodynamic measure for the direction a protonation reaction proceeds. In other words, it allows to find suitable compounds to be used as the reagent gas for protonating neutral molecules of interest.

A second important thermodynamic quantity is the proton affinity of a molecule, defined as the negative of the enthalpy change $-\Delta H$ for the reaction *Rn 5* [23,24].

$$PA_{(M)} = -\Delta H^0 \qquad (2)$$

Hence, the proton affinity is directly related to the exothermicity of a protonation event and allows to determine the excess energy potentially remaining in the products. The larger the difference of PAs between reagent and neutral molecule, the more excess energy will potentially remain in the vibrational degrees of freedom of the protonated analyte and cause its fragmentation. On the other hand, choosing a reagent gas with a high proton affinity to minimize the $\Delta PA$ between reagent and analyte, lowers the amenable range of compounds to be ionized by this particular reagent thus increasing the selectivity. Therefore, a chemical ionization method with a certain reagent is always a balance between excess energy potentially causing fragmentation and its selectivity.

The relation between the PA and GB is given by the Gibbs-Helmholtz equation

$$PA_{(M)} = GB_{(M)} + T\Delta S^0 \qquad (3)$$

The term for the entropy change $T\Delta S^0$ of a protonation reaction is generally relatively small [11], so that in most cases only the proton affinity differences are considered for the evaluation of the excess energy *and* the direction of the protonation. Thus, in good approximation, a neutral molecule with a higher proton affinity can effectively be protonated by an ion originating from a species with a lower proton affinity.

$$PA\ (M) > PA\ (B) \tag{4}$$

*Table 1* lists compounds with their respective nominal mass, PA, GB values, and ionization energy, relevant for this work. Shown are also the respective reactant ions, the neutral nominal mass and the ionization energies.

*Table 1: Proton affinity and gas phase basicity of common reagents* [25,26]

| **Reagent gas/ analyte** | **Reactant ion** | **Nominal mass** | **PA [kJ·mol⁻¹]** | **GB [kJ·mol⁻¹]** | **Ionization energy [eV]** |
|---|---|---|---|---|---|
| $O_2$ | --- | 32 | 421.0 | 396.3 | 12.07 |
| $H_2$ | $H_3^+$ | 2 | 422.3 | 394.7 | 15.43 |
| $N_2$ | $N_2H^+$ | 28 | 493.8 | 464.5 | 15.58 |
| $CH_4$ | --- | 16 | 543.5 | 520.6 | 12.61 |
| $H_2O$ | $H_3O^+$ | 18 | 691.0 | 660.0 | 12.62 |
| $C_6H_6$ (benzene) | --- | 78 | 750.4 | 725.4 | 9.24 |
| $CH_3OH$ (methanol) | $CH_3OH_2^+$ | 32 | 754.3 | 724.5 | 10.84 |
| $C_2H_5OH$ (ethanol) | --- | 46 | 776.4 | 746.0 | 10.48 |
| $C_3H_7OH$ (propanol) | --- | 60 | 786.5 | 756.1 | 10.22 |
| $C_6H_5CH_3$ (toluene) | --- | 92 | 784.0 | 756.3 | 8.83 |
| $C_4H_9OH$ (n-butanol) | --- | 74 | 789.2 | 758.9 | 9.99 |
| o-$C_6H_4(CH_3)_2$ (o-xylene) | --- | 106 | 796.0 | 768.3 | 8.56 |

## 2.3 Kinetics of Proton Transfer

Proton transfer is an important class of ion–molecule reactions with a range of analytical applications in MS [27,28]. In reaction *Rn 1*, this process is thermodynamically favorable when the PA of M surpasses that of the reactant ion. The rate of $[MH]^+$ formation

$$\frac{d\,[MH]^+}{dt} = k \cdot [M] \cdot [BH]^+ \tag{5}$$

usually proceeds rather fast, given that the overall and partial pressures of M and $BH^+$ still provide collisional dominated conditions. The reaction rate constant k for these kind of reactions falls within the range of $10^{-9}$ $cm^3 \cdot s^{-1}$ [13,29]. Due to ion-induced dipole contributions, this constant is up to one order of magnitude larger than the gas kinetically derived constant for a collisional limited process of purely neutral particles. Under typical chemical ionization conditions, the concentration of the neutral analyte molecules [M] is higher than that of the reactant ion $[BH]^+$. However, experimental conditions providing short reaction times, allow to keep the concentration of *both* reactants and thus the rate of the reaction quasi constant. In numerous analytical applications, this provides a means of quantitatively measuring gas phase concentration of analytes by a simple relation between the reaction time t, reaction rate constant k and the intensities of $[MH]^+$ and $[BH]^+$, such as in PTR[30].

## 2.4 Plasma

The term “plasma” was first introduced by the Czech physiologist J.E. Purkinje in the middle of the nineteenth century [31] to describe the liquid and cell-free part of blood. In the 20´s of the 20th century Irving Langmuir also used this term for “a quasi-neutral gas consisting of charged particles that exhibit collective behavior” [32]. In the latter system, collective behavior refers to how a plasma responds to external forces or disturbances due to the interactions of its charged particles. These particles influence each other’s momentum through electric (Coulomb force) and magnetic fields (Lorentz force). One important measure for this collective behavior and thus for defining an ionized gas as a plasma is the Debye length (DL). The equation of Debye length,

$$\lambda_D \approx 743 \sqrt{\frac{T_e}{n_e}}\ \text{(cm)} \tag{6}$$

It relates the electron density ($n_e$) and electron temperature ($T_e$) with basically the mean length at which the coulomb force of an additional positive charge has dropped to 1/e.

A plasma is a highly dynamic system. Electrons and ions rapidly recombine or diffuse towards walls and become neutralized. This loss of charges necessitates a constant energy supply to facilitate an equally fast ionization rate and maintain the plasma state. The gas can either be heated in a classical way, thermally increasing the energy among all the degrees of freedom inside the gas. At a sufficiently high temperature, some molecules/atoms also decompose into freely moving charged particles (electrons and positive ions) and the gas enters the plasma state. This is called a *hot* plasma and is characterized by an equilibrated temperature between the neutral particles (T), the ion temperature ($T_i$) and the electron temperature ($T_e$), $T_e = T_i = T$. This mechanism made plasmas also known as the *fourth state of matter*, in line with changing from solid to liquid and gas in the order of increasing temperature. The temperatures required to form plasmas from pure substances in thermal equilibrium start at roughly 4000 K (0.345 eV) for easy-to-ionize elements.[33] Our sun is the most famous example for this kind of plasma.

Due to three orders of magnitude higher inertia of positive ions, it is also possible to increase the temperature of electrons separately. This leads to *cold* plasmas, at which $T_e >> T_i \approx T$. Depending on a multitude of parameters, such as gas type and gas pressure, various electric and magnetic field driven setups can be applied to accelerate electrons without significantly raising the gas temperature. Fast electrons then initiate EI once their kinetic energy exceeds the ionization energy of the gas constituents, which typically range between 10 and 25 eV.

In this work, a helical resonator (HR) was used to sustain a cold, low-pressure plasma with hydrogen as the main gas constituent at approximately 1 mbar. A coil with roughly 120 windings surrounds a glass tube of 12.7 mm outer diameter, which feeds the plasma gas. An alternating current with 13.56 MHz frequency is supplied to the coil. This drives an alternating magnetic field inside the tube, inducing an alternating electrical field concentrically around the tube axis. Free electrons follow those induced electrical field lines in a helical way, collide with neutral species at the edge of the plasma zone and maintain the balance between the ionization and the charge loss rate. Since the driving mechanism is an induced electrical field, this type is also referred to as an inductively coupled plasma (ICP). These discharges are characterized by mean electron temperatures of $T_e \approx 1–10$ eV and charge densities of $n_i \approx n_e \approx 10^8–10^{13}$ $cm^{-3}$ [33].

## 2.5 Hydrogen Plasma-driven Chemical Ionization

Chemical ionization is a technique used in mass spectrometry to ionize molecules for analysis. The process involves generating reactive ions in large excess that can then transfer protons to sample molecules, causing them to become charged and detectable by the mass spectrometer.

Historically, this was achieved using filament-based CI sources, a method pioneered in the 1950s and 1960s by Talrose [34] and Munson and Field [3,35], respectively. However, these traditional sources have a significant drawback: the filaments degrade quickly in the presence of oxygen containing samples, leading to frequent maintenance and downtime. Due to these limitations, our research group, within the Department of Physical and Theoretical Chemistry at the University of Wuppertal, introduced a helical resonator plasma chemical ionization source (HRPCI) [8,13,36–38]. The HRPCI source was integrated in an atmospheric pressure interfaced time-of-flight (API-TOF) mass analyzer, in cooperation with TOFWERK, Thun, Switzerland and is now commercially available.

The HR plasma source uses hydrogen as the plasma gas to generate $H_3^+$ ions as the primary species [38] according to:

$$H_2 + e^- \rightarrow H_2^+ + 2e^- \qquad (Rn\ 6)$$

$$H_2 + H_2^+ \rightarrow H_3^+ + H^\cdot \qquad (Rn\ 7)$$

The proton in reaction Rn 7 from $H_2^+$ transfers to the neutral $H_2$ and produces $H_3^+$ by proton transfer reaction as described in *section 2.2 Thermodynamics of Proton Transfer Reactions* in the reaction *Rn 1*. The proton affinity of $H_2$ is 422.3 kJ·mol$^{-1}$ [26], a rather low value, meaning $H_3^+$ is a strong gas-phase acid that readily transfers a proton to a wide variety of other molecules, making it ideal for the analysis of many different chemical compounds. Since the lower PA can protonate the higher proton affinity reagent, the further reactant gas has to be selected accordingly. Any compound with a higher proton affinity than hydrogen can be used in theory. A new PG, by mixing hydrogen with another gas, can produce secondary ions to enhance the measurement range of the mass spectrometer. Nitrogen was found as a promising second reagent gas to readily form $N_2H^+$ [39–41]. In the final step, the analyte is introduced, protonated, and subsequently directed to the mass analyzer for measurement.

The successful formation of reagent ions requires careful control of several dependent parameters, including gas flow, gas mixture composition, plasma source pressure, and the purity of the plasma gases. Such optimization is crucial, as minor variations in these parameters can significantly affect reactant ion distributions, plasma density, and ion–molecule reaction rates [38].

# 3 Experimental

## 3.1 GC-FID Mass Spectrometer

A mass spectrometer, model SCEVOQ GC-TQ, from Bruker Corporation, USA, was interfaced with a GC-FID system. The MS system is a triple-quadrupole (TQ-MS), comprising four quadrupoles designated as Q0, Q1, Q2, and Q3 (cf. *Figure 3.1*). Q0 functions as an ion collimator and operates with radio frequency (RF) voltage alone, thereby focusing and transmitting ions into the subsequent quadrupoles. Both Q1 and Q3 function as mass filters through the application of combined RF and direct current (DC) voltages. Additionally, Q3 can serve as an ion guide to the detector when operated with RF voltage alone. Q2 operates as a collision cell, in which collision-induced dissociation (CID) or tandem mass spectrometry (MS/MS) experiments are performed by elevating the cell pressure and introducing an inert collision gas, typically argon, in conjunction with externally applied collision energy. The precursor ion of interest is first filtered in Q1 and subsequently accelerated into Q2, where it undergoes fragmentation upon collision with the CID gas. The resulting product ions are then directed into Q3, where a selected range of m/z ratios is scanned prior to detection. This sequence of operations corresponds to product ion scan mode. In addition to this mode, full scan (FS) and selected ion monitoring (SIM) modes were also employed. In FS mode, a defined m/z range is scanned in either Q1 or Q3 to generate a comprehensive mass spectrum of the sample. Conversely, SIM mode targets a limited number of ions (up to ten) by selecting their m/z values in Q1 or Q3, thereby enhancing sensitivity for the analytes of interest.

The GC-FID system enables the separation and characterization of complex mixtures, typically hydrocarbon-based samples. The sample line, after passing through the GC column, splits into two streams: one directed to the FID and the other to the mass spectrometer. This configuration permits simultaneous analysis of identical samples using both GC-FID and GC-MS techniques. The sample transfer line of the MS system can be adjusted to an appropriate temperature (from ambient to 350 °C) to prevent the loss (such as condensation) of analytes. The samples from the GC system are ionized with the filament-based EI/CI method and analyzed without any issues. However, for investigating samples including unstable compounds in atmospheric processes it is essential to also allow for direct sampling at ambient conditions. Therefore, an additional sample line has been connected in parallel with the sample line from the GC system to the MS system (cf. *Figure 3.1*). Consequently, the system can analyze either a VOC sample

from the GC system or a direct atmospheric sample from an external sample line. However, in this study, the GC system was disconnected, and only the atmospheric sample has been introduced to the MS system using the external sample line. It was observed that measuring atmospheric samples using a filament-based ion source has faced significant challenges, such as reduced lifespan of the ion source and extensive ion fragmentation. Due to these limitations of the measurement of samples from atmospheric conditions, the original ion source has been modified by a helical resonator-driven HPCI source (cf. *details in section 3.3*) into the MS system. This HPCI source was introduced to the TQ-MS system by Mr. Sackman for analyzing hydrocarbons (*addressing fragmented ions*) at atmospheric conditions [9]. Further experiments are continuing in this study to optimize the HPCI source and analyze atmospheric samples without/less fragmentation.

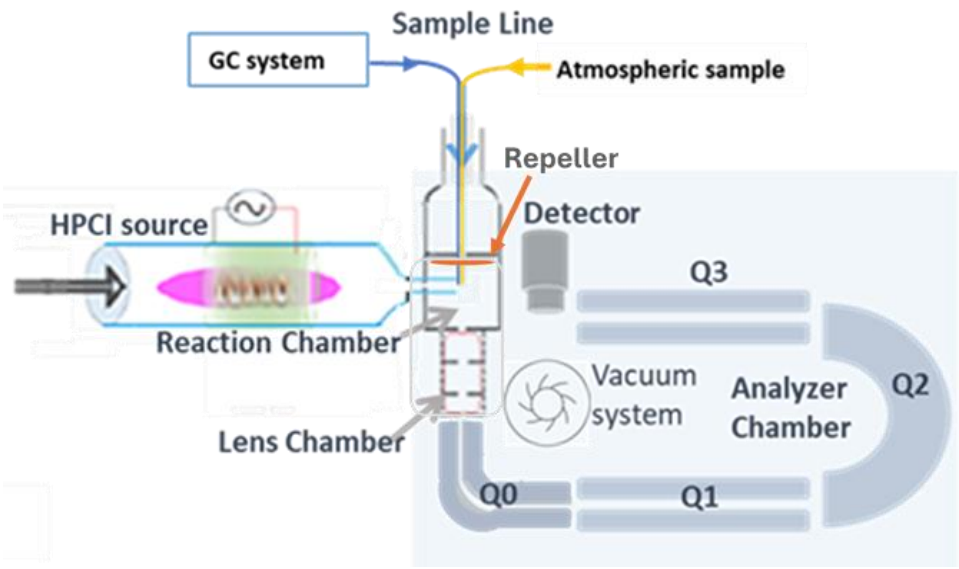


*Figure 3.1: Schematic diagram of HPCI source integrated into the Bruker EVOQ triple quadrupole mass spectrometer (TQ-MS)*

The original ionization source of this MS system is filament-based EI/CI. The EI source volume (in this work termed "reaction chamber") has a rather high conductance and comprises two filaments on the outside. In contrast, the CI volume comprises only one filament and is more enclosed to maintain higher pressures of the reagent gas. Since the HPCI is a CI source, a similar source volume has been manufactured by our university workshop. The hole in the reaction chamber for the filament-based CI source has a diameter of 0.7 mm. However, the diameter of the HPCI glass tube (inlet to the reaction chamber) is approximately 4.0 mm.

Consequently, a hole measuring approximately 4.7 mm has been created in the reaction chamber to serve as the inlet for the glass tube. The reaction chamber size is 10 mm in length with 12 mm OD. Following the reaction chamber, there are two other chambers, denoted as the lens chamber and analyzer. Ions and neutral species are introduced to the lens chamber from the reaction chamber. Only positive ions are accelerated from the lens chamber to the analyzer chamber, all other species are pumped away from the system. The positive ions are filtered by the mass filter Q1 or Q3 within the required range and accelerated to the electron multiplier detector. The ions, except for the selected range of m/z, are pumped away by the turbo molecular pump.

## 3.2 Vacuum System

The EVOQ GC-TQ system employs a vacuum configuration designed to sustain optimal operating pressures across its components. The vacuum assembly comprises two stages: a pre-vacuum (roughing) pump (model DUO 3, Pfeiffer Vacuum GmbH, Germany), operating pressure $<10^{-3}$ mbar, and a turbomolecular pump (model TW 400-300, Leybold, Germany) with an operating pressure range of $10^{-5}$-$10^{-7}$ mbar [42].

In the original mass spectrometer configuration, the vacuum pressure was not monitored. Following the replacement of the electron ionization source with the high-pressure chemical ionization (HPCI) source, continuous monitoring of pressure has become essential due to the pressure-dependent nature of the HPCI source, as well as the associated chamber conditions. Consequently, two pressure gauges (PG-1 and PG-2) were installed (cf. *Figure 3.2*) to monitor the pressures within the analyzer, lens, and reaction chambers.

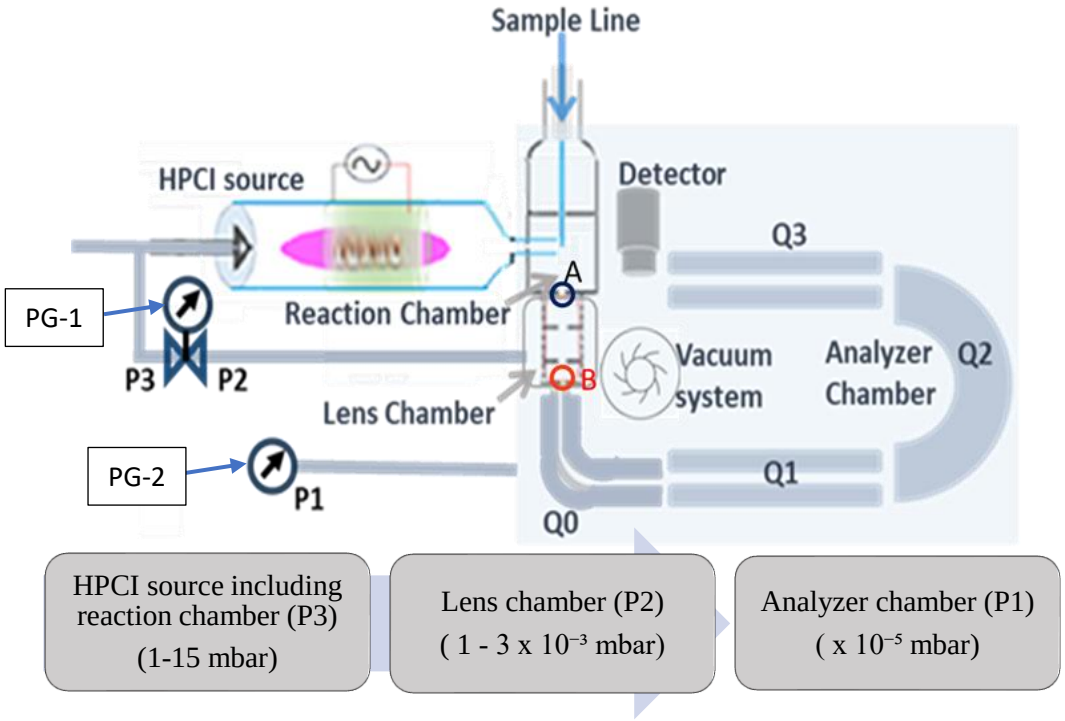


*Figure 3.2: Pressure measurement setup of the mass spectrometer. The reaction chamber is part of the HPCI source. "A" is an aperture restricting gas flow from the reaction chamber to the lens chamber; aperture diameters of 1.0 mm or 1.5 mm are used. "B" marks a 4 mm slit connecting the lens and analyzer chamber.*

The reaction chamber of the system was equipped with two inlets, one for the plasma ion source and another for the sample line. Upon the introduction of reagent gas (also referred to as plasma gas) and sample into the reaction chamber, the internal pressure was maintained within the range of 1 to 15 mbar. The exit aperture of this chamber was 1.0 or 1.5 mm in diameter.

Following the reaction chamber, a system of lenses focuses the generated ions into the mass analyzer. The lens region was operated at an intermediate pressure range of 1 to 3 × $10^{-3}$ mbar. This lens chamber was connected to the analyzer chamber via a 4.0 mm exit slit, allowing a collimated ion beam to enter the high-vacuum region. The analyzer chamber itself was directly coupled to the turbomolecular pump to sustain high vacuum conditions (<$10^{-5}$ mbar), which are essential for mass analysis.

Both pressure gauges are from Pfeiffer Vacuum GmbH, Germany. The model TPR 270 and PKR 361 measure a range of $10^{-4}$ to 1000 mbar, and $10^{-9}$ to $10^{-2}$ mbar, respectively.[43] The model TPR 270 operates according to the Pirani principle and is integrated to monitor the pressure of the reaction chamber, including the HPCI source chamber and lens chamber.

On the other hand, the PKR 361 vacuum gauges, which operate with cold discharges, are called cold-cathode or Penning vacuum gauges to measure the analyzer chamber pressure. A common feature of all cold cathode ionization vacuum gauges is that they contain just two unheated electrodes, a cathode and an anode, between which a so-called cold discharge is initiated and maintained using a DC voltage (ignition voltage ≤ 4.5 kV, operating voltage ≤ 3.3 kV),[43] so the discharge continues at very low pressures.

## 3.3 Helical Resonator-driven HPCI Source

The HR plays a critical role in the plasma generation process by facilitating effective energy transfer to the plasma medium. This type of plasma is categorized as an inductively coupled plasma [44]. It offers a relatively high-density plasma ($10^{10}$ to $10^{12}$ $cm^{-3}$) at a comparatively low RF power of 10-40 W and a frequency range of 3-30 MHz, maintained at a pressure of $10^{-4}$ to 20 mbar [45–48].

In the present study, a C210 model OEM power supply from Heraeus Holding GmbH in Germany, was employed (cf. *Figure 3.3*). The resonator is made of a coil with a thin strand of copper, 5.3 meters in length, comprising 120 turns, surrounded by a 14 mm diameter support structure.

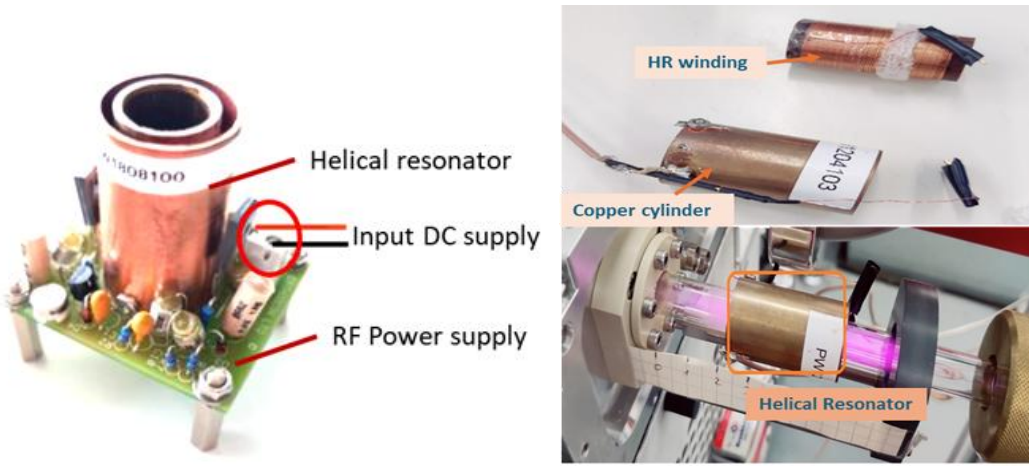


*Figure 3.3: Helical resonator and its driving power supply. A 15 V DC voltage is required to generate a 13.56 MHz [49] RF frequency. Integrated view of the HR with the plasma glass tube (lower right) of the HPCI source.*

One end of the coil is grounded, while the other end is left floating. For enhanced stability and efficiency during the plasma generation process, a copper cylinder surrounding the coil is an integral part of the entire circuit. This copper cylinder is connected to the same ground as the resonator coil. The HR acts as a slow-wave structure, enhancing the electric and magnetic fields necessary for plasma generation [48]. The resonator operates between 11 MHz and 16 MHz [8], with a power of less than 2 watts. The input direct current (DC) of 15 volts for the HR driving power is supplied by a DC power supply model E3611A from Agilent Technologies.

This advanced HR assembly is precisely integrated within a 12.7 mm outer diameter (OD) glass tube, which is then affixed to the reaction chamber of the MS. One end of the glass tube narrows down from 12.7 mm to 4.0 mm and slides into the reaction chamber. The HR position is adjustable along the glass tube. Plasma gas is supplied to the glass tube at the other end (12.7 mm OD) by copper tube fittings.

The HPCI source utilizes $H_2$ gas exposed to an HR driven 13.56 MHz RF electromagnetic field to generate a medium-pressure hydrogen plasma, resulting in a reactive plasma state consisting of protons, free electrons, neutral radicals, and electronically excited species.

## 3.4 Repeller

A repeller [50] plate is located in the reaction chamber (cf. in *Figure 3.1*). By properly tuning the DC supply, the ions are repelled towards the analyzer chamber through the lens chamber. This additional voltage may also influence the ionization processes and the resultant precision of ion detection.

This study focuses on the experimental setup involving an external voltage power supply (ORTEC model 456, USA) connected to the repeller plate. Operating a DC voltage < 80 volts, this power supply enables the controlled acceleration and deflection of ions, thereby enhancing their transmission into the mass analyzer.

## 3.5 UV-NIR Spectroscopy

### 3.5.1 UV-NIR Spectrometer with CCD

A spectroscopic device from Solar Laser Systems was used to measure the emission of the HPCI source in the UV to NIR regime. The model S100 operates within a wavelength (WL) range of 190–1100 nm, offering a spectral resolution of 1 nm, a minimal exposure time of 3 ms, and an average grating density of 300 lines/mm. A Toshiba CCD TCD1340AP linear image sensor is integrated to convert the optical emission into an electric signal. An optical fiber with a diameter of 0.6 mm was positioned to observe the signal on the glass tube of the plasma ion source, specifically between the ion source and the ionization source chamber.

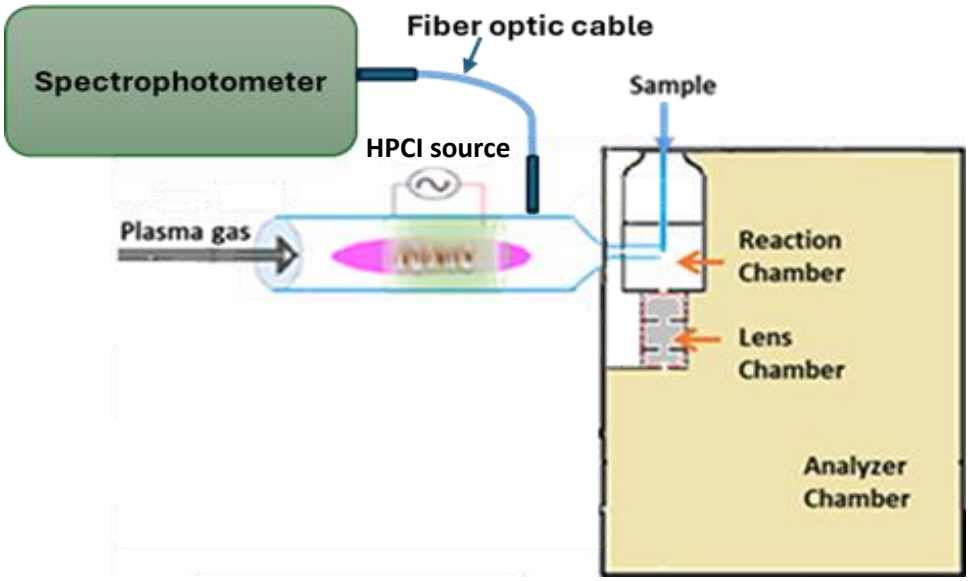


*Figure 3.4: Schematic diagram of the positioning of the optical fiber along the plasma glass tube of the HPCI source for emission measurement.*

The instrument interfaces via a USB cable and utilizes the Solar SL. Lab software (version 18.10.29.0) for data recording. This software adjusts exposure time and frame count to enhance data quality. The recorded data can be exported as a CSV file for further analysis.

### 3.5.2 UV-NIR Spectrometer with PMT

For more enhanced performance regarding resolution, signal to noise ratio and linear dynamic range, also a scanning iHR320 spectrometer (HORIBA Ltd., Kyoto, Japan) equipped with a 1800 grooves/mm grating and a photomultiplier tube (PMT) was used. A 220F optical fiber (HORIBA Ltd., Kyoto, Japan) was positioned radially on the plasma tube.

The photons were captured by a PMT (DPM-HV, HORIBA Ltd., Kyoto, Japan) and the signal was processed with a subsequent acquisition controller (SpectrAcq3, HORIBA Ltd., Kyoto, Japan). The spectrometer was set to scan from 300 to 900 nm with a step size of 0.05 nm and an integration time of 0.1 s. The entrance and exit slits were configured at 0.1 mm.

## 3.6 Flow Meter and Flow Controller

Plasma gas was introduced into the HPCI source using a 10 sccm mass flow controller (model F-200DV-ABD-11-V, Bronkhorst Deutschland Nord GmbH, Germany). The sample flow rate was regulated by a 10 sccm mass flow controller (model 1359CJ-00010SK, MKS Instruments Deutschland GmbH, Germany) and also monitored using a 10 sccm mass flow meter (model FM 360, Tylan Corp., USA). For further sample dilution, an additional 10 sccm mass flow controller (model 1179AX11CS1BK, MKS Instruments) was integrated into the system, and both flow rates were regulated using the Multi Gas Controller 647C, MKS Instruments. In addition, a 1 sccm mass flow controller (model F-200CV-002-ABD-88-K, Bronkhorst) was employed to introduce reagent gas (dopant). All mass flow meters and controllers were calibrated prior to use to ensure accurate flow measurements.

## 3.7 Reagent Gas Supply from Liquids (dopant)

With pure hydrogen the HPCI source primarily generates $H_3^+$ ions. To lower the risk of extensive fragmentation following the proton transfer reaction, the high gas-phase acidity of this species is reduced by adding reagent gases with higher proton affinities. Methanol has a proton affinity of PA 754.3 kJ·mol$^{-1}$, well above hydrogen and water (cf. *Table 1*). The primary species $H_3^+$ reacts with methanol ($CH_3OH$) and generates an abundant secondary reagent ion population of $CH_3OH_2^+$ and its cluster. These further react with the neutral analyte. In this work the saturated vapor phase of methanol is introduced to the reaction chamber to adjust the reactivity. As shown in *Figure 3.5*, synthetic air is bubbled through a temperature controlled liquid reservoir of methanol with approximately 0.5 sccm. The saturated vapor phase is merged via a T-connector with the sample flow and introduced to the reaction chamber.

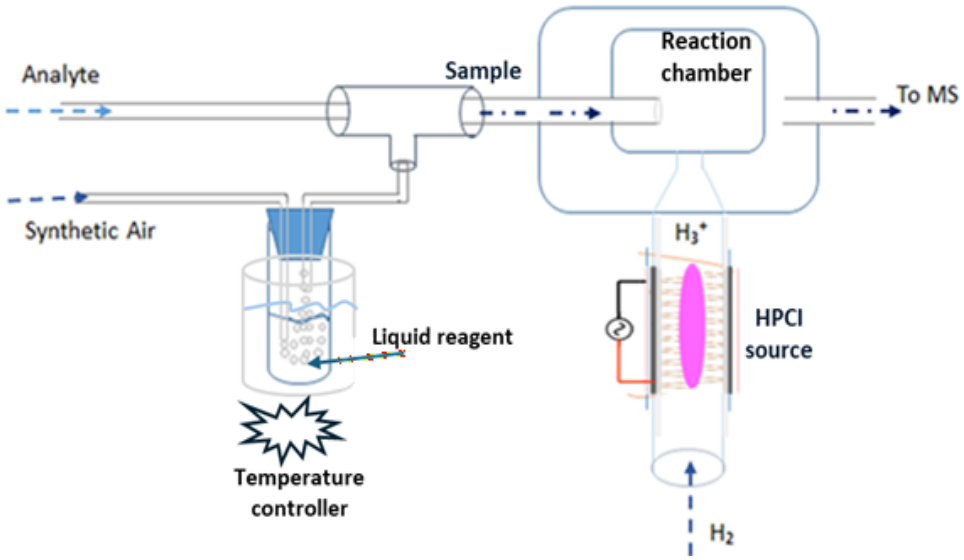


*Figure 3.5: Schematic diagram of the gas supply from liquid reagents.*

## 3.8 Chemicals

Messer Industriegase GmbH, Germany, supplied hydrogen and nitrogen with a stated purity of 99.999%. These gases were used either directly or after additional purification via a cold trap. In-house bottled benzene, toluene, and o-xylene (BTX) mixtures 10.6, 9.9 and 9.5 ppmV, respectively in synthetic air (5.0) were employed to calibrate the system. Additionally, toluene was mixed with synthetic air (5.0) to 12.6 ppmV. Moreover, o-xylene and toluene were mixed with nitrogen (5.0) to 4.1 ppmV and 12.6 ppmV, respectively.

Methanol (7.0 ppmV), ethanol (2.6 and 90.0 ppmV), propanol (1.6 and 45.0 ppmV), and n-butanol were premixed with synthetic air (5.0) and introduced into the system to evaluate sensitivity. The mixing ratios of the in-house bottled gases were evaluated using a GC- FID instrument. The vapor phase of Methanol with a purity ≥ 99.8 %, HPLC grade, Fisher Scientific, Loughborough UK, was used as a reagent gas.

## 3.9 Data Acquisition and Evaluation

The GC-FID MS data were recorded as raw data by the MSWS 8 system control version 8.2.1, Bruker Daltonics MS Workstation. A key advantage of this software is its seamless operation of both the GC and MS systems, whether used together or separately. It also facilitates the recording of profile and centroid data. The profile data provide the summed recorded intensity at each mass step, while the centroid data only display the maximum intensity of each unit mass. The raw data were exported in CSV format using Bruker's MS Data Review (including plotting chromatograms and spectra). Furthermore, Microsoft Excel [51] was used to process and evaluate the data, as well as to plot spectra and chromatograms.

# 4 Results and Discussion

## 4.1 Plasma Gas Studies

The helical resonator introduced to the MS system [8,36,38] can initiate plasmas from a broad variety of gas compositions at certain ranges of pressures. Changing these parameters will greatly affect the plasma conditions itself with respect to the electron energy distribution function and eventually the degree of ionization. Additionally, these parameters also control the plasma chemistry in terms of the kinetics and thermodynamics of ion-molecule reactions and thus the final distribution of charged species. This distribution in the plasma outflow is then characteristic of this source as the subsequent chemical ionization properties for analyte molecules.

These complex interdependencies will be investigated in this section. Plasma gases such as hydrogen with different degrees of purity and mixtures of $N_2$ in $H_2$ were introduced into the plasma source to investigate the formation of reagent ions such as $H_3^+$ and $N_2H^+$. Also the effects of variations in the gas pressures and flows will be discussed.

### 4.1.1 Plasma Gas

#### 4.1.1.1 Hydrogen as a Plasma Gas

Hydrogen has a very low proton affinity (cf. Table 1), therefore the $H_3^+$ ion is a very strong gas-phase acid. As mentioned in Section *3.3*, the HPCI source utilizes $H_2$ gas exposed to an HR driven 13.56 MHz RF electromagnetic field to generate a medium-pressure hydrogen plasma, resulting in a reactive plasma state consisting of protons, free electrons, neutral radicals, and electronically excited species. The relative population of $H_2^+$ to $H_3^+$ is pressure dependent in the low-pressure regime [52]. However, for the applied operating conditions – 1 - 20 mbar and pure hydrogen – it is reasonable to assume fast and quantitative conversion of initial $H_2^+$ to $H_3^+$ according to the reaction *Rn 7*.

Initially, in this PG study pure $H_2$ gas has been added to the PS. Since the PS is an open system to the reaction chamber, the width of the exit slit (aperture) of this chamber is crucial for maintaining the pressure of both the PS and the reaction chamber. Originally, an aperture size of 1.0 mm in diameter was installed on the system, which caused significant issues in generating reactant ions at relatively high pressure (cf. *section 4.1.2*). Therefore, the aperture size has been increased to 1.5 mm. With that, a PS pressure of 7 mbar is maintained by adding 5.5 sccm PG flow. In this condition, a mass spectrum of $H_2$ PG within a m/z range of 10 to 100 has been recorded and is shown in *Figure 4.1*. Abundant $H_3^+$ ions are expected, however, cannot be observed with this system due to the limitation of the low mass cutoff at m/z 10. Mainly ions at m/z 29, 32 and between m/z 14 and 19 are recorded, however, with rather low intensity, which demonstrates the purity of the gas. Compared to 12% $N_2/H_2$ PG, the abundances of the ion m/z 29 for $H_2$ gas were measured $10^5$ times lower. The signals at m/z 19 and m/z 29 result from proton transfer reactions according to *Rn 1* with $H_3^+$ and the $H_2O$ and $N_2$ molecules, respectively.

$$H_2O + H_3^+ \rightarrow H_3O^+ + H_2 \qquad (Rn\ 8)$$

$$N_2 + H_3^+ \rightarrow N_2H^+ + H \qquad (Rn\ 9)$$

The reaction rate coefficients of the reactions *Rn 8* and *Rn 9* are $5.9 \times 10^{-9}$ and $1.9 \times 10^{-9}\ \mathrm{cm^3 \cdot s^{-1}}$, respectively [53]. In addition to those signals, a group between m/z 12 and 18 is observed, which might at first be attributed to species such as $N^+$ at m/z 14 or $O^+$ at m/z 16. However, most likely those signals are due to hydrocarbons. From an energetic point of view $O^+$ and $N^+$ can be ruled out. Starting from $O_2$ and $N_2$, appearance energies of at least 17 eV and 24 eV are required, respectively [25]. Neither photoionization nor charge transfer reactions from plasma species can lead to their generation. Moreover, the direct interaction of fast plasma electrons with molecular oxygen and nitrogen cannot explain the abundant appearance of these two ionized fragments either. Compared to the reference EI mass spectra at the typical 70 eV electron kinetic energy [25], a population of merely roughly 20% of the atomic ion relative to the respective molecular ions are observed. However, the recorded spectrum from the hydrogen plasma in *Figure 4.1* shows a reversed population distribution with approximately an order of magnitude higher signal intensities at m/z 16 and 14 than at the expected molecular ions at masses m/z 32 and 28, respectively. Therefore, it is reasonable to assume that the pattern between m/z 12 and 16 is probably due to $CH_x^+$, with m/z 14 assigned

to $CH_2^+$ and m/z 16 assigned to $CH_4^+$. However, as mentioned earlier, the absolute abundances in this background spectrum of pure hydrogen are rather low ($\times 10^5$) as compared to hydrogen mixtures, since in fact the majority of ions from the plasma are $H_3^+$, which cannot be detected by this instrument due to the low mass cut off. This demonstrates the low impurity content of the main plasma gas obtained under this experimental condition.

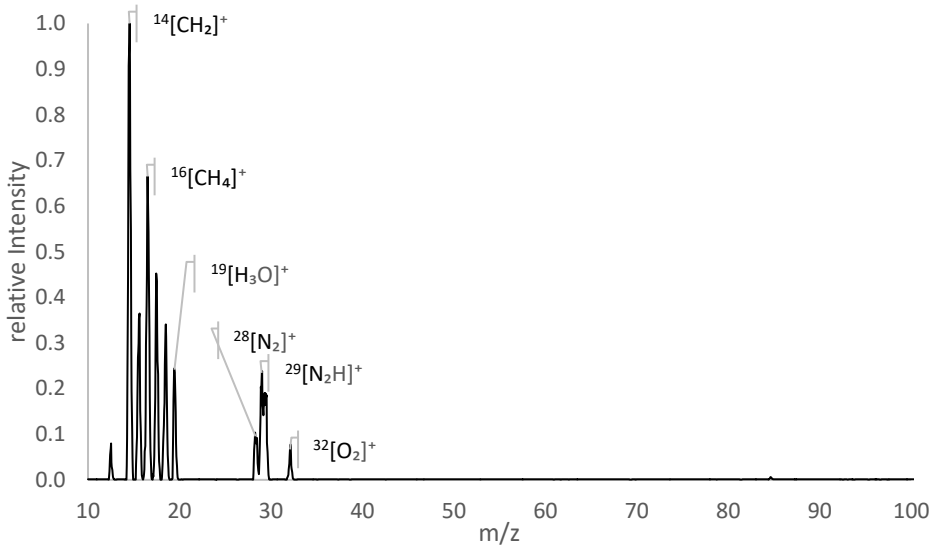


*Figure 4.1: Mass spectrum of the "pure" hydrogen plasma gas at a flow of 5.5 sccm. The y-axis shows relative intensity.*

A gradual increase in impurity signals has been observed as the PS pressure has been raised by adding more PG. As the system pressure increases, the reaction conditions change, presumably resulting in higher reactant $H_3^+$ density. Therefore, the impurities may collide more often with $H_3^+$ ions, as shown in reactions *Rn 8* and *Rn 9*, leading to increasing formation of $H_3O^+$, $N_2H^+$ ions, and others, as illustrated in *Figure 4.2*. An experiment of $H_2$ plasma conducted by Dr. Kroll also revealed that impurities such as $H_3O^+$, $N_2H^+$ ions increase with pressure [38].

To check the impurity-related signals at relatively high and low pressure conditions, pure hydrogen was introduced at flow rates of 5.5 sccm and 6.0 sccm, which resulted in plasma source pressure of 7 mbar and 8 mbar, respectively. The *Figure 4.2* (A) shows the recorded profile spectra for both conditions, and in (B) two chromatograms are plotted for the species $H_3O^+$ and $N_2H^+$, demonstrating the experimental reproducibility of these two conditions. The primary and secondary y-axes in (A) are the relative intensities of 8 mbar and 7 mbar pressure,

respectively. These intensities are related to the $N_2H^+$ intensity at 8 mbar. The x-axis of the spectrum shows the m/z range.

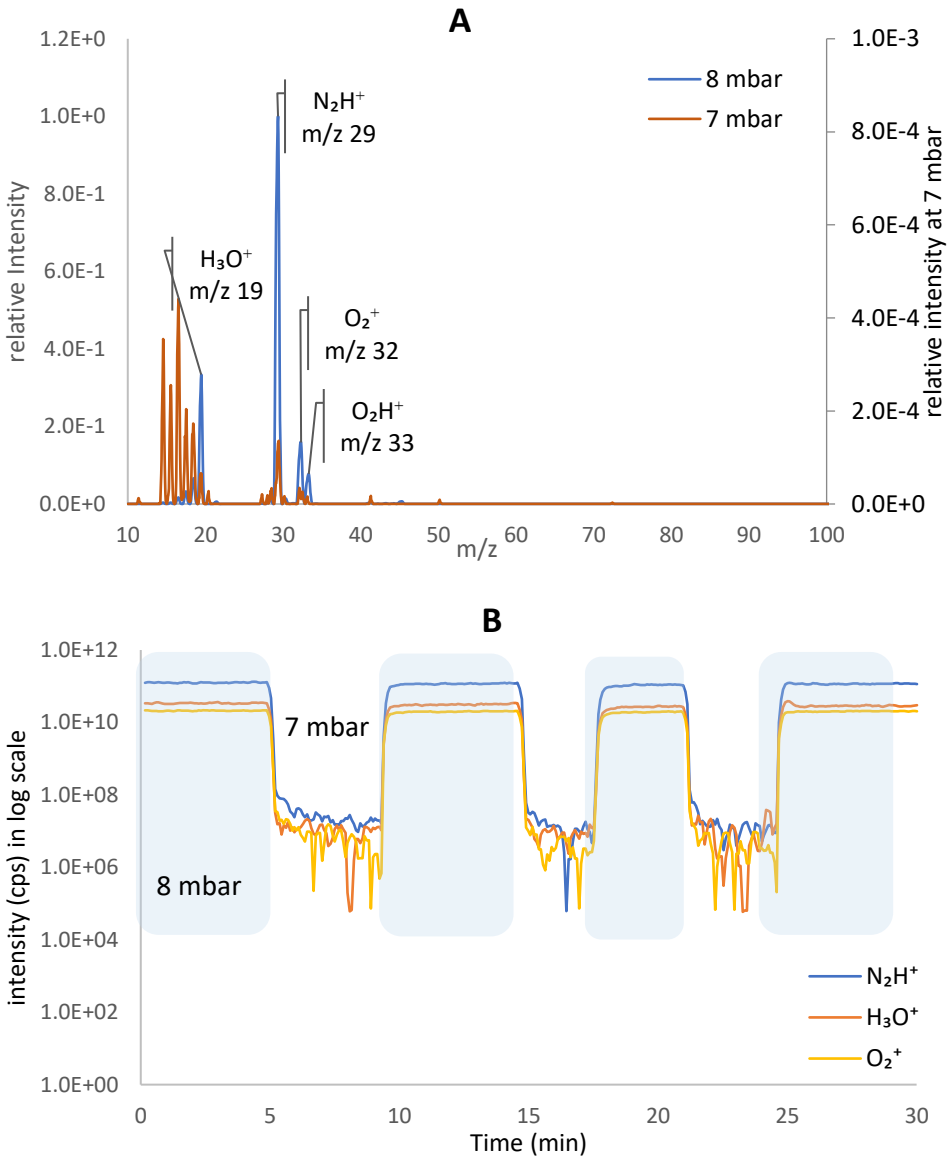


*Figure 4.2: The profile spectra of hydrogen plasma at 7 mbar and 8 mbar pressures are illustrated in graphs (A) and chromatograms of m/z 19, 29 and 32 in graph (B) at PG flow of 5.5 sccm and 6.0 sccm, corresponding to pressures of 7 and 8 mbar, respectively.*

The experimental data show an increase in impurity-related ion signals, especially $H_3O^+$, $N_2H^+$ and $O_2^+$, when the pressure is ≥ 7 mbar. A sharp, instantaneous jump in signal intensities is observed, when switching from 7 mbar to 8 mbar hydrogen condition and an equally strong

decrease when lowering the pressure back to 7 mbar. These jumps span three orders of magnitude and are clearly reproducible, as shown in *Figure 4.2* (B).

The pronounced non-linear behavior within a small range of merely 1 mbar required further investigation. Certainly, the pressure influences the plasma density and thus the $H_3^+$ ion formation rate. A higher density of primary ions as well as neutral impurities also changes the formation rate of species such as $O_2H^+$, $N_2H^+$ and $H_3O^+$, which should be observed as increasing signal intensities at the respective masses. Interestingly, none of the primary species ($H_2^+$ or $H_3^+$) can produce $O_2^+$ via charge transfer, they all protonate oxygen to $O_2H^+$. Thus the molecular ion of oxygen can either be generated via direct electron interaction or photoionization. The ionization energy of $O_2$ is 12.07 eV, which corresponds to a photon wavelength of 102.7 nm. This matches the transition from the second excited state to the ground state of the hydrogen atom with 12.1 eV or 102.5 nm, respectively. This could explain the rather strong presence of $O_2^+$ via photoionization. In addition, the molecular oxygen ion is rather inert within this matrix, since there is no reaction to hydrogen.

However, all these considerations cannot explain the observed pronounced non-linear increase in ion intensities. To correlate the mass spectral data to the impact of the pressure change between 7 mbar and 8 mbar on the plasma dynamics itself, also the optical plasma emission at these two conditions was investigated in the following.

#### 4.1.1.1.1 Plasma Emission Measurements I

A spectrometer, model S100 from the Solar Laser System (cf. *section 3.5.1*) was employed to analyze the variations in emission corresponding to changes in plasma parameters. This system measured spectral data from 300 nm to 800 nm under two different conditions. Initially, spectral data were collected with the plasma turned off to establish a baseline. Notably, this spectrum appeared baseline signals, providing a reference for further spectral analysis under different plasma conditions. Following this, the same source conditions as in the previous experiment with plasma gas flow rates of 5.5 (7 mbar) and 6.0 sccm (8 mbar) have been established to assess their impact on the emission characteristics. The two spectra in *Figure 4.3* have been recorded after introducing the above-mentioned PG flows. The optical fiber was positioned on the plasma glass tube between the PS and the reaction chamber (cf. schematic in *Figure 4.3*).

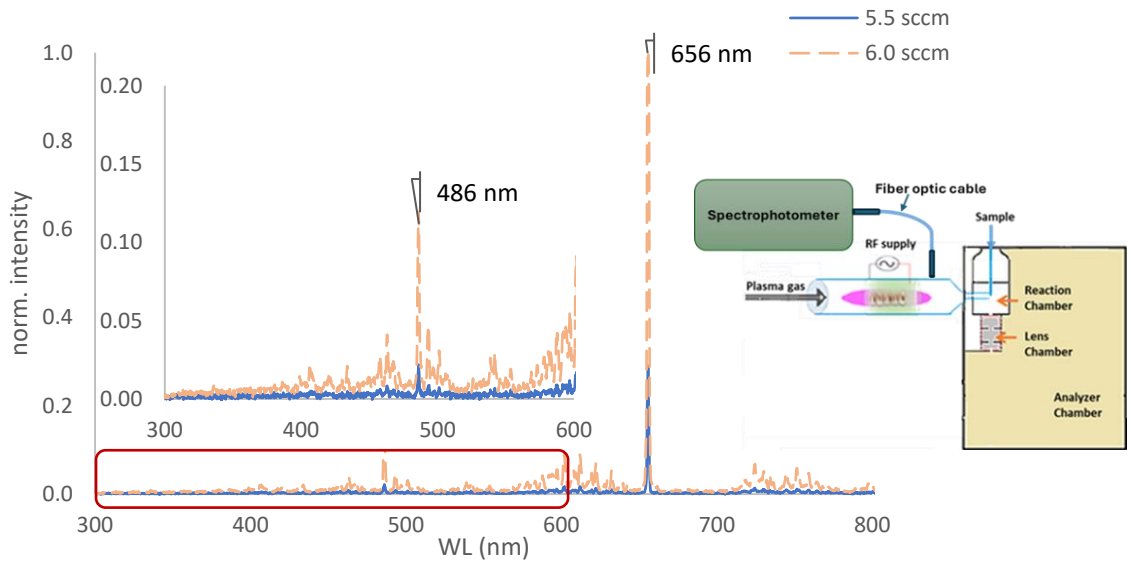


*Figure 4.3: Emission spectra of the plasma ion source at PG flow of 5.5 sccm and 6 sccm.*

At both flow rates, the strongest emission observed stems from the atomic hydrogen lines at 656 nm and 486 nm. According to the Balmer series [54,55], those are assigned to the H-α and H-β transitions, respectively, and are formed as the first and second emission lines in this plasma [56,57]. Between the two PS pressure conditions the spectral intensities vary significantly. At the H-α emission line, the intensity increased by approximately 75% when the gas flow was raised

from 5.5 sccm to 6.0 sccm. This rise in gas pressure promotes more substantial ionization, elevating the electron density and thereby enhancing the emission [58]. The initial hypothesis posits that modifying the PG flow alters the ion dynamics and, consequently, the ionization processes, which would significantly affect the ion intensity of impurities such as $N_2$ as well. The mass spectrum and chromatogram in *Figure 4.2* demonstrate that the increased gas flow markedly changes the ion intensities of impurities; however, emissions from impurities such as $N_2$ have not been identified by this spectrometer due to its limited sensitivity. To address this limitation, we employed a more sensitive spectrometer, the iHR 320 from Horiba Scientific, which offers a broader dynamic range, to replicate the same experiment.

#### 4.1.1.1.2 Plasma Emission Measurements II

The following measurement was conducted by the iHR 320 model spectrophotometer with PMT detector (cf. experiment *section 3.5.2*). The $H_2$ PG, flowing at 6.0 sccm, was introduced into the PS. Two spectra were recorded over the wavelength range 300–900 nm (*Figure 4.4)*: one with the PS off and one with the PS on. The spectrum obtained under PS-off conditions served as the baseline for comparison with the PS-on spectrum.

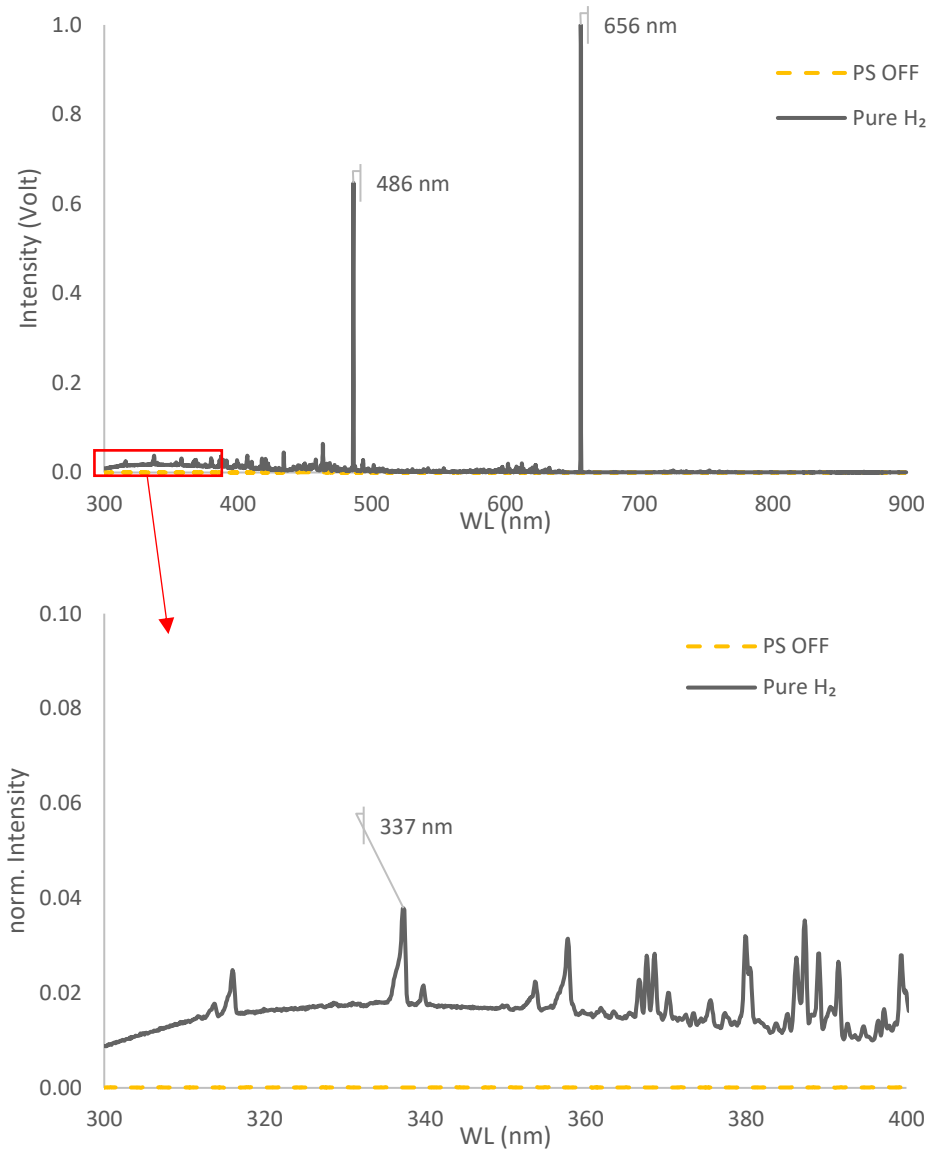


*Figure 4.4: Emission spectrum of a pure hydrogen plasma at 8 mbar, WL: 300-900 nm (upper) and 300-400 nm WL range (lower) for impurities check (especially $N_2$ emission).*

The black line in the upper *Figure 4.4* shows the hydrogen lines at 486 nm and 656 nm as the most abundant emission. Our primary focus, however, is on impurities, specifically $N_2$ molecules, since the MS system detects the $N_2H^+$ base peak upon adding 6.0 sccm of pure $H_2$. The lower panel, spanning 300–400 nm, marks the feature at 337 nm [59], corresponding to the 0-0 transition of the 2nd positive band of neutral nitrogen ($C\ ^3\Pi_u \rightarrow B\ ^3\Pi_g$). This emission is absent or weak when PG flows of pure hydrogen are ≤ 5.5 sccm, as shown in *Figure 4.2* (B). Collectively, these observations indicate that increasing the PG flow alters the plasma

conditions, primarily by increasing the pressure within the PS. Pressure variations influence the frequency and nature of ion–molecule collisions, thereby modifying the reaction kinetics. Note that minor leaks in the system may allow laboratory air—typically containing $N_2$, $O_2$, and $H_2O$ - to enter the plasma region.

#### 4.1.1.1.3 Impurities of $H_2$ Plasma

$H_2$ with a stated purity of 99.999 % has been used to generate a hydrogen plasma and form $H_3^+$ ions as primary reagents. However, at a certain PS pressure, $N_2H^+$ was observed as well. To estimate the emission of $N_2$ impurities within the hydrogen plasma, pure $H_2$ and a mixture of 12% $N_2$ in hydrogen were investigated with the iHR320 spectrometer. *Figure 4.5* displays the emission in the range of 300 to 900 nm of both measurements. With 12% $N_2$ strong emission of nitrogen was observed from the 2nd positive band of neutral nitrogen ($C\ ^3\Pi_u \rightarrow B\ ^3\Pi_g$) with the 0-0 transition at 337 nm as the most abundant. Further prominent emissions in this band are the 0-1 transition at 358 and the 0-2 transition at 380. The 337 nm emission increased by a factor of 53 as compared to the pure hydrogen plasma, whereas the atomic hydrogen lines at 486 nm and 656 nm decreased by a factor of 0.6 and 0.8, respectively.

From the relative intensity of the $N_2$ emission calculated from the intensity of 12% $N_2$, an impurity of 0.2 ± 0.02 % $N_2$ in the system, mainly due to leakage of the system when added hydrogen PG.

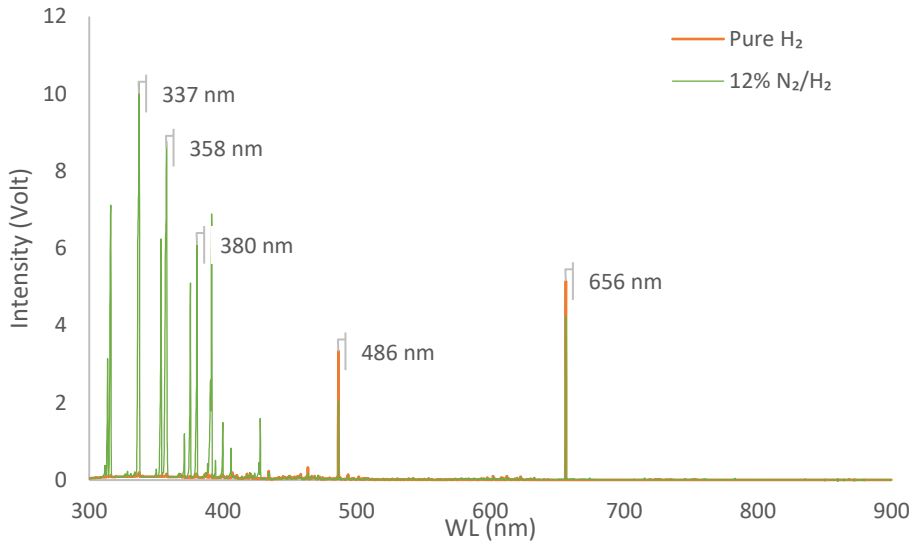


*Figure 4.5: Spectrum of 12% $N_2$ in $H_2$ PG (green line) and high-purity $H_2$ spectrum (orange line)*

In addition to the spectroscopic results, an MS spectrum has been recorded. A profile spectrum of 5.5 sccm with the 12% $N_2/H_2$ mixture is presented in *Figure 4.6*. The $N_2H^+$ ion at m/z 29 is observed as the base peak, with other prominent peaks at m/z 18, 19, 28, and 32 corresponding to $H_2O^+/NH_4^+$, $H_3O^+$, $N_2^+$, and $O_2^+$, respectively.

Under these conditions, $H_3^+$ and neutral $N_2$ are present and reaction *Rn 9* produces the $N_2H^+$ ion. In this step, $N_2$, which has a higher proton affinity (PA) than $H_2$, accepts a proton from the $H_3^+$ reactant ($\Delta PA = PA(N_2) - PA(H_2) = 71.3$ kJ mol$^{-1}$). The $N_2H^+$ formation proceeds very fast with a rate constant of $k = 1.9 \times 10^{-9}$ cm$^3 \cdot$s$^{-1}$ [53]. The $N_2H^+$ ion intensity in the mixed $N_2/H_2$ plasma is five orders of magnitude higher than in the pure $H_2$ plasma.

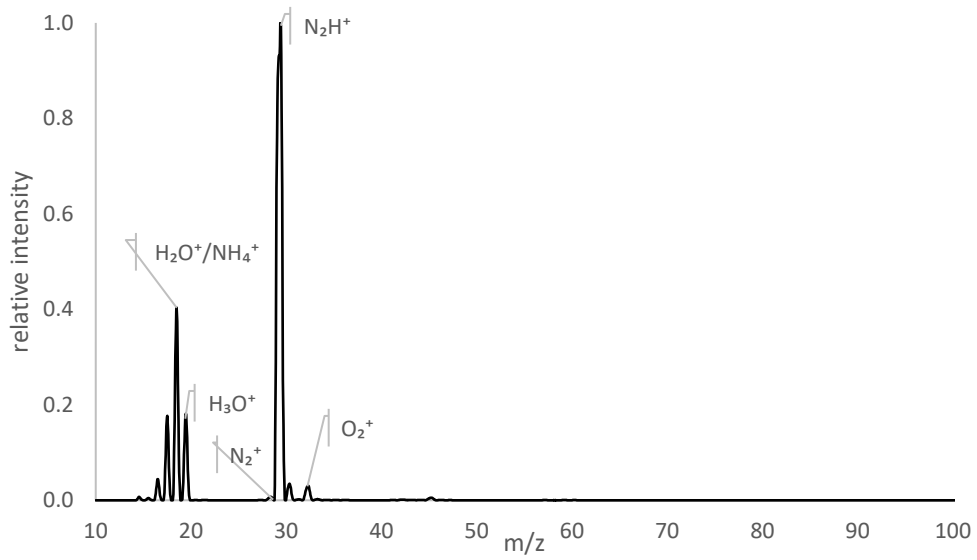


*Figure 4.6: Profile spectrum of 12% $N_2$ in $H_2$ plasma gas with a flow of 5.5 sccm corresponding to a PS pressure of 7 mbar.*

The second most abundant signal appears at m/z 18, which may correspond to either $H_2O^+$ or $NH_4^+$. Water has an ionization energy of 12.6 eV, so unlike the $O_2^+$ formation, photoionization is ruled out (cf. *page 24*); its formation must occur via direct interaction with plasma electrons. However, $H_2O^+$ further reacts with $H_2$ to form $H_3O^+$ [60]. The large absolute abundance at m/z 18, together with the substantial ratio to m/z 19, suggests that $H_2O^+$ is not the dominant contributor to the m/z 18 signal. Rather, ammonium formation $NH_4^+$ appears to be responsible

in this nitrogen–hydrogen plasma: abundant N and H radicals adsorb to the glass wall of the helical resonator and combine to form $NH_3$, which is subsequently protonated mainly by $H_3^+$ to yield $NH_4^+$ [61,62]. The exact masses are 18.02 Da for $H_2O^+$ and 18.04 Da for $NH_4^+$. Due to the limited mass resolving power of this TQ-MS with approximately $\Delta m/z \geq 0.7$, these ions cannot be distinguished and are observed as a single peak at m/z 18.

From the perspective of the pure $H_2$ plasma, ion intensities are comparatively lower than those observed in the 12% $N_2/H_2$ plasma at the same total flow rate (5.5 sccm). However, increasing the densities of neutral species and/or reactant ions in the plasma stage can alter the plasma reaction dynamics significantly. Consequently, it is important to assess the dependence on the $N_2/H_2$ mixing ratio in more detail, which is discussed below.

#### 4.1.1.1.4 Variation of the Plasma Gas Mixing Ratio

To understand the generation of ions depending on the mixing effect of the plasma gas, the $H_2$ gas and $N_2$ gas were introduced via two flow controller units with 10 sccm each, and mixed in-situ before entering the helical resonator. For each mixing ratio, the total flow was kept constant at a flow rate of 5.5 sccm to provide comparable conditions to the experiments in *section 4.1.1.1*. The mixing ratios investigated varied between 3% to 25% $N_2$ in $H_2$ by volume.

*Figure 4.7* exemplarily shows the mass spectra of plasma gas mixtures with 3% and 9% $N_2$ in $H_2$. The predominant ion observed in both spectra is again attributed to $N_2H^+$ at m/z 29. Additional ions identified include $N_2^+$, as well as $H_2O^+/NH_4^+$ (m/z 18) and $H_3O^+$ (m/z 19), which are likely due to trace impurities (water) and the in-situ formation within the plasma (ammonium) as previously discussed. Based on the profile spectra, it can already be seen that increasing the amount of nitrogen increases the total ion intensities, not only for $N_2H^+$.

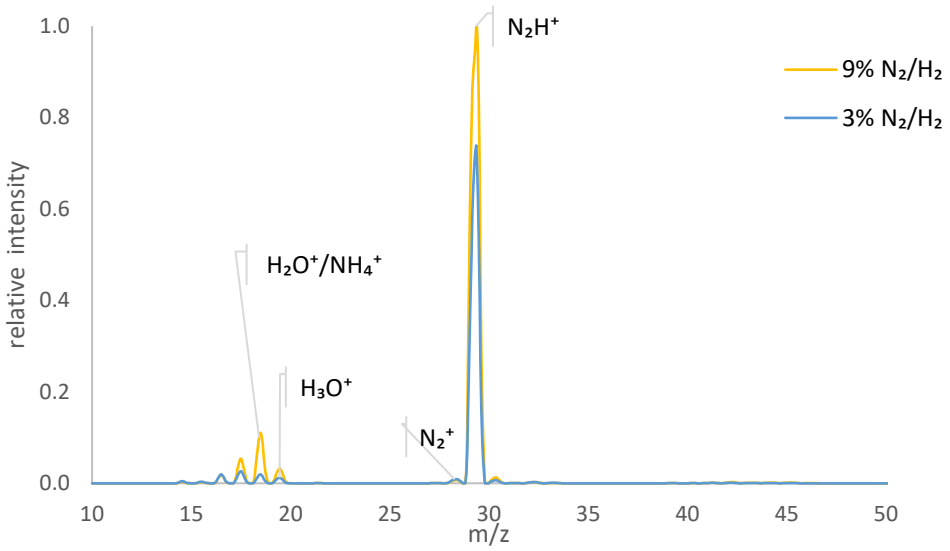


*Figure 4.7: Spectra of plasma gas mixture 3% and 9 % $N_2$ in $H_2$.*

The dependence of ion intensities on the nitrogen/hydrogen mixing ratio was systematically investigated, as illustrated in *Figure 4.8*. The primary y-axis shows the relative intensity of $N_2H^+$ at m/z 29 and the secondary y-axis shows the intensities of $N_2^+$, $H_3O^+$ and $H_2O^+/NH_4^+$ at m/z 28, 19 and 18, respectively. The highest total ion count was observed at 9% $N_2/H_2$ mixing gas. Thus, ion intensities are normalized using the ion counts at 9% $N_2/H_2$. Raising the $N_2$ fraction from 3% to 9% increased the $N_2H^+$ signal by 19% relative to the 3% baseline. Further increases to 12%, 15%, and 25% $N_2$ in $H_2$ produced a pronounced decrease in $N_2H^+$ intensity, falling to 75%, 26%, and 0.2% of the 9%-$N_2$ maximum, respectively. This non-monotonic dependence suggests competing processes influencing $N_2H^+$ formation as the $N_2/H_2$ mixing ratio is varied. With increasing $N_2$ fraction, nitrogen–electron collision cross sections begin to shape the electron energy distribution, the electron density, and the overall ionization rate—the fundamental plasma dynamics. More nitrogen molecules increase energy loss in inelastic collisions, which lowers the mean electron energy and, consequently, reduces the ionization rate. Thus, there is a trade-off: ion–molecule chemistry leading to $N_2H^+$ formation is enhanced with higher $N_2$ content, while the plasma dynamics are negatively affected by a reduced primary ionization rate. The net effect on observed ion signals depends on the balance between these competing processes and may favor higher $N_2H^+$ yields at certain mixing ratios, even as overall plasma density declines at higher $N_2$ fractions [63]. These results highlight the importance of maintaining an optimal $N_2/H_2$ mixing ratio to sustain adequate ion density and stable plasma conditions. Such optimization is essential for maximizing ion yields in plasma-based

applications, such as ionization in an MS system. The ionization efficiency directly influences the system's sensitivity [64].

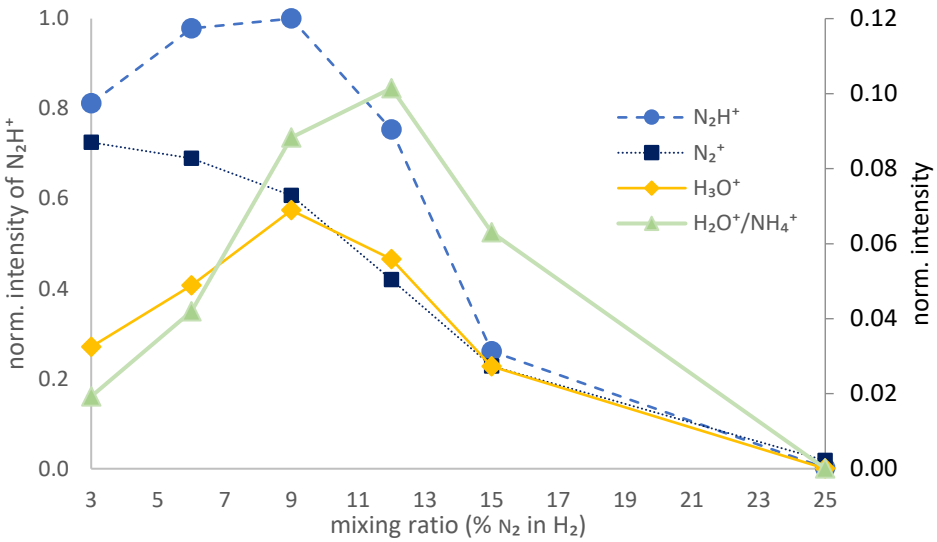


*Figure 4.8: $N_2H^+$ and other ions' dependency on plasma gas mixture. The primary vertical axis is $N_2H^+$ ion intensity, while others are in the secondary vertical axis.*

The optimal mixing ratio of 9% $N_2$ in $H_2$ appears to strike a favorable balance between plasma stability and energy transfer, thereby enhancing $N_2H^+$ (m/z 29) production. A similar trend is observed for $H_2O^+/NH_4^+$ (m/z 18) and $H_3O^+$ (m/z 19) signals: they increase with rising $N_2$ content and peak at the 9% $N_2/H_2$ ratio. Interestingly, the intensity of the $N_2^+$ (m/z 28) nearly decreases monotonically with increasing $N_2$ fraction between 3 and 25 %, as shown in *Figure 4.8*. It is speculated that the total ion formation rate already starts to decrease with 3% nitrogen addition.

On the primary y-axis of *Figure 4.9*, it is shown that the $N_2H^+/N_2^+$ ratio increases with added $N_2$ up to a 12% mixing ratio. A further increase to 25% $N_2$ results in a pronounced decline, yielding the lowest observed $N_2H^+/N_2^+$ value. This behavior suggests that excessive $N_2$ perturbs the PS ionization processes, reducing $N_2H^+$ formation. Similarly, the $N_2H^+/H_3O^+$ ratio, shown on the secondary y-axis, decreases with increasing $N_2$ content. This trend indicates a rise in water-related species (likely impurities in the $N_2$ feed) and a relative increase in $H_3O^+$ formation as $N_2$ content grows.

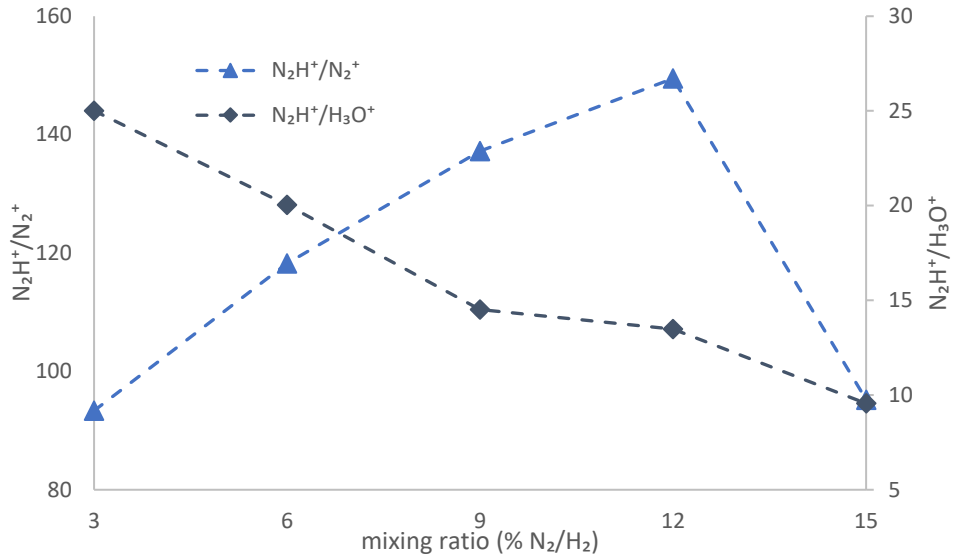


*Figure 4.9: Ratios of $N_2H^+$ to $N_2^+$ and $N_2H^+$ to $H_3O^+$ ions under different plasma gas mixing ratios.*

The $N_2/H_2$ mixing ratio was varied from 3% to 25%. In the lower $N_2$ range (3–9%), the $N_2H^+$ ion intensity changed by about 19%, suggesting that further reductions in $N_2$ could enhance total ion production by the HPCI source. However, the 10 sccm flow controller used in this setup imposes a practical lower limit, preventing achieving $N_2$ fractions below roughly 3%. To enable exploration at even lower mixing ratios, subsequent experiments were conducted with a 1 sccm flow controller to provide finer control over the $N_2/H_2$ composition.

Using a 1 sccm flow controller, the PG mixing ratio has been reduced to 0.2 % $N_2/H_2$. *Figure 4.10* depicts the variation of $N_2H^+$ relative intensity as a function of the PG mixing ratio, which ranged from 0.0 to 2.0% $N_2/H_2$. The x-axis represents the $N_2/H_2$ mixing ratio. The primary y-axis shows the relative signal intensity of $N_2H^+$, while the secondary y-axis represents the relative intensities of $N_2^+$, $H_2O^+/NH_4^+$, and $H_3O^+$.

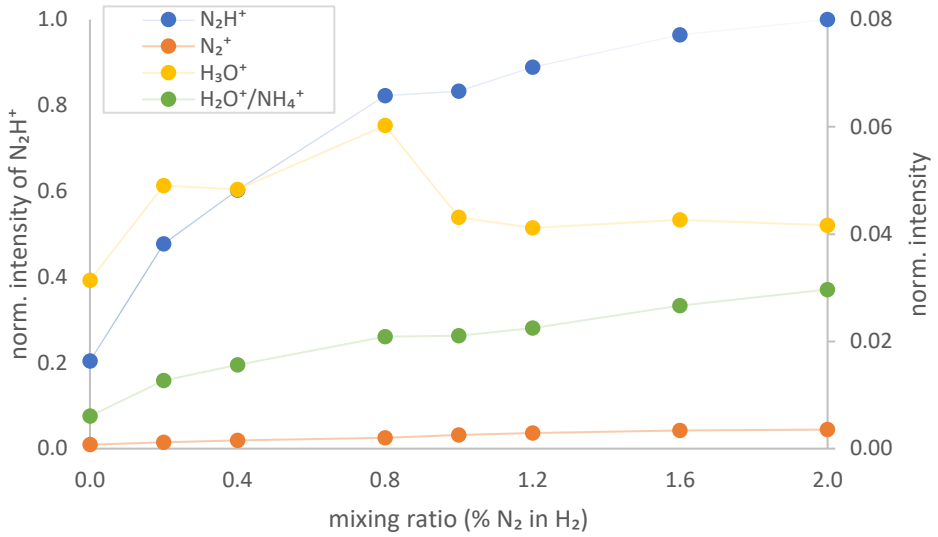


*Figure 4.10: Relative intensities of $N_2H^+$ (primary y-axis) and $N_2^+$, $H_2O^+/NH_4^+$, and $H_3O^+$ (secondary y-axis with varying PG mixing $N_2$ in $H_2$.*

The $N_2/H_2$ mixing ratio was gradually increased up to 2.0%. Within this range, the ion intensity of the $N_2H^+$ signal linearly increased by approximately 36% at first from 0.2% mixing ratio and then started levelling off at around 1.0 % $N_2$ addition. At a 2.0% PG mixing, the relative intensities of $N_2^+$ (m/z 28) and $H_2O^+/NH_4^+$ (m/z 18) were approximately 0.2% and 2%, respectively, representing roughly threefold and twofold increases, respectively, relative to the 0.2% mixing level. By contrast, the $H_3O^+$ ion intensity remained essentially unchanged.

Additionally, the plasma emission of the 2nd positive band of neutral nitrogen ($C\ ^3\Pi_u \rightarrow B\ ^3\Pi_g$) at the 0-0 transition at 337 was monitored in parallel using the iHR 320 spectrometer. As depicted in *Figure 4.11*, this emission shows a perfect linear correlation with increasing nitrogen addition between 0.2% and 2.0%.

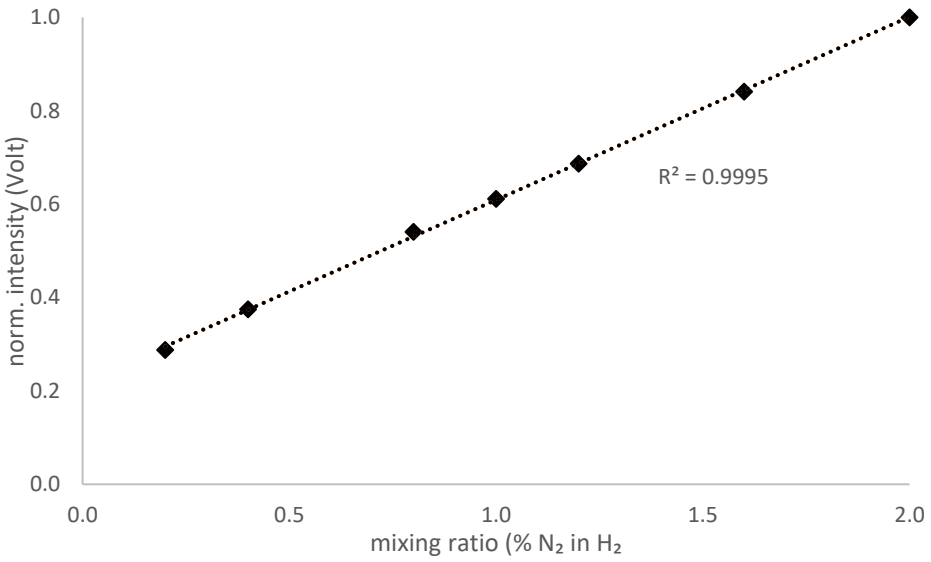


*Figure 4.11: Plasma gas mixing ratio (%$N_2$ in $H_2$) vs Volt intensity of spectrophotometer at nitrogen emission line WL 337 nm*

Overall, increasing the $N_2$ fraction in the $H_2$ plasma gas enhances $N_2H^+$ formation up to a 9% $N_2/H_2$ ratio; beyond this value, the $N_2H^+$ concentration decreases, likely due to a reduction in the primary ion $H_3^+$. The maximum production of $N_2H^+$ occurs at 9% $N_2/H_2$. Nevertheless, subsequent experiments were conducted with 10% and 12% $N_2/H_2$ mixtures due to gas availability in the laboratory.

### 4.1.2 Modification of the Reaction Chamber on Plasma Gas Flow

To observe the $N_2H^+$ ion in the HPCI-MS, 10% $N_2/H_2$ mixing gas and $N_2$ gas have been used as the PG and the sample gas, respectively. The plasma gas is supplied to the plasma glass tube. This tube and sample line are connected to the reaction chamber (cf. *Figure 3.2*). The reaction chamber consists of an aperture disk with a small hole (cf. *Figure 4.17*), which is also crucial for maintaining the chamber pressure. In this section, the $N_2H^+$ ion has been observed along with other related ions depending on aperture size and the corresponding pressure variation.

Initially, PG flow ranged from 1.0 to 3.0 sccm, while the sample gas flow was maintained at 4.0 sccm. The pressure of the PS was less than 1.0 mbar when only the PG was added using the original 1.0 mm aperture disk. Although these two gases (PG and sample gas) kept the ion source pressure between about 1.0 mbar and 1.7 mbar. In this condition, measurements have been performed and ions such as $N_2H^+$ and $N_2^+$ were observed. These measurement results are plotted in *Figure 4.12*, where the x-axis and y-axis show the PG flow and relative intensity with respect to the $N_2H^+$ intensity of 2.0 sccm PG flow, respectively.

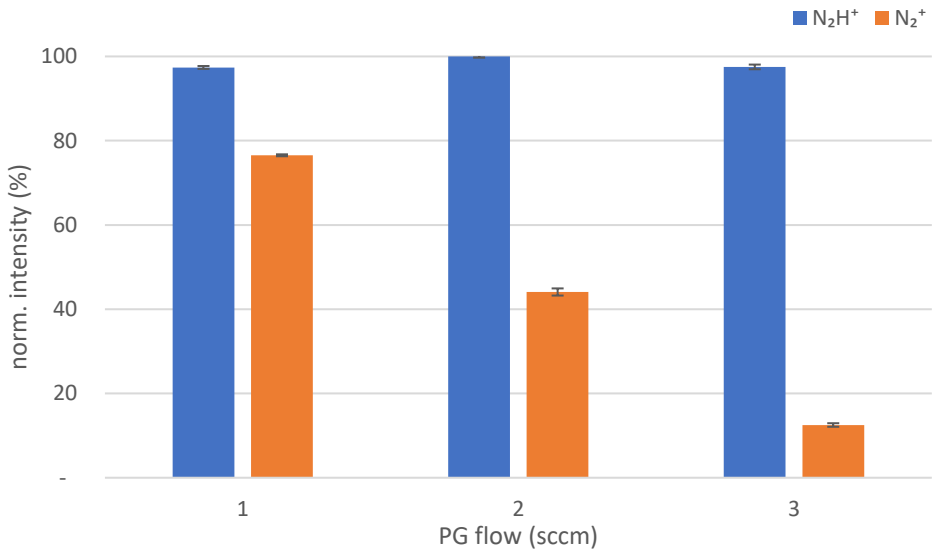


*Figure 4.12: $N_2H^+$ and $N_2^+$ ion dependency on PG. A 10% $N_2/H_2$ mixture as the plasma gas and $N_2$ as the sample, was employed.*

It was observed that the generated $N_2H^+$ population remained essentially unchanged with variations in pressure. In contrast, the $N_2^+$ signal decreased markedly as the PG flow increased: the relative intensity of $N_2^+$ decreased by approximately 66% and 87% of the 1 sccm baseline

when PG flow was increased to 2.0 sccm and 3.0 sccm, respectively. Experimentally, the PG flow was varied while the sample flow remained constant. As discussed above, the source pressure should scale with the PG flow. However, the pressure remained effectively constant throughout the measurements. This constancy could account for the unchanging $N_2H^+$ population originating from the active plasma zone and entering the reaction chamber. Conversely, the decrease in the $N_2^+$ signal with increasing PG flow is likely due to a reduced flux of pure nitrogen from the sample flow reaching the edge of the active plasma zone at the junction of the two perpendicular flow streams.

Based on these observations, we inferred that the plasma glass tube might not be adequately sealed in the reaction chamber. Furthermore, as shown in (cf. *Figure 4.13* left), the glass tube with an outer diameter (OD) of 4.0 mm is coupled to the reaction chamber, whose glass inlet has a diameter of 4.7 mm. Therefore, the reaction chamber resides in the open space of the lens chamber (cf. in *Figure 3.2*), and its surroundings are influenced by the vacuum in the lens chamber, which operates at a pressure three orders of magnitude lower than the reaction chamber. To mitigate this, PTFE tape was used to increase the effective OD of the glass tube (cf. *Figure 4.13* right) and the assembly was reinstalled to the reaction chamber.

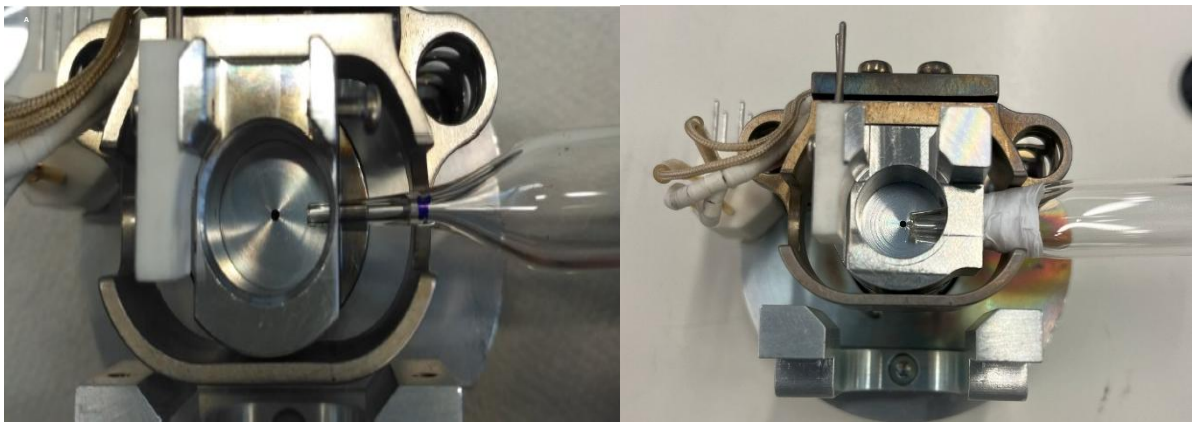

*Figure 4.13: The plasma glass tube is coupled to the reaction chamber. The left figure shows the state before sealing, and the right figure shows the state after sealing.*

With the improved sealed configuration, a PG $N_2/H_2$ mixture ($N_2$ fraction of 10 %) at a flow rate of 2.5 sccm and a pure $N_2$ sample at a flow rate of 4.0 sccm were introduced into the reaction chamber. Under these conditions, the plasma source, including the reaction chamber, reached a pressure of 10.0 mbar at both inlets, nearly an order of magnitude higher than observed with the unsealed configuration.

Under these conditions, the mass spectrum (*Figure 4.14)* is dominated by a single peak at m/z 18, while the previously dominant $N_2H^+$ signal at m/z 29 is markedly diminished. The peak at m/z 18 is most plausibly assigned to $NH_4^+$ rather than to $H_2O^+$. As discussed in *Section 4.1.1.1*, neither photoionization, charge transfer, nor conventional chemical ionization processes can account for an increase in $H_2O^+$ with rising pressure alongside the depletion of $N_2H^+$. By contrast, a rise in ammonium ion formation with pressure provides a coherent explanation: (i) higher pressure promotes heterogeneous formation of $NH_3$ on the glass surface of the plasma tube and on the metallic surfaces of the reaction chamber; (ii) the increased $NH_3$ availability and the higher collision frequency facilitate protonation by $N_2H^+$, effectively titrating the $N_2H^+$ population in favor of $NH_4^+$ [53,65]. This proton-transfer step can be represented as

$$NH_3 + N_2H^+ \rightarrow NH_4^+ + N_2 \qquad (Rn\ 10)$$

Thus, the observed progression toward $NH_4^+$ and the suppression of $N_2^+$ with increasing pressure are consistent with this mechanism.

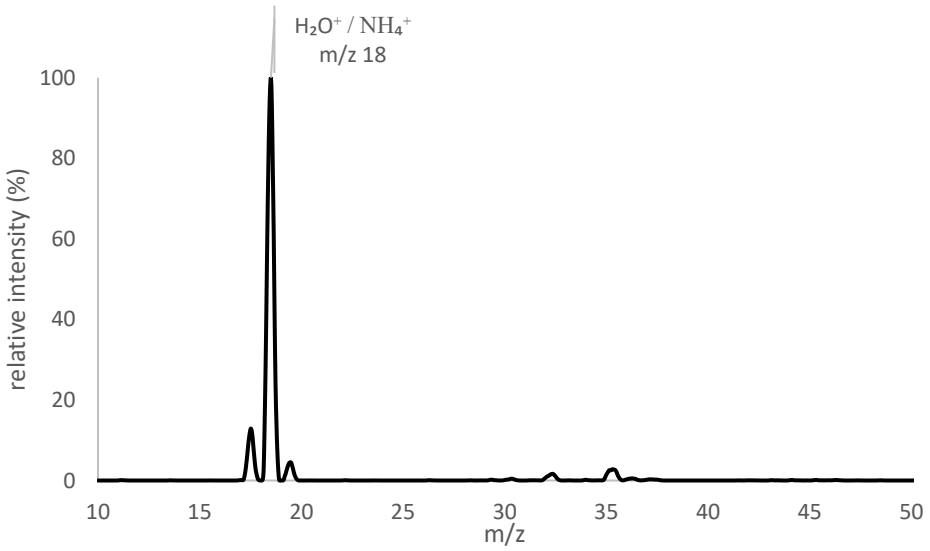


*Figure 4.14: Profile spectra of 2.5 sccm 12%$N_2$ in $H_2$ PG, an $N_2$ sample flow rate of 4.0 sccm at 10.0 mbar pressure with a 1.0 mm aperture*

Interestingly, Bräkling *et al* [8] reported the formation of $N_2H^+$ as the predominant species within a pressure regime of 2.0–13.0 mbar. Their experimental setup utilized a serial multistage inlet system, which spatially isolated discrete chemical transformation steps. Crucially, this

configuration suppresses the heterogeneous formation of neutral $NH_3$. In contrast, the present study employs a "one-pot" ion-molecule reaction system to generate $N_2H^+$ in situ from a nitrogen/hydrogen plasma discharge. While the complex network of ion-molecule reactions theoretically converges on the production of $N_2H^+$ (see *Section 4.1.1.1*), this "one-pot" approach does not preclude the heterogeneous synthesis of neutral $NH_3$. It is postulated that the presence of $NH_3$ subsequently interferes with the primary ion population by effectively quenching the $N_2H^+$ signal. Although $NH_4^+$ could be utilized as an alternative reagent ion, its lower gas-phase acidity relative to $N_2H^+$ would significantly increase the selectivity of the system, potentially limiting the range of detectable analytes. Driven by these considerations, the chamber pressure was reduced from 10.0 mbar to approximately 6.0 mbar by decreasing the plasma gas flow while maintaining a constant $N_2$ sample flow of 4.0 sccm. This adjustment yielded a subdued but distinct signal at m/z 29 (data not shown). To characterize this behavior more rigorously, the pressure in the plasma source and reaction chamber was systematically varied from 0.2 to 7.5 mbar by modulating the plasma gas flow ($N_2/H_2$ 12% mixture) in the absence of sample flow. As illustrated in *Figure 4.15* (upper panel), the mass spectrum at 7.5 mbar is still dominated by $NH_4^+$, however, with $N_2H^+$ already accounting for approximately 10% relative to the base peak. Notably, the intensity of $N_2H^+$ exhibits an inverse correlation with pressure; this trend is quantitatively summarized in the lower panel of *Figure 4.15* lower, where the x-axis and y-axis show the PS pressure and intensity (cps) in log scale, respectively.

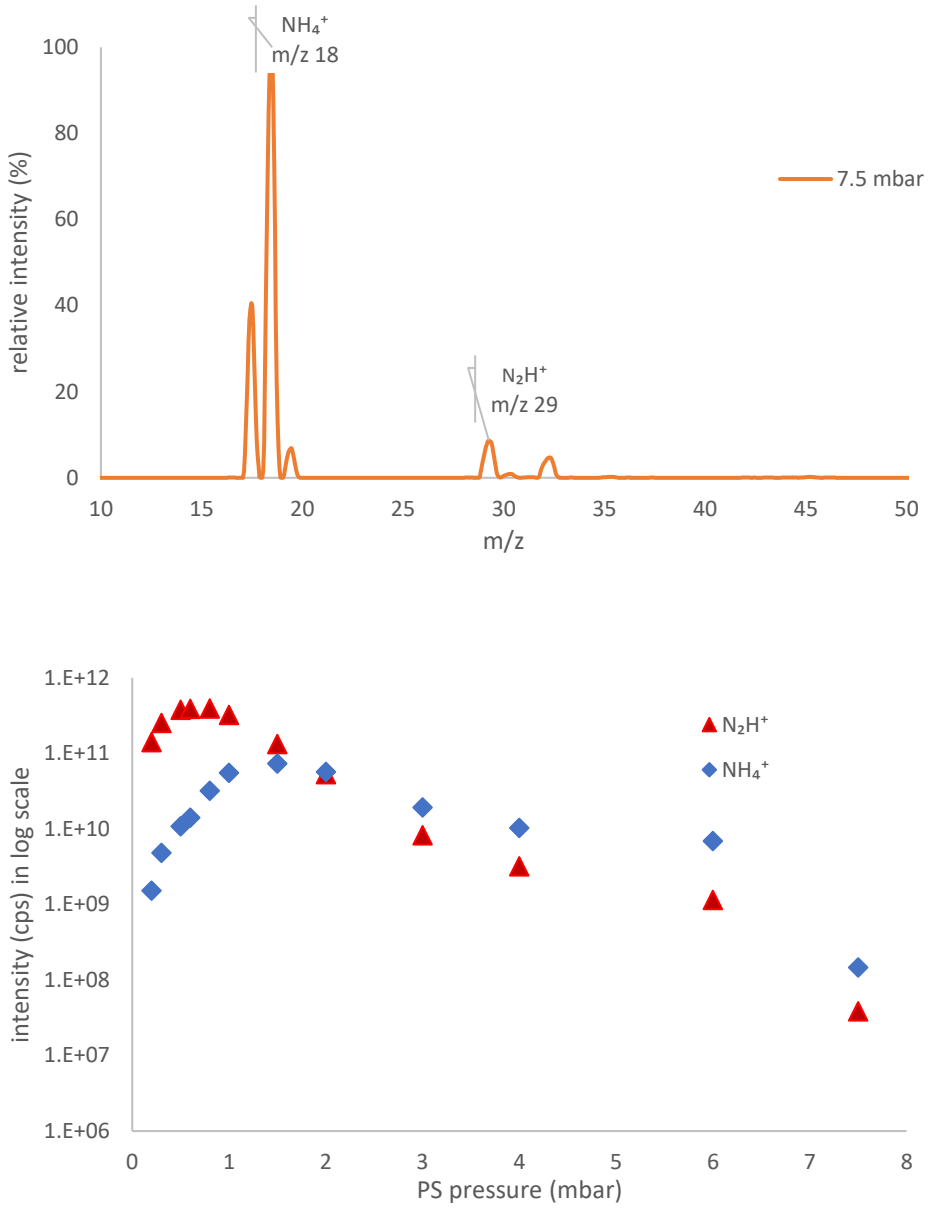


*Figure 4.15: Profile spectra of 5.3 sccm 12% $N_2/H_2$ PG at 7.5 mbar using 1.0 mm aperture (upper); $N_2H^+$ and $NH_4^+$ dependency of plasma gas on reaction chamber pressure.*

According to these experimental data, the ion $N_2H^+$ intensity slightly increases from 0.2 up to 0.8 mbar into a maximum and then dramatically decreases by nearly four orders of magnitude with increasing pressure from 0.8 up to 7.5 mbar. On the other hand, the $NH_4^+$ ion signal increases to a maximum from 0.2 to 1.5 mbar and the ion intensity decreases as the pressure increases. At 7.5 mbar, its intensity decreases by about three orders of magnitude from the ion intensity at 1.5 mbar. Below 0.2 mbar the plasma extinguishes.

Additionally, a spectrum at 1.5 mbar plasma gas is presented in *Figure 4.16.* In this figure, the $N_2H^+$ signal appears as the base peak alongside with $NH_4^+$ and $H_3O^+$ ions.

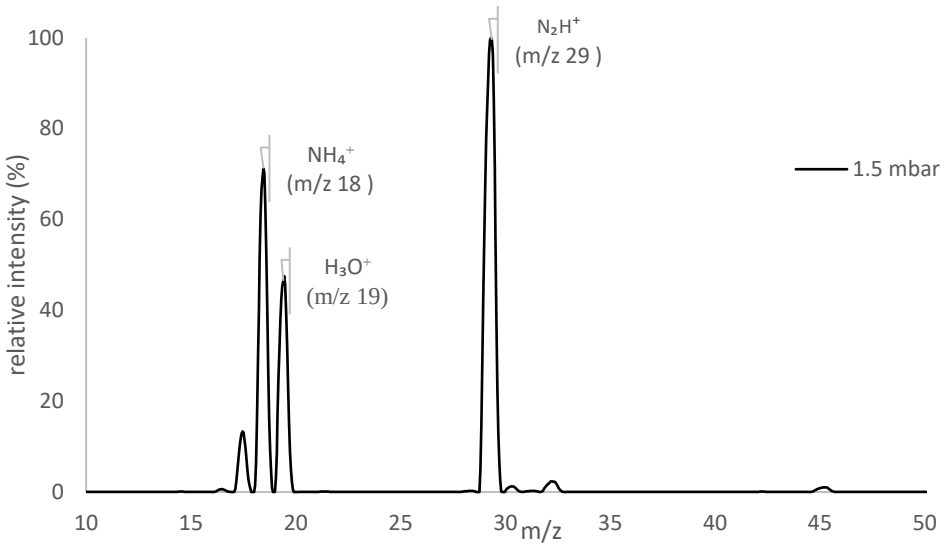


*Figure 4.16: Profile spectra of 2.2 sccm PG (12% $N_2$ in $H_2$) at 1.5 mbar pressure with 1.0 mm aperture ID.*

However, when the sample flow is turned on as well, the $N_2H^+$ ion completely vanishes again, which is readily explained by the increased chamber pressure. To address this limitation in flow conductance of the reaction chamber, the original aperture disk with 1.0 mm orifice was replaced by an aluminum disk of 19.0 ± 0.1 mm diameter, a thickness of 0.5 mm and an orifice diameter of 1.5 mm. Subsequent measurements were performed with this modified configuration.

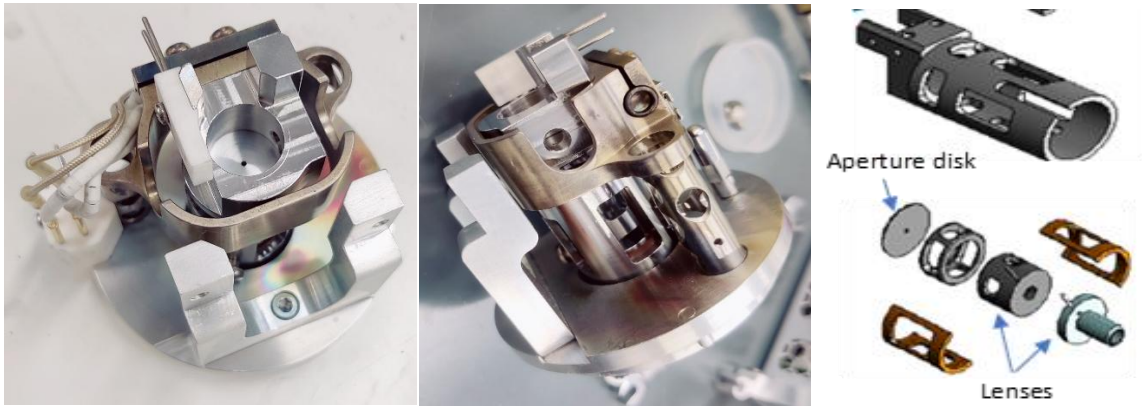


*Figure 4.17: Reaction chamber with aperture (left side), side view of this chamber (middle), and aperture disk & lenses (right side).*

As anticipated, the enlargement of the orifice to 1.5 mm in diameter yielded consistently lower pressures in the ionization chamber than in the preceding configuration. The initial experiment employed a plasma-gas flow of 4.8 sccm, corresponding to a chamber pressure of 4.0 mbar. The profile spectrum for this condition is shown in the upper panel of *Figure 4.18*, with the base peak observed at m/z 29.

Following the replacement of the aperture disk with one featuring a diameter of 1.5 mm, the pressure within the reaction chamber is lower compared to the previous configuration. The initial measurement has been conducted using only PG at 4.8 sccm into the system, resulting in a chamber pressure increase to 4.0 mbar. A profile spectrum of the mixing gas at a pressure of 4.0 mbar is depicted in *Figure 4.18*.

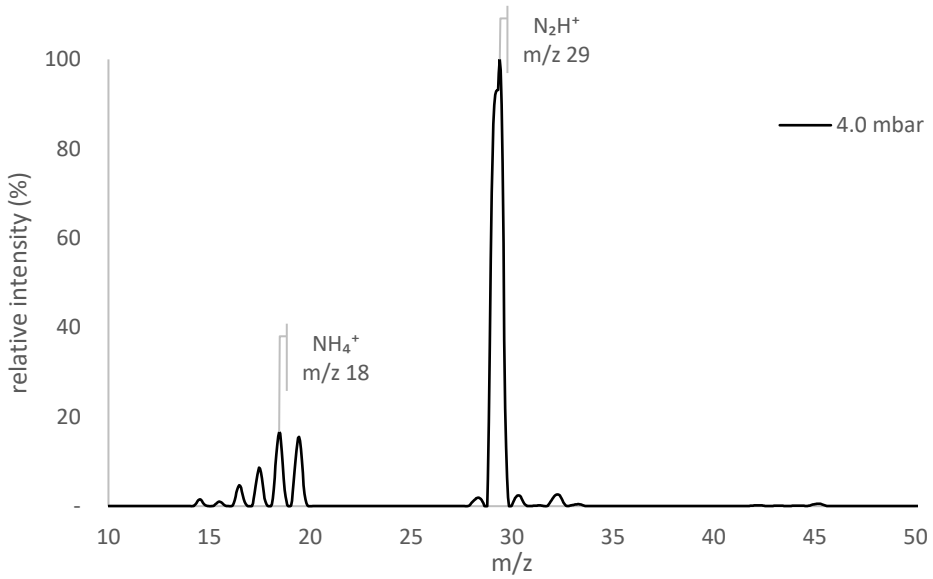


*Figure 4.18 : Profile spectrum of 12% $N_2$ in $H_2$ at 4.0 mbar pressure using a 1.5 mm aperture in the reaction chamber.*

Because ion abundances are pressure dependent, optimal ion production was achieved using a 1.5 mm aperture in the reaction chamber, which provided a favorable balance between pressure and ionization efficiency. Following this optimization, two sets of experiments are conducted: one in which only the PG flow rate is varied (cf. *section 4.1.3*), and another in which the PG flow rate is varied while maintaining a constant flow of sample (cf. *section 4.1.4*). These experiments are designed to systematically evaluate the dependence of ion abundances on gas flow conditions.

### 4.1.3 Plasma Gas Flow without Analyte Flow

This section discusses the dependence of reactant ions on the gas flow of the HPCI source. Reactant ions are crucial for the overall analytical performance and also for understanding the mechanisms of chemical reactions in the HPCI-MS system. Varying the PG flow within a plasma environment may influence the formation of reactant ions. The following measurements were conducted for a fixed distance of the helical resonator. The HR distance was defined as the length measured from the end of the PS glass tube, extending toward the reaction chamber, to the center of the HR. Since variations in the HR position can influence ion–molecule interactions (discussed in *section 4.2)*, the HR distance was maintained at 100 mm throughout these experiments. A 12% $N_2/H_2$ plasma gas mixture was used to generate $N_2H^+$ reactant ions, while the sample line was sealed with an end cap to eliminate any influence from analyte molecules.

Initially, the PG flow rate was set to 2.5 sccm and was gradually increased to a maximum of 7.5 sccm. As the gas flow increased, the overall system pressure rose correspondingly, ranging from approximately 1.6 mbar to 15.6 mbar. The resulting variation in $H_3O^+$ (m/z 19), $N_2^+$ (m/z 28) and $N_2H^+$ (m/z 29) ion intensities as a function of PG flow rate is shown in *Figure 4.19*. The maximum $N_2H^+$ abundance was observed at a gas-flow rate of 5.5 sccm; consequently, all ion intensities were normalized to the $N_2H^+$ abundance measured at that flow rate. The x-axis and y-axis show different PG flows in sccm and norm. intensity in cps, respectively. The primary y-axis shows the intensity for $N_2H^+$, and the secondary y-axis shows the intensity for $H_3O^+$ and $N_2^+$. In addition, the PS pressure (in mbar) corresponding to the plasma gas flow is shown on the secondary x-axis.

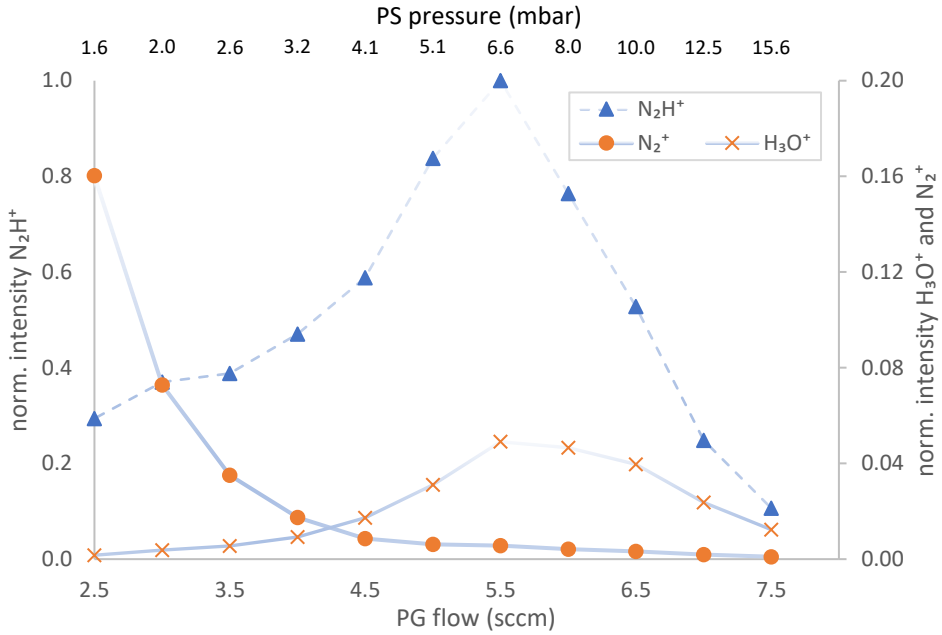


*Figure 4.19: The dependence of ions on plasma gas flow is observed. $N_2H^+$, $N_2^+$ and $H_3O^+$ are represented by blue, orange, and yellow marks, respectively. The secondary x-axis shows the corresponding PS pressure on the introduced PG flow.*

At a flow rate of 2.5 sccm, the PS pressure is approximately 1.6 mbar, and the ion yield is relatively low. Beyond this flow, the abundance of $N_2H^+$ ions begins to increase. This positive trend has been observed up to the flow of 5.5 sccm (cf. *Figure 4.19*). However, further increases in the plasma gas flow beyond this point—to 6.5 sccm and 7.5 sccm—led to a pronounced decline.

The ion abundances are normalized with the measured ion abundances at 5.5 sccm flow (6.6 mbar). The relative ion abundance at 2.5 sccm flow is calculated to be 30% for the $N_2H^+$ ion. When the flow is increased to 3.0 sccm, this ion abundance rose significantly to approximately 40%. Upon the introduction of a flow of 4.0 sccm and 5.0 sccm, the relative abundance of $N_2H^+$ ions increased markedly from 47% to 83%. However, further increases in the plasma gas flow result in ion abundances dropping to 52% and 10% at 6.5 sccm (10.0 mbar) and 7.5 sccm (15.6 mbar), respectively. This decline is linked to the rising neutral density, which alters the plasma conditions and the overall production of ions.

Additionally, the $N_2^+$ ion abundance is measured in this experiment. It is observed that starting from 2.5 sccm, this intensity exponentially drops with increasing flow rate and source pressure,

respectively. This might be attributed to enhanced subsequent ion molecule reactions of initial $N_2^+$ with $H_2$ to form the thermodynamically more stable $N_2H^+$.

As discussed in *Section 4.1.1.1*, with increasing plasma gas flow rates rising impurity levels within the system were observed. The main impurity is water, which is a thermodynamically favored end product ($H_3O^+$) within the $N_2/H_2$ matrix due to the high proton affinity (cf. *Table 1*). Experimental data strongly support this correlation, indicating that as the plasma gas flow increases, there is a significant rise in the abundance of $H_3O^+$ ions. This trend highlights the growing prevalence of water-related impurities at higher pressure, which may have substantial implications for plasma chemistry and system performance. The intensity of $H_3O^+$ is about 4% relative to $N_2H^+$. Both species ($H_3O^+$ and $N_2H^+$) are formed with $H_3^+$ faster with rate coefficients of $5.9 \times 10^{-9}$ and $1.9 \times 10^{-9}\ cm^3 \cdot s^{-1}$, respectively [53,66]. In addition, $N_2H^+$ can further react with $H_2O$ as mentioned earlier. It is essential to emphasize that this trend of increasing $H_3O^+$ ion intensity was consistently observed also up to the 5.5 sccm flow; after this point, further increases in plasma gas flow resulted in a decrease in the intensity of all ions.

*Table 2* below shows that at 2.5 sccm, the $N_2H^+$ and $N_2^+$ ratio is 2, which increases with the addition of further flow. This ratio increased presumably for two reasons: 1) the increasing pressure in the PS (for PG flow up to 5.5 sccm) generated more $H_3^+$ and produced $N_2H^+$, and 2) the probability of initially formed $N_2^+$ to react with $H_2$ to form $N_2H^+$ increases with increasing pressure.

However, the increasing ratios are observed only up to a flow of 5.5 ± 0.5 sccm. Beyond that, this ratio declined. Moreover, the ratio of $N_2H^+$ to $H_3O^+$, decreases with the flow. The protonation of water molecules from $N_2H^+$, thus $H_3O^+$ is dependent on the reactant ion. In addition, we have observed in *Figure 4.2* that an increased pressure produces more $H_3O^+$ ions. Therefore, the $N_2H^+/H_3O^+$ ratio has decreased with increasing PG flow.

*Table 2: The ratio of $N_2H^+/N_2^+$ and $N_2H^+/H_3O^+$*

| PG Flow (sccm) | $N_2H^+/N_2^+$ | $N_2H^+/ H_3O^+$ |
|---|---|---|
| 2.5 | 2 | 173 |
| 3.0 | 5 | 99 |
| 3.5 | 11 | 70 |
| 4.0 | 27 | 51 |
| 4.5 | 68 | 34 |
| 5.0 | 135 | 27 |
| 5.5 | 177 | 20 |
| 6.0 | 180 | 16 |
| 6.5 | 163 | 13 |
| 7.0 | 131 | 11 |
| 7.5 | 106 | 9 |

In the previous experiment, when PG was added, the ion $N_2H^+$ remained constant while the $N_2^+$ intensity dropped significantly with increasing PG. In this case, the system was suspected of having a small leak, allowing lab air to be introduced into the PS. After having fixed this leakage issue, the $N_2H^+$ maximum abundance was observed at 5.5 sccm flow (cf. *Figure 4.19*). Below this flow, ion production was limited by inadequate plasma conditions. The optimal balance between ion generation and impurity control was achieved between 5.5 and 6.0 sccm of PG flow.

### 4.1.4 Plasma Gas Flow with Constant Analyte Flow

The PG flow without analyte flow has been performed in the previous section. However, the analyte must be introduced into the MS system to be analyzed. Therefore, $N_2$ gas has been introduced into the reaction chamber through a 2.5-meter-long fused silica sample line. Since the reaction chamber maintains a medium pressure range (2.0-15.0 mbar), the analyte gas flow can be added up to approximately 4.0 sccm. However, in this experiment, the $N_2$ gas was added to the reaction chamber with 3.0 sccm flow using a calibrated flow controller. To optimize the PS, a mixing $N_2/H_2$ PG with varying flow (1.0 – 6.0 sccm) was introduced to the PS, while the analyte flow remained constant. The $N_2^+$ and $N_2H^+$ ion abundances were recorded, which are shown in *Figure 4.20*. At a PG gas flow of 3.5 sccm (total gas flow 6.5 sccm), the maximum ion abundance ($(3.96 \pm 0.02) \times 10^{11}$ cps) is observed at m/z 29, corresponding to the $N_2H^+$ ion. Therefore, all measured ion abundances are normalized to this ion abundance and plotted as the relative intensity on the respective y-axis. The x-axis shows the total gas flow in the system.

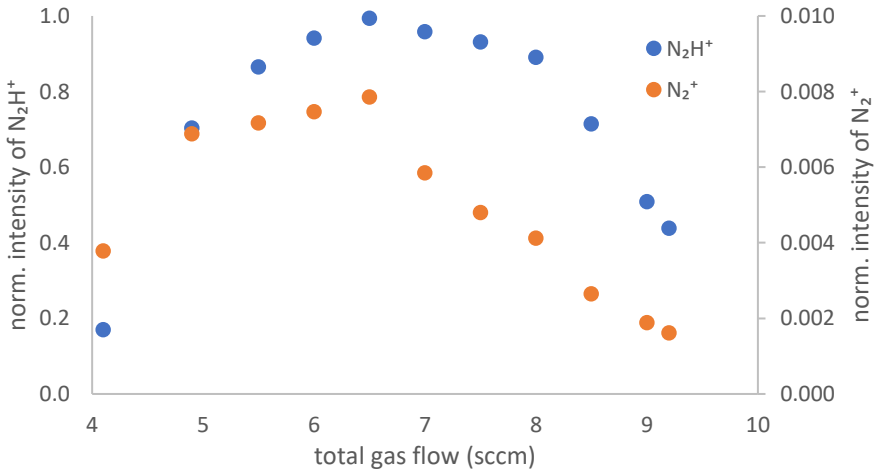


*Figure 4.20: Ion dependency on total gas flow (PG and analyte gas) with a constant analyte gas flow rate of 3.0 sccm. The relative ions $N_2H^+$ and $N_2^+$ are indicated in blue and orange, respectively.*

It is observed that the relative $N_2H^+$ ion intensity at a lower total flow rate (4.0 sccm) produced 17% of the maximum ion intensity (cf. *Figure* 4.20). This ion intensity increased by further increasing the gas flow. As mentioned in the previous section, the pressure of the PS increases with increasing gas flow. Consequently, the collision frequency increases, enhancing the total ion formation in the plasma as well as the extend of ion-molecule reactions, both resulting in

more reactant ion formation. At 5.0 sccm and 6.0 sccm, the relative ion intensity increased to about 70% and 94%, respectively, and continued to increase up to 6.5 sccm. Beyond a gas flow rate of 6.5 sccm the ion intensity showed a pronounced decline. The $N_2H^+$ ion intensity is dropped to approximately 96%, 89% and 50% at 7.0 sccm, 8.0 sccm, and 9.0 sccm, respectively.

In the previous experiment, the maximum ion intensity was observed at a PG flow rate of 5.5 sccm (without analyte flow) (cf. *Figure 4.19*) into the PS. However, in this experiment, the maximum ion intensity has been observed at a total flow rate of 6.5 sccm. At this total flow rate, the pressure in the plasma source stabilizes at 8.0 mbar.

The same trend is shown in this experiment for the $N_2^+$ ion, which is generated by direct electron ionization with free plasma electrons. The relative ion intensity is observed to be approximately 1% of the $N_2H^+$ population at 6.5 sccm gas flow (shown in *Figure 4.20*). However, this $N_2^+$ intensity is 40% higher than that without the analyte (cf. *section 4.1.3*).

The optimal ion intensity when introducing only PG was observed at a flow rate of 5.5 sccm in the previous experiment (cf. in *Figure 4.19*). However, in this experiment, the reactant ion can be generated with a maximum intensity at a total gas flow rate (including 3.0 sccm of analyte) of 6.5 sccm. Therefore, the following experiments were conducted at 6.5 ± 0.5 sccm and 5.5 ± 0.5 sccm with and without analyte flow, respectively.

## 4.2 Distance Variation of the Plasma Ion Source

The HPCI source used in this study, as shown in *Figure 3.1*, consists of an HR, a glass tube, and an RF power supply. The position of the HR along the glass tube is adjustable, and variations in this position can significantly influence the behavior and relative abundances of the reactant ions ($N_2H^+$ and $N_2^+$). Accordingly, this section investigates the dependence of reactant ion behavior on the HR position. Measurements were performed at three discrete HR positions, corresponding to 100 mm, 110 mm, and 120 mm, defined as the plasma source distance (PSD). The PSD is measured from the center of the HR to the end of the glass tube.

In the previous section (cf. *section 4.1.2*) it was mentioned that the intensity related to $N_2H^+$ remains constant over a pressure range of 1.0 – 1.7 mbar. Accordingly, in the present experiment, the reaction chamber pressure was maintained at 1.7 mbar by introducing PG and $N_2$ into the system. Under these controlled pressure conditions, the intensities of $N_2^+$ and $N_2H^+$ were measured at three PSDs, as shown *Figure 4.21*. The dependence of $N_2H^+$ and $N_2^+$ ion intensities on PSD is represented by the blue and orange dashed lines, respectively. Ion intensities on the y-axis are normalized to the $N_2H^+$ intensity measured at a PSD of 110 mm, allowing direct comparison of relative ion behavior as a function of HR position.

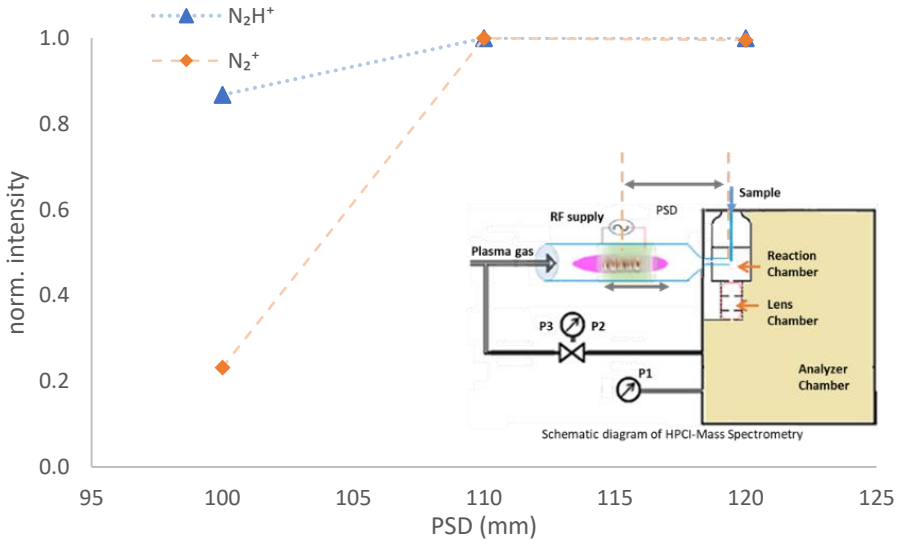


*Figure 4.21: Dependence of $N_2H^+$ and $N_2^+$ intensities on the PSD is shown, with the respective ion intensities.*

In this figure, the maximum ion intensity is observed at 110 nm. Interestingly, at this pressure the reactant-ion intensity of a 100 mm PSD is lower than that of a 110 mm PSD, though the latter is further away from the entrance of the mass spectrometer. At this 100 mm distance, the relative ion intensities of $N_2H^+$ and $N_2^+$ were 87% and 23%, respectively. The experimental data also show (in *Figure 4.21*) that the intensities remain virtually constant when further increasing this distance to 120 mm.

This dependency is required to be investigated at higher pressures following the modification of the reaction chamber. Accordingly, the subsequent experiments were conducted.

*Ion dependency on PSD without analyte gas*

After having fixed the sealing issue between the PS glass tube and the reaction chamber, the PS was initially optimized using only the PG flow. It was previously observed that a 12% $N_2/H_2$ mixing PG generates a maximum $N_2H^+$ intensity at a flow rate of 5.5 sccm. Therefore, the ion dependencies on the PSDs of 100 mm, 110 mm, and 120 mm were also measured for this flow condition. Here at the PSD position of 100 mm, the reactant ion $N_2H^+$ is recorded as a base peak, along with species such as $H_3O^+$ and $N_2^+$ at m/z 19 and 28, respectively. The measurements at all PDSs have been normalized to the intensity of each ion at 100 mm PSD in *Figure 4.22*. The PSD in mm and the normalized intensity are shown on the x-axis and y-axis, respectively.

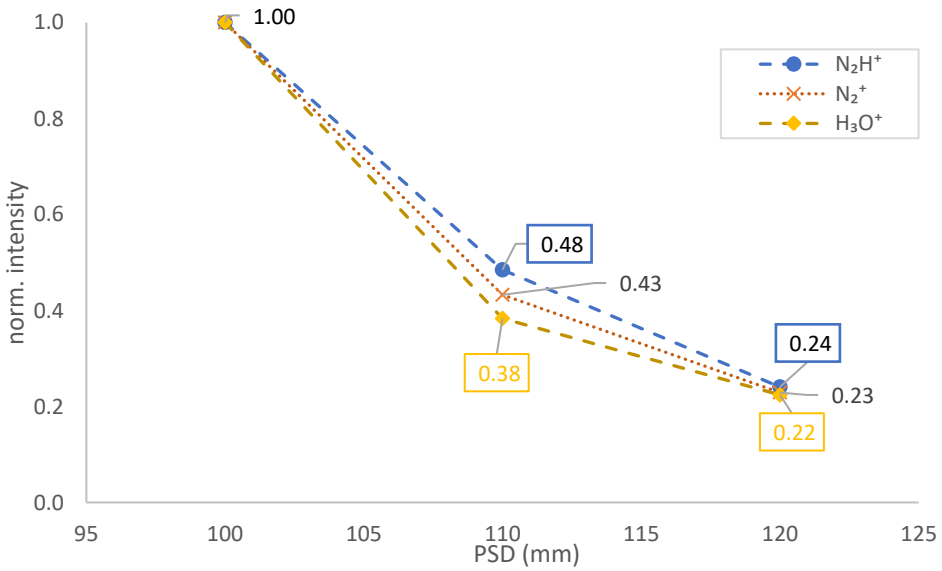


*Figure 4.22: Dependence of ions of 12% $N_2/H_2$ mixing PG on PSD. Plasma gas $N_2/H_2$ 5.5 sccm was added to maintain the optimum reaction chamber pressure of 7.0 mbar.*

When the PSD was set to 110 mm, a substantial reduction in the intensity of the $N_2H^+$ reactant ion was observed. Specifically, the $N_2H^+$ signal decreased by approximately 52 ± 2% relative to its intensity at the initial PSD of 100 mm. A similar trend was observed at a PSD of 120 mm, where the $N_2H^+$ intensity decreased by approximately 76 ± 1% compared to the 100 mm position. In parallel, increasing the PSD by 10 mm and 20 mm likewise led to significant reductions in the intensities of the $N_2^+$ and $H_3O^+$ ions, with decreases of approximately 60 ± 3% and 77 ± 1%, respectively, relative to their intensities at the 100 mm PSD.

*Ion dependency on PSD with constant plasma gas flow and sample flow ($N_2$)*

It is important to note that the previous experiment was conducted by only introducing PG into the system. However, the analyte flow must be considered as well. Initially, only $N_2$ was added as the analyte gas, while an $N_2/H_2$ mixture served as the PG. Both gases were introduced into the MS system at a combined flow rate of 6.5 sccm resulting in an overall plasma source pressure of 8.0 mbar. Under these conditions, the abundances of $H_3O^+$, $N_2^+$, and $N_2H^+$ ions were recorded at the three PSDs of 100, 110, and 120 mm. The corresponding ion abundances at each PSD are shown in *Figure 4.23*, with all intensities normalized to the intensity of each ion at 100 mm PSD.

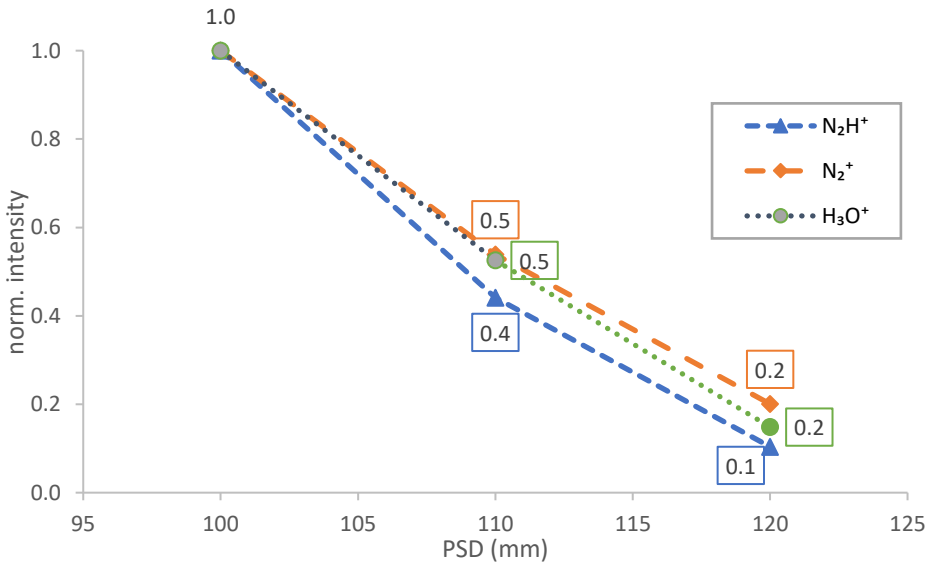


*Figure 4.23: $N_2H^+$, $N_2^+$ and $H_3O^+$ dependency on PSD with a total flow of 6.5 sccm of 12% $N_2/H_2$ PG and $N_2$ sample gas.*

As shown in *Figure 4.23*, the $N_2H^+$ intensity at a PSD of 110 mm is reduced by 60 ± 6% relative to the intensity measured at 100 mm, while at a PSD of 120 mm the reduction reaches 90 ± 5%. In the preceding experiment conducted without analyte introduction, the corresponding decreases in $N_2H^+$ intensity were 52% and 76% at PSDs of 110 mm and 120 mm, respectively. A similar trend is observed for protonated water ions ($H_3O^+$), whose intensity decreases with increasing PSD, attributable to the reduced availability of the reactant ion $N_2H^+$.

Upon introduction of $N_2$ into the reaction chamber, $N_2^+$ ions are additionally generated via electron ionization with free plasma electrons. At a PSD of 100 mm, the absolute $N_2^+$ intensity is (1.5 ± 0.2) × $10^9$ cps. This signal decreases by 50 ± 6% at 110 mm and by 80 ± 5% at 120 mm. In the previous experiment performed in the absence of $N_2$ sample flow, the ratio of $N_2H^+$ to $N_2^+$ ion intensities remained constant at 126 ± 6 across all PSD positions, reflecting ion formation solely within the plasma source, aside from minor contributions from impurity ions in the reaction chamber. In contrast, with the $N_2$ sample flow present, the $N_2H^+/N_2^+$ intensity ratio decreases systematically with increasing PSD, exhibiting values of 125, 102, and 65 at PSDs of 100, 110, and 120 mm, respectively.

The potential influence of proton-transfer reactions on the transport and diffusion of the reactant ions must also be considered. To investigate this effect, a subsequent experiment employing a BTX-mixed sample flow was conducted and is discussed in the following section.

*Ion dependency on PSD with constant plasma gas flow and sample flow (BTX)*

In the previous experiment, $N_2$ gas was introduced into the reaction chamber; however, proton-transfer reactions with the reactant ions ($N_2H^+$) did not occur because the interacting species possess identical proton affinities. Consequently, BTX was selected as the analyte in the subsequent experiment, as it provides a higher PA than $N_2H^+$. In this experiment, a 12% $N_2/H_2$ gas mixture was employed as PG, while a BTX/SA mixture was introduced via the sample inlet into the MS system. Accordingly, data were recorded at different PSDs and resulting profile spectra of the BTX at 100 and 120 mm PSD are shown in the *Upper Figure 4.24*. The x-axis and y-axis of these spectra show the m/z and the relative intensity, respectively. The molecules benzene, toluene, and o-xylene in the BTX mixing are denoted Mb, Mt, and Mx, respectively.

The molecular ions $M^+$ and protonated molecular ions $MH^+$ of the BTX analyte measured at different PSDs are presented in the lower *Figure 4.24*. The intensities of these ions (including $N_2^+$ and $N_2H^+$) are normalized to their respective values measured at a PSD of 100 mm. In this figure, the x-axis represents the PSD, while the y-axis denotes the relative ion intensity.

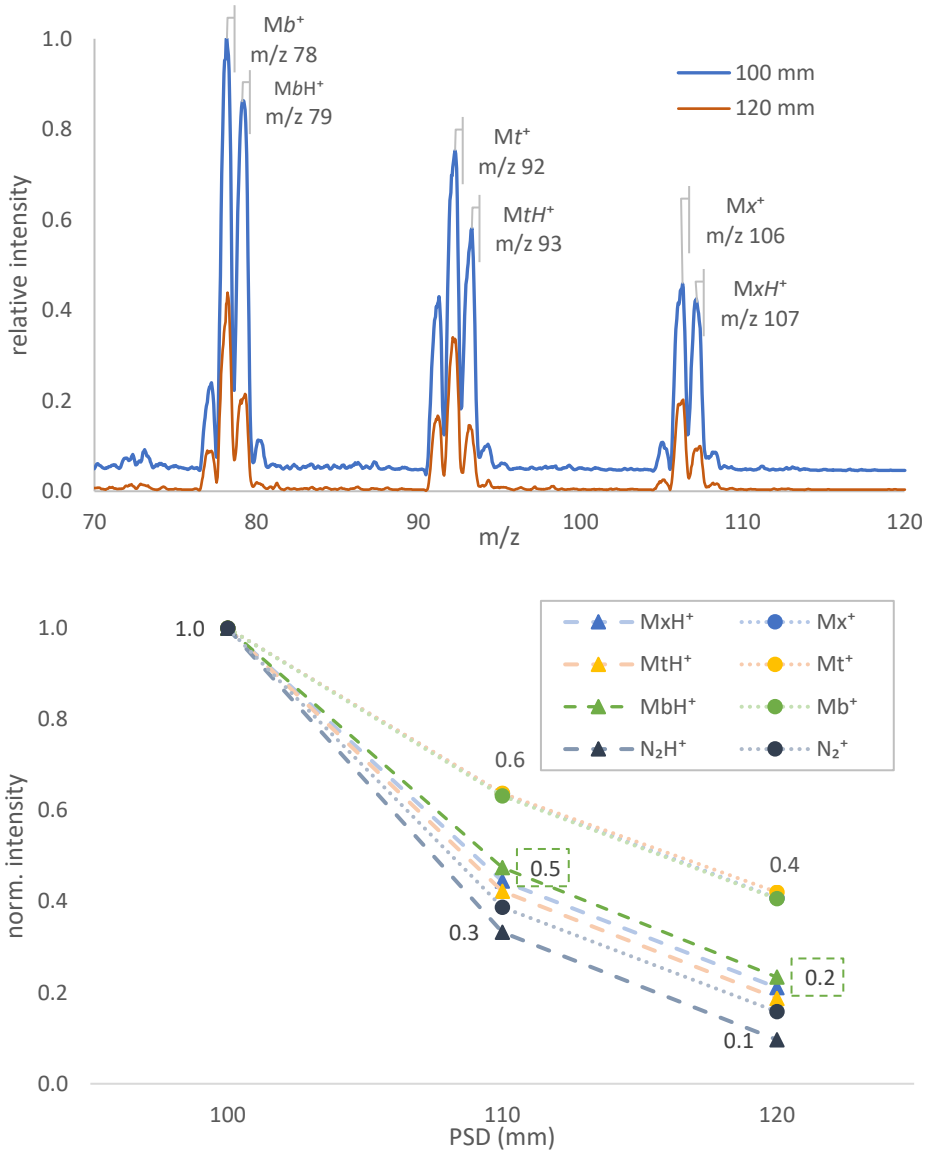


*Figure 4.24: Profile spectra of BTX mixing on different PSD (upper); Ion intensity of BTX mixing at 8.0 mbar pressure with 12% $N_2$ in $H_2$.*

In this section, the intensities of the $M^+$ and $MH^+$ are measured at different PSDs, and the dependence of these ion intensities on the PSD is discussed. However, the formation of the molecular ions of BTX has been discussed in the following *section 4.7.1*.

In the profile spectra, the molecular and quasi-molecular ions ($M^+$ and $MH^+$) are observed at m/z 78 and 79 for benzene, m/z 92 and 93 for toluene and m/z 106 and 107 for o-xylene. These ions at 100 mm PSD are much higher than those at 120 mm PSD. These observations give an overview of the effect of ion intensity dependence on the PSD.

However, for quantitative analysis, the $MH^+$ for benzene, toluene, and o-xylene from the BTX mixing has been shown in the lower *Figure 4.24* as green, gray, and blue, respectively. It is observed that the $MH^+$ signal intensities of the BTX components decreased by approximately 55 ± 5% and 78 ± 5% when the PSD was adjusted to 110 mm and 120 mm, respectively. This $MH^+$ is formed by proton transfer reaction between $N_2H^+$ and M. In this case, the analyte flow remained constant.

However, for the reactant ion $N_2H^+$ (shown dash blue-gray in the lower *Figure 4.24)*, the ion intensity decreases with increasing plasma source distance. Specifically, when the PSD increases from 100 mm to 110 mm and 120 mm, the $N_2H^+$ intensity is reduced by 67 ± 3% and 90 ± 3%, respectively. Consequently, the intensity of the corresponding product ions also decreases.

In contrast, the formation of $M^+$ is due to photoionization from plasma fluorescence (for details, cf. *section 4.7.1*). From the perspective of photoionization, the plasma fluorescence effect reduces with increasing PSD. Accordingly, molecular ion ($M^+$) intensities of the analytes are also decreased by approximately 36 ± 5% and 59 ± 5% at PSDs of 110 mm and 120 mm, respectively.

The analyte ion intensity exhibits a strong dependence on the plasma source distance (PSD), with a clear decrease observed with increasing distance. This decrease is due to a decrease in the number of reactant ions entering the reaction chamber. As the reactant ions move from the HPCI source to the reaction chamber, the number of reactant ions decreases due to wall losses. Therefore, positioning the HPCI source close to the reaction chamber is essential to minimize reactant-ion losses.

## 4.3 Different Analyte Flow with Constant Plasma Gas Flow

In the preceding section, the dependence of ion intensities on the PSD was investigated, and it was observed that increasing the PSD leads to a reduction in reactant ion concentration within the glass transfer tube. Accordingly, the following experiments examine the dependence of ion intensities on the analyte gas flow while the PG flow with 12% $N_2/H_2$ is held constant at 3.0 sccm and the PSD is fixed at 100 mm. The experimental results show distinct ion-intensity responses as a function of analyte flow rate, as reflected by the measured molecular $M^+$ and quasi-molecular $MH^+$ ion intensities of a BTX mixture with 10.6 ppmV benzene, 9.9 ppmV toluene and 9.5 ppmV xylene, respectively.

The BTX mixture was introduced into the reaction chamber through the sample line with initially ~1.0 sccm, yielding a total flow of 4.0 sccm (including PG). The total flow in the PS and reaction chamber was then increased to 7.0 sccm by adding additional analyte flow. Under these conditions, the intensities of different ions at various gas flow rates were recorded, and the relative intensities are plotted on the y-axis of *Figure 4.25.*

The analyte ions are denoted $Mb^+$ and $MbH^+$ for benzene, $Mt^+$ and $MtH^+$ for toluene, and $Mx^+$ and $MxH^+$ for o-xylene. The upper and lower panels show the reactant ions ($H_3O^+$, $N_2^+$, $N_2H^+$, and $O_2^+$) and analyte ions, respectively, as functions of the total gas flow in the system. The intensities are normalized to the intensities of $N_2H^+$ and $M^+$ at 5.5 sccm flow for the y-axes of the lower and upper panels, respectively.

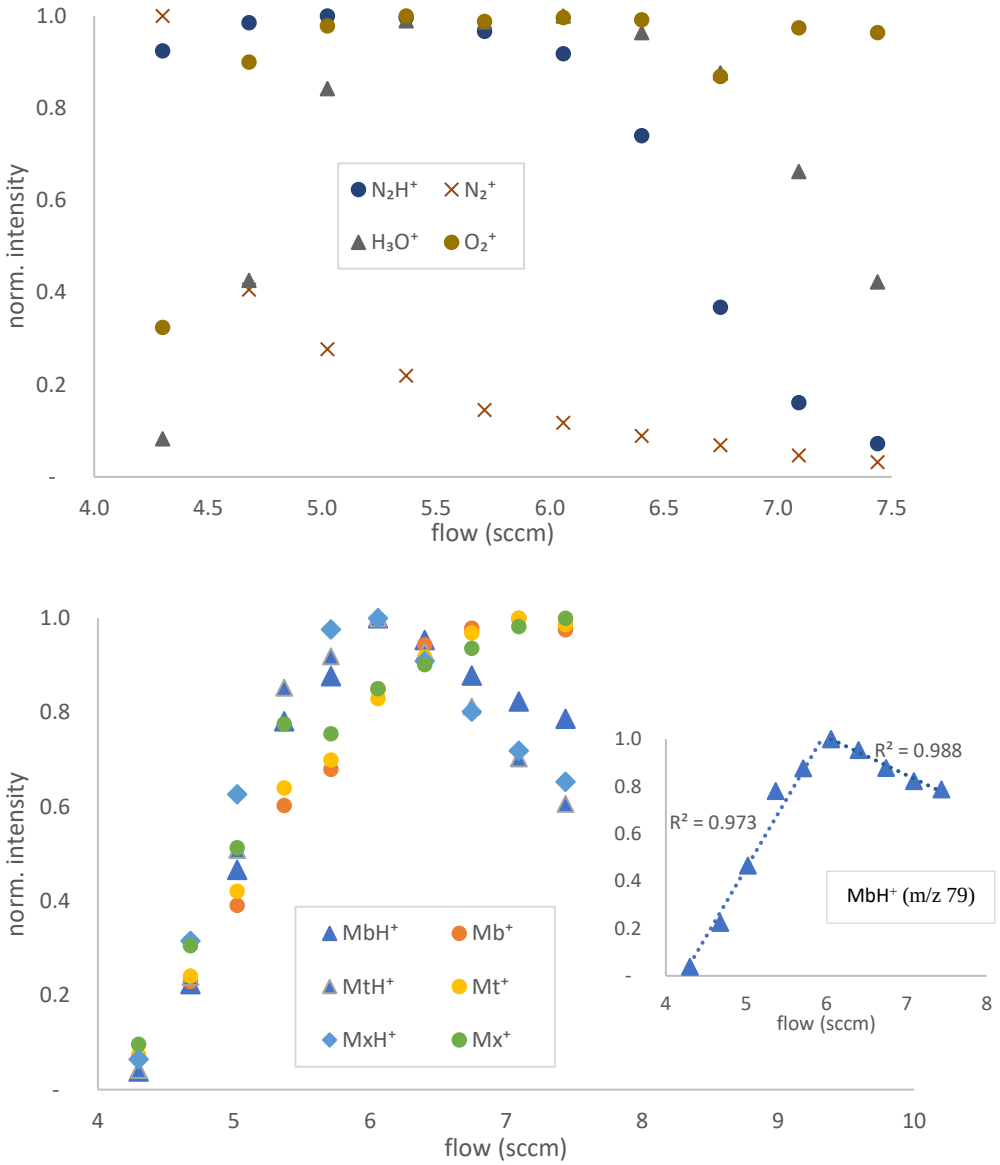


*Figure 4.25: Dependence of reactant ions (upper) and analyte ions (lower) of the analyte (BTX/SA mixing gas) flow. The linear curve of $M_bH^+$ (m/z 79) with flow rate is shown inside the lower figure.*

From the upper panel, the relative intensity of the principal reactant ion, $N_2H^+$, remains approximately constant for total gas flows up to 6.0 sccm. Beyond 6.0 sccm, the intensity decreases. This downward trend was likewise observed in the ion-dependence measurements across different PG flows with a fixed analyte flow (cf. *section 4.1.4*). Thus, the reactant-ion intensity is effectively stable up to a total gas flow of 6.0 sccm.

Because the formation of $H_3O^+$ is strongly pressure-dependent, its intensity is lower at small gas flow rates and increases with rising flow, mainly due to favoring the protonation reaction between $N_2H^+$ and $H_2O$. At gas flow rates from 5.0 to 6.5 sccm, the $H_3O^+$ intensity remains essentially constant; beyond this range, it begins to decrease, similar to the behavior observed for $N_2H^+$, because less $N_2H^+$ will also diminish the protonation step to $H_3O^+$.

As noted earlier, $N_2^+$ is formed solely by electron-impact ionization from the free plasma electrons, whereas $O_2^+$ can arise from both electron ionization and photoionization. The $N_2^+$ signal shows a continuous, steep decrease with increasing gas flow (cf. upper panel of *Figure 4.25)*. In stark contrast, $O_2^+$ formation increases markedly with increasing sample gas flow. The $O_2^+$ intensity rises up to a total gas flow of 5.0 sccm, after which it remains essentially constant. This behavior can be explained by the dual ionization pathways for $O_2^+$ and by its limited reactivity with $H_2$, $N_2$, or $H_2O$; $O_2^+$ can only ionize the BTX components via electron transfer under these conditions.

The proton-transfer reaction *Rn 1,* in which a proton from the reactant ions $N_2H^+$ and $H_3O^+$ to the analyte, producing $MH^+$. When the densities of the reactant ions are fixed, $MH^+$ formation is governed by the neutral-analyte concentration. The lower panel of *Figure 4.25* shows that $MH^+$ intensity increases with analyte flow from 4.0 to 6.0 sccm, exhibiting a good linear correlation ($R^2 = 0.973$) for protonated BTX species (e.g., benzene $MH^+$). The maximum $MH^+$ intensity for the BTX mixture occurs at an analyte flow of 2.8 ± 0.5 sccm, corresponding to a total flow of approximately 6.0 sccm (including PG). From chemical kinetics, product-ion formation increases with increasing neutral analyte concentration and with higher concentrations of the reactant ions $N_2H^+$ and $H_3O^+$, as demonstrated in *Figure 4.25*. However, when the analyte flow has been further increased beyond this point (2.8 sccm), up to 4.5 sccm (total 7.5 sccm, including PG), an inverse relationship between the analyte flow and $MH^+$ ion intensity was observed. Specifically, higher flow corresponded to a decrease in ion signal, with a good linear correlation coefficient of $R^2 = 0.988$ for $MbH^+$. In this case, the reactant ions are decreased with increasing total flow. The higher gas flow results in a higher pressure. The higher pressure affects the production of reactant ions, and consequently, fewer protonated ions are generated. Specifically, for the reactant ion $N_2H^+$ shown in the upper *Figure 4.25*, the gas flow range of 4.0 sccm to about 6.0 sccm did not affect reactant ion generation, whereas increasing the flow reduced the reactant ion. Consequently, the protonated analyte $MH^+$ intensity is observed to be lower as well.

In contrast, the intensities of molecular ions for BTX analytes are increased with increasing analyte flow. Since the $M^+$ ion is produced through either photoionization or an electron transfer reaction between the $O_2^+$ ion and neutral molecules (M) (cf. details in the *section 4.7.1*), the intensity of molecular ions is increased with increasing analyte flow.

The empirical data showed that the optimum $MH^+$ intensity for each compound within the BTX mixture is observed at a total gas flow of 6.0 ± 0.5 sccm (including PG). However, this chamber pressure has been maintained at 8.0 ± 0.5 mbar. The dependency of the BTX molecular ions on chamber pressure (by varying analyte flow) is discussed in the analytical measurement section (cf. *Section 4.7.1*).

## 4.4 Analyte Inlet Positions in Reaction Chamber

During entry into the reaction chamber, the sample gas undergoes rapid dispersion under the prevailing vacuum, promoting uniform distribution of the analyte molecules. The reactant ions enter the chamber at a 90-degree angle to the sample line (cf. *Figure 3.1*). The analyte inlet position inside the reaction chamber can be adjusted by translating the sample line (cf. *Figure 4.26*); a base position of 0 mm places the inlet near the glass tube of the ion source, while positive and negative values correspond to forward and backward displacements, respectively. In this study, 12% $N_2/H_2$ was used as the plasma gas and 12.6 ppmV toluene/synthetic air as the analyte (M). With $N_2H^+$ reactant ions and toluene present, protonation yields $MH^+$ via the protonation reaction *Rn 1*. Consequently, the $MH^+$ ion intensity was recorded at several sampling positions and is displayed on the logarithmic y-axis in *Figure 4.26*. Five distinct sampling positions were examined, as indicated on the x-axis of the figure.

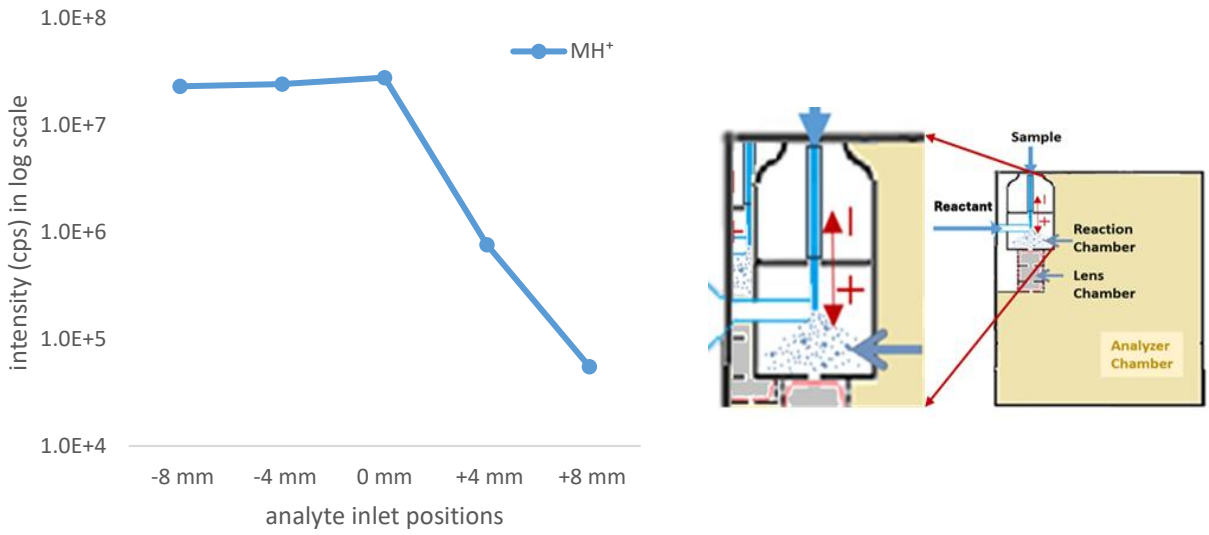


*Figure 4.26: Dependence of $MH^+$ on different analyte inlet positions. The '-' and '+' signs indicate the back and forth movement of the sample line with respect to the 0 mm base position exactly in front of the 90° angled reactant ion inlet from the plasma source.*

Positioning the analyte inlet at -4 mm or -8 mm relative to the 0 mm reference results in broader dispersion of the analyte molecules within the chamber prior to interaction with the reactant ions, thereby reducing the spatial overlap between the analyte and reactant ion concentrations. Accordingly, the observed reductions in $MH^+$ intensity of approximately 13 ± 1% and 18 ± 1%

for sample-line retractions to -4 mm and -8 mm, respectively, can be readily rationalized on the basis of chemical-kinetic considerations.

Positioning the analyte outlet at +4 mm and +8 mm downstream from the reactant ion introduction reduces the effective reaction time and dilution of the analyte. Consequently, the probability of productive collisions between reactant ions and analyte molecules decreases markedly, leading to a substantial drop in ion signal of approximately 97.0% and 99.8% for the +4 mm and +8 mm positions, respectively. In contrast, at the 0 mm reference position—the alignment of the glass tube of the ion source and the analyte inlet within the reaction chamber—the concentration overlap and thus the likelihood of collisions is maximized, supporting efficient analyte ionization. Any deviation from this optimal alignment, whether upstream or downstream, markedly degrades ionization efficiency.

## 4.5 Sample Transfer Line and Reaction Chamber Temperature

As mentioned in the experimental section of the GC–MS system, following the separation column, the effluent is divided between two sample lines: one connected to the GC detector and the other to the MS system. The transfer of the sample from the GC to the MS is accomplished through a fused silica capillary with an inner diameter of 0.25 mm. In addition to the sample line supplied from the GC, a second fused silica capillary with an inner diameter of 0.25 mm is connected to the MS system to allow for continuous sampling of ambient air without chromatographic separation. Both capillaries are embedded into a temperature-controlled transfer line, adjustable in the range of 25 to 350 °C. In principle, both inlets can be used for analysis, however, for characterization of the HPCI system only the second sample line is used and connected to an actively controlled flow controller to maintain a constant analyte flow into the source.

In this section, the effect on ion intensities by varying the sample transfer line and reaction chamber temperature was investigated. A BTX/synthetic air gas mixture was introduced through the sample line with a constant flow rate of 3.0 sccm. A 12% $N_2/H_2$ mixture was used as the plasma gas with a flow rate of 3.5 sccm. Setpoints for the transfer line temperature were 80 °C, 120 °C, 150 °C, and 180 °C. Note, throughout this experiment the reaction chamber temperature was set to the same value as the transfer line. The ion intensities of $N_2H^+$ (at m/z 29) as the reactant, and $M^+$ (at m/z 78) and $MH^+$ (at m/z 79) for benzene as the analyte were recorded at the mentioned temperatures and plotted in *Figure 4.27*. The intensities are normalized to the respective maximum at 80°C and plotted on the y-axis, while the x-axis shows the transfer line/reaction chamber temperature in °C.

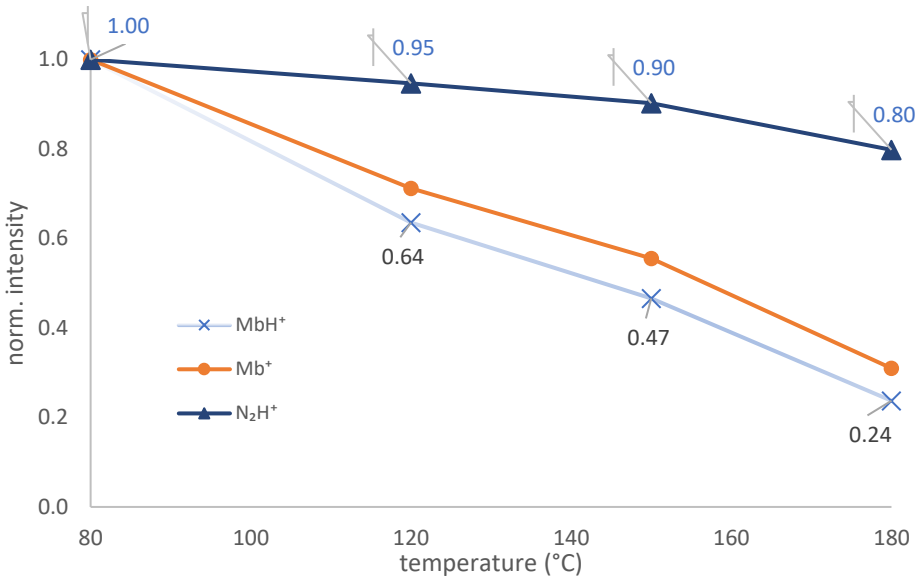


*Figure 4.27: Dependence of ion signals on varying transfer line and reaction chamber temperatures. Signal intensities were normalized to the respective intensities at 80°C.*

At 80 °C, the ion intensities corresponding to both reactant and molecular ions exhibited the highest intensity within the investigated temperature range. Experimental results show a clear inverse relationship between temperature and ion intensity. All the BTX ions showed the same trend. However, only benzene is shown in this figure as a representative species.

The intensity of the protonated benzene ($MH^+$) linearly decreased by approximately 75% relative to the measured intensity at 80 °C when the temperature was increased to 180 °C. At 120 °C and 150 °C the intensities had dropped by 36 % and 53%, respectively. The intensity of the molecular ion ($M^+$) showed very similar behavior. The reason for this effect is not quite understood. As mentioned before, the sample flow rate was maintained at 3.0 sccm throughout this experiment, therefore it cannot be attributed to a flow effect through the capillary potentially changing the partial pressures. The overall pressure inside the reaction chamber did not change as well. The gas-phase viscosity increases as temperature rises, however, if this affects the outflow, subsequent ionization reactions and also the transmission efficiency remains speculative [67].

From a kinetic perspective (Reaction *Rn 5*), the formation of protonated analyte depends on the concentrations of both the analyte and the reactant ions. The reactant ion $N_2H^+$, however, exhibits relatively minor variations with changes in the sample line and reaction chamber temperature compared to the analyte ions. At a transfer line temperature of 180 °C, the relative $N_2H^+$ intensity decreases by approximately 20%, whereas at 120 °C and 150 °C, the corresponding decreases are limited to about 5% and 10%, respectively.

As discussed in *Section 4.1.2*, elevated pressure can lead to a reduction in reactant ion intensity, however, the overall pressure inside the chamber and the plasma remained constant. Hence, this effect remains unclear. Nevertheless, this experiment suggests that lowering the transfer line temperature enhances the analyte ionization efficiency.

## 4.6 Impact of Repeller Potential

Analyte molecules are ionized in the reaction chamber and exit through a small aperture into the high-vacuum region of the instrument. In this section it was of interest, if an additionally applied voltage to the repeller inside the source (cf. details in the *section 3.4*) might be beneficial to the overall performance. Therefore, a positive DC potential was applied to the repeller plate through an external power supply to additionally force the positively charged ions in the direction of the exit aperture of the reaction chamber.

A toluene/synthetic-air gas mixture (12.6 ppmV) was introduced into the reaction chamber as the analyte with a flow rate of 4.0 sccm. Reactant ions were generated in the HPCI source with a 12% $N_2/H_2$ plasma gas mixture at a flow rate of 2.5 sccm. A DC potential was applied to the repeller plate and varied from 0 to 75 V. The corresponding ion intensities, including that of $N_2H^+$, were recorded and are presented in *Figure 4.28*. In this figure, the x-axis represents the applied potential in volts, while the y-axis shows the ion intensities on a logarithmic scale.

As illustrated in *Figure 4.28*, the intensity of $N_2H^+$ increases with increasing repeller plate potential by nearly an order of magnitude between 0 V and 45 V, and remains constant beyond that.

In contrast, the recorded intensity of the protonated toluene ($MH^+$) as well as the molecular ion ($M^+$) remain relatively constant over the applied repeller plate potential range from 0 to 75 V, as indicated by the blue triangle and dot in *Figure 4.28*, respectively. A maximum $MH^+$ intensity of $(2.9 \pm 0.8) \times 10^7$cps is observed at an applied potential of 40 V. The minimum intensity within this potential range is recorded at $(2.2 \pm 0.7) \times 10^7$cps, which lies within the uncertainty of the maximum value, indicating no statistically significant variation in the $MH^+$ population with an additionally applied voltage to the repeller. Absolute intensity assigned to the $M^+$ population varies between $(11.3 \pm 2.2) \times 10^7$cps and $(25.0 \pm 2.6) \times 10^7$cps.

Additionally, a negative repeller potential of up to −40 V was intentionally applied, resulting in a reduced ion intensity due to electrostatic attraction of the positively charged ions toward the repeller plate. Overall, these observations indicate that the external repeller potential does not enhance protonation efficiency in this system. Consequently, subsequent experiments were conducted without applying an external repeller voltage and it remained grounded.

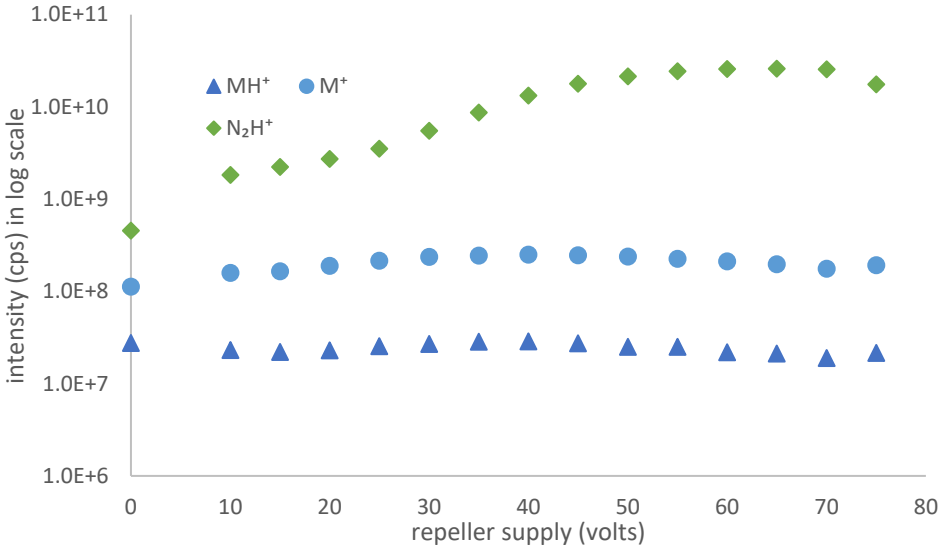


*Figure 4.28: Dependence of the recorded $MH^+$ and $M^+$ ion populations of toluene and the reactant ion, $N_2H^+$, on an additionally applied repeller potential in the reaction chamber. A DC voltage range of 0 to 75 V was applied.*

## 4.7 Measurement of Analyte Using Different Reactants

In the preceding sections, the PS parameters (*sections 4.1 and 4.2*) and sampling methodology (*sections 4.3 to 4.6*) were systematically optimized. In the present section, analyte molecules are investigated using different reactant ions generated by the HPCI source. Reactant ions play a critical role in the ionization of analyte molecules, particularly in chemical ionization (CI) techniques. In the HPCI–MS system, $H_2$ gas and an $N_2/H_2$ gas mixture are employed as reagent gases to generate reactant ions, with $H_3^+$ and $N_2H^+$ expected to be the dominant species, respectively. However, as discussed in the *section 4.1*, the ion source also produces additional ions, including $H_3O^+$, $N_2^+$, $N_2H^+$, and $O_2^+$. These ions, together with the primary reactant ion $H_3^+$, can undergo ion–molecule reactions with analytes within the reaction chamber. The BTX mixing gas and a series of alcohol mixtures, as aromatic compounds and as oxygenated compounds, respectively, are introduced into the system as analyte gas. Therefore, the reaction rate coefficients of possible reactions between reactants generated from the HPCI source and analytes are shown in *Table 3*.

*Table 3: Reaction rate constants, k for reactions of $H_3^+$, $H_3O^+$, $N_2^+$, $N_2H^+$ and $O_2^+$ with aromatic compounds and alcohols* [68–71]

| **Molecules** | **k ($H_3^+$)** ($10^{-9}\ cm^3 \cdot s^{-1}$) | **k ($H_3O^+$)** ($10^{-9}\ cm^3 \cdot s^{-1}$) | **k ($N_2^+$)** ($10^{-9}\ cm^3 \cdot s^{-1}$) | **k ($N_2H^+$)** ($10^{-9}\ cm^3 \cdot s^{-1}$) | **k ($O_2^+$)** ($10^{-9}\ cm^3 \cdot s^{-1}$) |
|---|---|---|---|---|---|
| $C_6H_6$ | 3.3 | 1.9 | 1.6 | 1.5 | 1.6 |
| $C_7H_8$ | 3.9 | 1.3 | 1.9 | 1.7 | 1.7 |
| $C_8H_{10}$ | 4.1 | 2.4 | 4.1 | 1.9 | 1.9 |
| $CH_3OH$ | 2.9 | 2.8 | 1.4 | 1.7 | 1.0 |
| $C_2H_5OH$ | 5.0 | 2.8 | - | - | 2.3 |
| $C_3H_7OH$ | 5.0 | 2.7 | - | - | 2.2 |
| $C_4H_9OH$ | - | 2.8 | - | - | 2.3 |

### 4.7.1 Measurement of Aromatic Compounds using $N_2/H_2$ reagent

*Toluene/synthetic air measurement*

In this experiment, 12% $N_2/H_2$ mixing gas was introduced into the plasma source. A mixture 12.6 ppmV of toluene ($C_7H_8$) in synthetic air (SA) and for comparison only SA were added via the sample inlet to the reaction chamber. The PG and sample were added with flow rates of 3.0 and 3.5 sccm, respectively. The recorded mass spectra of the mixture and SA are presented in *Figure 4.29*, where the *x*-axis represents the *m/z* and the *y*-axis indicates the relative intensity (%). The relative intensity of the observed toluene ions ($MH^+$, $M^+$, $M(-H)^+$, and $M(-CH_3)^+$) within the m/z range 70 –100 and reactant ions ($H_3O^+$, $N_2H^+$ and $O_2^+$) within the m/z range 10–70 are shown in the right figure and left figure, respectively.

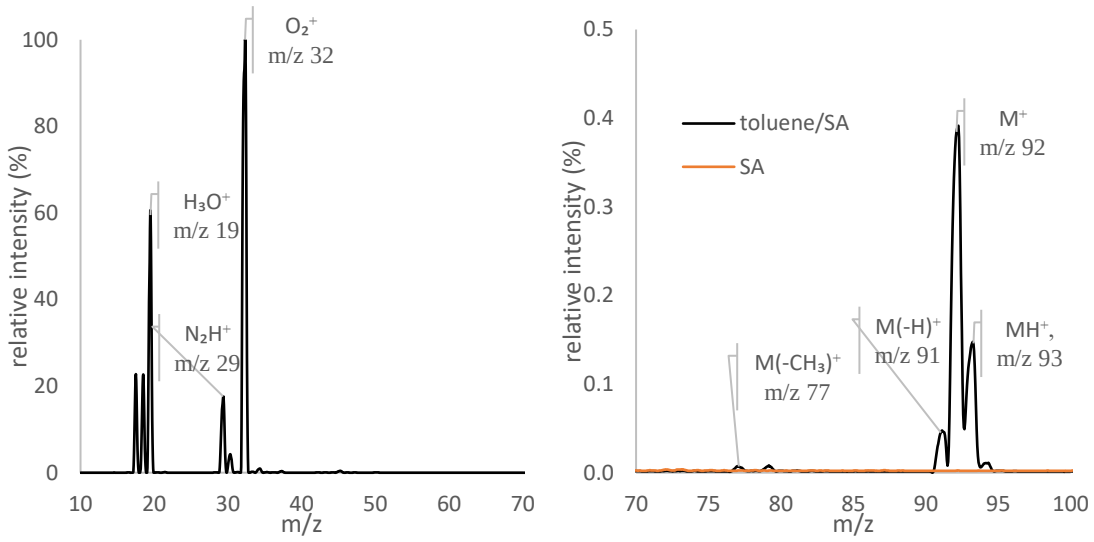


*Figure 4.29: Profile spectra of a 12.6 ppmV toluene/SA mixture introduced with a flow rate of 3.5 sccm. The 12% $N_2/H_2$ plasma gas was introduced with a flow rate of 3.0 sccm and the resulting pressure in the reaction chamber was 8.0 mbar. The m/z range 10 to 70 is shown in the left figure, and the m/z range 70 to 100 is shown in the right figure.*

$O_2^+$ is observed as the base peak in the spectrum, therefore all ion intensities were normalized to the $O_2^+$ signal with an absolute abundance of $(37 \pm 0.1) \times 10^{10}$ cps. The calculated relative abundances of the other reactant ions were $39.5 \pm 0.4\%$ for $H_3O^+$, $14.5 \pm 0.2\%$ for $N_2H^+$ and $0.1 \pm 0.01\%$ for $N_2^+$, which, in comparison, are much higher than the relative abundances of the analyte ions with < 0.5%. The absolute intensity of $MH^+$ was measured as $(6.4 \pm$

$0.3) \times 10^8$ cps for 12.6 ppmV toluene in SA. The signal intensities assigned to analyte ions have been normalized to their sum abundance ($MH^+$, $M^+$, $M(–H)^+$ and $M(–CH_3)^+$). Accordingly, for toluene, under the given ionization conditions, we found an ion signal distribution of $25 \pm 1\%$ $MH^+$, $65 \pm 2\%$ $M^+$, $9 \pm 0.3\%$ $M(–H)^+$ , and $1 \pm 0.2\%$ $M(–CH_3)^+$.

In this system, the protonated form, $MH^+$, is generated through a proton transfer reaction between a $C_7H_8$ molecule (M) and $H_3^+$, $H_3O^+$, or $N_2H^+$ reactant ions, as listed in the following:

$$C_7H_8 + H_3^+ \rightarrow C_7H_9^+ + H_2 \qquad (Rn\ 11)$$

$$C_7H_8 + H_3O^+ \rightarrow C_7H_9^+ + H_2O \qquad (Rn\ 12)$$

$$C_7H_8 + N_2H^+ \rightarrow C_7H_9^+ + N_2 \qquad (Rn\ 13)$$

For the proton-transfer process, the reaction exothermicity is defined as ΔPA = PA(toluene) – PA(reagent). The calculated ΔPA values for proton transfer from $H_3^+$, $N_2H^+$, and $H_3O^+$ to toluene are 361.7, 290.2, and 93.0 kJ $mol^{-1}$, respectively. In exothermic ion-molecule reactions, when the available excess energy (ΔPA) significantly exceeds the relevant bond dissociation energies (BDEs), the ions tend to fragment. The BDEs for $C_7H_7$–H and $C_6H_5$–$CH_3$ cleavage in toluene are approximately 356.0 and 389.0 kJ $mol^{-1}$, respectively [72,73]. Since these BDEs are greater than the ΔPA for the reaction with $N_2H^+$ and $H_3O^+$, a "soft" ionization of toluene without fragmentation is expected for these two protonation pathways. In contrast, proton transfer with $H_3^+$ (cf. *Rn 11*) induces sufficient excess energy, which makes the $C_7H_9^+$ ion prone to fragmentation. Daniel *et al.* reported that the reaction between toluene and $H_3^+$ produces $MH^+$, $M(–H)^+$, and $M(–CH_3)^+$ ions in approximate yields of 75%, 20%, and 5%, respectively, consistent with the observed fragmentation behavior [66]. The following reaction occurs with the excess energy from the reaction *Rn 11* :

$$C_7H_8 + H_3^+ \rightarrow C_7H_7^+ + 2H_2 \qquad (Rn\ 14)$$

$$\rightarrow C_6H_5^+ + H_2 + CH_4 \qquad (Rn\ 14a)$$

The fragment ions $M(–H)^+$ and $M(–CH_3)^+$ are clearly observed in the right-side spectrum in *Figure* 4.29. However, these ions may not only be produced by the reaction with $H_3^+$, additionally, charge transfer with $N_2^+$ can also lead to fragmentation of the toluene molecule [53]. Since the PG of the HPCI source is 12% $N_2/H_2$, abundant $N_2^+$ ions are present as well. As

mentioned above, the relative ion abundance of $N_2^+$ is approximately 0.1% of the base peak under the present conditions. The possible reactions between toluene and $N_2^+$ are given below:

$$C_7H_8 + N_2^+ \rightarrow C_7H_7^+ + N_2 + H \qquad (Rn\ 15)$$
$$\rightarrow C_6H_5^+ + N_2 + CH_3 \qquad (Rn\ 15a)$$

According to Anicich *et al.*, the fragmentation reactions *Rn 15* and *Rn 15*a induced by $N_2^+$ produce mainly $C_7H_7^+$ ($M(-H)^+$, 85%), along with smaller amounts of ($M(-CH_3)^+$, 5%) and further minor products [53]. However, $N_2^+$ occurs at only minor levels, and the product ion $M(-CH_3)^+$ is likewise detected at trace levels, as depicted on the right-hand of *Figure 4.29*.

Formation of the radical cation $M^+$ may also occur through charge transfer with $O_2^+$ and/or via photoionization within the reaction chamber. Literature reports indicate that charge transfer from $O_2^+$ to toluene proceeds non-dissociatively, yielding $M^+$ exclusively [74]. The ionization energy of toluene (8.83 eV) is lower than that of $O_2$ (cf. *Table 1*) making this charge-transfer pathway energetically favorable.

From a photoionization perspective, photons must possess energies ≥ 8.83 eV to ionize toluene. Because the plasma gas of the HPCI source is $H_2$, the discharge emits VUV radiation. The Lyman-series transitions of atomic hydrogen generate photons in the wavelength range 91.2–121.6 nm, corresponding to photon energies of 13.6–10.2 eV [75]. These photon energies are sufficient to ionize toluene and thereby produce $M^+$. Furthermore, following charge transfer, the molecule may fragment if the BDE of the newly formed molecular ion is lower than the excess energy. In the case of photon energy 13.6 eV, the excess energy corresponds to 4.47 eV ($13.6 - 8.83$ eV) equivalent to 460 kJ $mol^{-1}$, which exceeds the BDEs of toluene molecules. Hence, toluene can also fragment via photoionization under the present conditions, producing $M(-H)^+$ and $M(-CH_3)^+$ ions.

Based on the PG velocity of 12.1 $cm \cdot s^{-1}$, the lengths of the reaction chamber (1.0 cm) and the ID of the PS tube (0.4 cm), the reaction times for photoionization and protonation were roughly estimated to be approximately 33 ms and 82 ms, respectively. Hence, the residence time of the gas flow allows sufficient interaction for the ion–molecule reactions to proceed effectively.

The radical cation $M^+$ is also formed from reactions with $O_2^+$. Because the analyte is introduced using SA as the mixing gas, $O_2^+$ appears as the base peak in the mass spectrum (cf. *Figure*

*4.29*). It is therefore reasonable to expect that substituting the mixing gas, for example, replacing SA with high-purity $N_2$, could alter the dominant ionization pathways and the resulting ion populations. To evaluate this effect, an additional experiment using a toluene/$N_2$ mixture (12.6 ppmV) was investigated and is shown in the following.

*Toluene/$N_2$ measurement*

A 12.6 ppmV toluene/$N_2$ mixture as the analyte gas was investigated and the results are shown in *Figure 4.30*. The base peak is assigned to $N_2H^+$, with an absolute abundance of $(14 \pm 0.3) \times 10^{10}$ cps. Further reactant ions and their abundances relative to the base peak are $NH_4^+$ with $69 \pm 1\%$, $H_3O^+$ with $16 \pm 0.3\%$, $O_2^+$ with $1.5 \pm 0.1\%$ and $N_2^+$ with $0.3 \pm 0.01\%$.

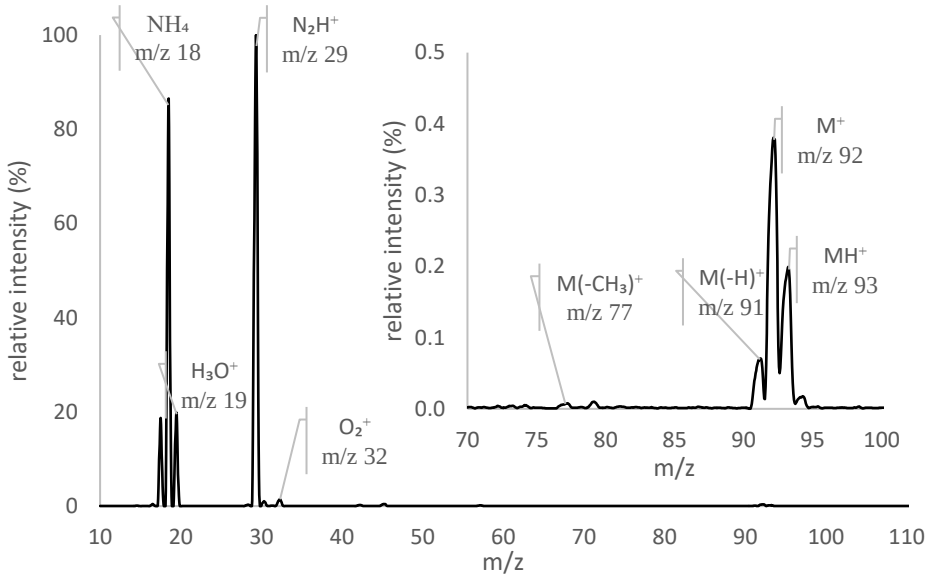


*Figure 4.30: Mass spectrum from a 12.6 ppmV toluene/$N_2$ mixture as the sample gas and a 12% $N_2/H_2$ plasma gas supply with flow rates of 3.5 sccm and 3.0 sccm, respectively. The resulting pressure was 8 mbar. The analyte ions are shown in the m/z range 70 to 100.*

Striking is the strong intensity at m/z 18, corresponding to $NH_4^+$. As discussed in *section 4.1.1.1* at elevated pressure $NH_3$ might be heterogeneously formed from plasma species at the wall surfaces either in the plasma glass tube or even in the reaction chamber. Ammonia is then subsequently protonated by $H_3^+$, $N_2H^+$ or $H_3O^+$ to form $NH_4^+$. Interestingly, however, that simply the change of the sample gas composition from synthetic air with 78.5% $N_2$, 20.5% $O_2$ and 12.6 ppmV toluene, to pure $N_2$ with 12.6 ppmV toluene (cf. *Figure 4.30*) has such a drastic

effect on the formation rate of $NH_4^+$. Since the composition and flow through the plasma glass tube is assumed to have remained constant and only the composition in the reaction chamber had changed, it might be speculated that the main region of $NH_3$ formation is indeed preferably on the metal walls of the reaction chamber. The acidity of $NH_4^+$ is not strong enough to directly protonate toluene, however, slight differences compared to the previous experiment with the toluene/SA as the sample gas can be found. The absolute ion abundance of the protonated analyte $MH^+$ is $(4 \pm 0.2) \times 10^8$ cps, which is approximately 37% lower than that measured for the toluene/SA sample. Furthermore, the recorded ion distribution of $31 \pm 1\%$ $MH^+$, $56 \pm 2\%$ $M^+$, $12 \pm 0.5\%$ $M(–H)^+$, and $1 \pm 0.3\%$ $M(–CH_3)^+$ slightly deviates from the previous experiment as well.

As discussed earlier, the protonated form $MH^+$ is produced via proton transfer from three reagent ions—$H_3^+$, $H_3O^+$, and $N_2H^+$. Since $H_3^+$ is the primary ion generated in the HPCI source, its concentration is expected to be similar in both systems (toluene/$N_2$ and toluene/SA). The remaining two reagent ions, $H_3O^+$ and $N_2H^+$, are clearly observed in the profile spectrum (cf. *Figure 4.29)*, and their concentrations are higher in the SA-based experiment. In contrast, when $N_2$ is used as the mixing gas, the corresponding profile spectrum shows $N_2H^+$ as the base peak, whereas $H_3O^+$ appears at significantly lower relative intensity (cf. *Figure 4.30*). However, the higher abundance of $H_3O^+$ in the SA mixture originates from residual moisture impurities in the synthetic air. Since the rate coefficients for proton transfer from $H_3O^+$ and $N_2H^+$ to toluene (*Rn 12 and Rn 13*) are similar (cf. *Table 3*), and both experiments use identical analyte concentrations (12.6 ppmV), the differing yields of $MH^+$ can be assumed to only depend on the concentration of the reactants. In the toluene/$N_2$ experiment, the combined abundance of these two reagent ions is approximately 20% lower than in the toluene/SA experiment. As a result, the $MH^+$ intensity in the toluene/$N_2$ system is reduced accordingly. However, the relative $MH^+$ abundance (related to the sum of observed analyte ions) of the toluene/$N_2$ sample increases by 6% in comparison to the toluene/SA sample.

In this experiment, the abundance of the molecular ion $M^+$ ($(7.4 \pm 0.3) \times 10^8$ cps) is approximately 56% lower as compared to the toluene/SA sample. As discussed previously, $M^+$ is produced primarily through charge transfer from $O_2^+$ and via photoionization. Since the photon flux from the plasma in both experiments is assumed to be identical, the difference in $M^+$ formation can be attributed to the strong decrease in the $O_2^+$ concentration. The $O_2^+$

abundance is significantly higher in the toluene/SA mixture, because oxygen is actively added with 20.5% of the sample gas. Consequently, the toluene/SA sample yields a proportionally higher $M^+$ signal. This indicates that the absolute $M^+$ intensity depends on the availability of $O_2^+$. Nevertheless, the relative $M^+$ signal (related to the sum of observed analyte ions) for the toluene/$N_2$ sample was reduced by only about 10% relative to the toluene/synthetic-air condition, highlighting the superior mechanism of photoionization for producing the radical cation in this system.

*O-xylene/$N_2$ measurement*

In this experiment, the analyte (M) was introduced into the reaction chamber as a 4.1 ppmV o-xylene ($C_8H_{10}$) in nitrogen mixture. To assess background signals, an additional experiment was conducted under otherwise identical conditions using only $N_2$ as the sample gas. The nominal sample flow rate was 4.0 sccm, and 10% $N_2/H_2$ plasma gas with flow rate was 3.0 sccm. However, due to an improper seal between the plasma glass tube and the reaction chamber (see *Section 4.1.2*), the plasma source pressure was only approximately 1.7 mbar. Consequently, the results are not directly comparable to the two preceding experiments with toluene.

The reactant ion distribution in the mass range of m/z 15-65 is shown in the upper graph of *Figure 4.31* and is essentially the same for the blank and the analyte spectrum. The lower graph (blue) shows the assigned analyte ions $MH^+$, $M^+$, $M(-H)^+$ and $M(-CH_3)^+$. The orange line shows the blank spectrum in that mass range. The y-axis of both figures represents the relative intensity with respect to the $N_2H^+$ abundance.

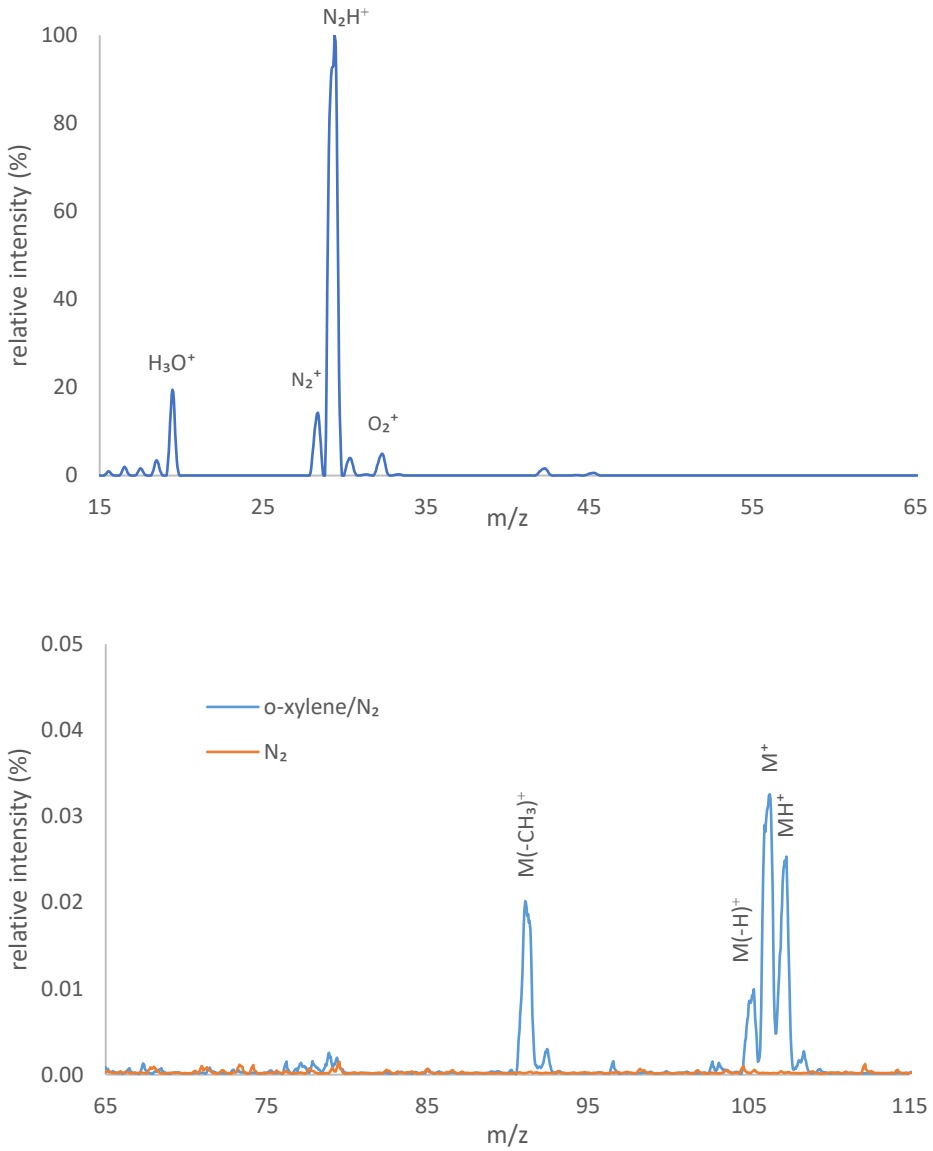


*Figure 4.31: Mass spectrum of a 4.1 ppmV o-xylene/$N_2$ mixture (blue) and a blank spectrum with only $N_2$ gas (orange, lower figure) at a total pressure of 1.7 mbar in the reaction chamber. Sample and PG (10% $N_2$/$H_2$) flow rates were 4.0 and 3.0 sccm, respectively.*

The ions $H_3O^+$, $N_2^+$, $N_2H^+$, and $O_2^+$ are clearly observed in the upper figure. Among these ions, the $N_2H^+$ is the base peak and its absolute intensity is $(39 \pm 0.1) \times 10^{10}$ cps. The relative intensities of $H_3O^+$, $N_2^+$, and $O_2^+$ with respect to $N_2H^+$ are $11 \pm 0.3\%$, $13 \pm 0.2\%$ and $4 \pm 0.2\%$, respectively.

The signal intensities assigned to the individual analyte species are normalized based on the sum of all observed o-xylene ions. For $MH^+$, $M^+$, $M(-H)^+$ and $M(-CH_3)^+$ these recorded relative

intensities are $28 \pm 5\%$, $38 \pm 6\%$, $10 \pm 2\%$, and $24 \pm 3\%$, respectively. The absolute intensity of the protonated o-xylene form ($MH^+$) is $(1 \pm 0.2) \times 10^8$ cps.

All the reactant ions can react with $C_8H_{10}$ molecules due to the lower PA and higher ionization energy than that of the analyte molecule (cf. *Table* 1). The corresponding reaction rate constants are listed in *Table 3*. The $H_3^+$, $N_2H^+$ and $H_3O^+$ ions can transfer a proton (*Rn 1*) to the M and produce $MH^+$ ion at m/z 107 and $H_2$, $N_2$ and $H_2O$, respectively. The excess energies (ΔPA) of these reactions are 373.7, 302.2, and 105.0 kJ $mol^{-1}$, respectively. Literature reported that the BDE of $C_8H_9$-H and $C_7H_7$-$CH_3$ are 357.3 and 301.0 kJ $mol^{-1}$ [73,76]. Therefore, the reaction between the $H_3^+$ ion and o-xylene can also fragment the ion due to the available excess energy. Moreover, the ionization energy of o-xylene with 8.56 eV (cf. *Table 1*) is significantly lower than the available photon energies of the hydrogen plasma. Consequently, also fragmentation due to photoionization can occur, as was observed for toluene.

As discussed for the toluene measurement, the $M^+$ cannot only be formed via photoionization. In addition, the reactant ions $N_2^+$ and $O_2^+$ can ionize o-xylene via charge-transfer reactions, generating the molecular ion, which is subsequently prone to fragmentation due to available excess energy (cf. *Table 1*). According to literature values, the reaction between neutral $C_8H_{10}$ and $N_2^+$ produces $C_8H_{10}^+$ (4%), $C_8H_9^+$(8%), $C_7H_7^+$(79%), and $C_6H_6^+$(9%). In contrast, the reaction between $C_8H_{10}$ and $O_2^+$ produces $C_8H_{10}^+$, $C_7H_7^+$, and $C_6H_6^+$ ions, with relative abundances of 30%, 67% and 3 % respectively [53]. The corresponding reactions are shown in the following:

| | | | | | | | | | |
|---|---|---|---|---|---|---|---|---|---|
| $C_8H_{10}$ | + | $N_2^+$ | → | $C_8H_{10}^+$ | + | $N_2$ | | | (*Rn 16*) |
| | | | → | $C_8H_9^+$ | + | $N_2$ | + | H | (*Rn 16a*) |
| | | | → | $C_7H_7^+$ | + | $N_2$ | + | $CH_3$ | (*Rn 16b*) |
| | | | → | $C_6H_6^+$ | + | $N_2$ | + | $C_2H_4$ | (*Rn 16c*) |
| $C_8H_{10}$ | + | $O_2^+$ | → | $C_8H_{10}^+$ | + | $O_2$ | | | (*Rn 17*) |
| | | | | $C_7H_7^+$ | + | $O_2$ | + | $CH_3$ | (*Rn 17a*) |
| | | | | $C_6H_6^+$ | + | $O_2$ | + | $C_2H_4$ | (*Rn 17b*) |

The profile spectrum of the analyte ions shows that the fragment ion $M(-CH_3)^+$ is produced in higher abundance than the $M(-H)^+$ ion. In comparison, the fragmentation pattern of toluene differs from that of *o*-xylene, which can be attributed to the lower formation of $N_2^+$ ions under the same mixing gas conditions (cf. *Figure 4.30*). It is expected that with changing $N_2^+/O_2^+$ ratio also the overall mean available excess energy changes.

*Analysis of BTX/synthetic air*

In the previous experiments of this section, two aromatic compounds were introduced into the system. It was observed that different reactant ions react with the $C_7H_8$ and $C_8H_{10}$ molecules and produce $MH^+$, $M^+$, $M(-H)^+$ , and $M(-CH_3)^+$. However, in this experiment, a BTX/SA mixture (benzene, toluene, and o-xylene are 10.6, 9.9, and 9.6 ppmV, respectively) was introduced, and these analytes were observed under different reaction chamber pressure conditions. This pressure was controlled by varying the sample gas flow, while the plasma gas $N_2/H_2$ mixing was kept constant at a flow rate of 3.0 sccm.

The maximum yield of reactant ions was observed at a total gas flow rate of 6.5 ± 0.5 sccm, corresponding to a pressure of 8.0 ± 1.0 mbar, with $N_2H^+$ exhibiting the highest ion population (cf. *section 4.1.4*). Here, the BTX/SA mixture is introduced into the reaction chamber, and the pressure is adjusted within the range of 3.5 mbar to 15.5 mbar by varying the sample flow.

Two profile spectra of the BTX/SA mixture under two different pressure conditions (3.5 mbar and 8.0 mbar) are shown in *Figure 4.32*. The upper and lower figures show reactant ions and analyte ions, respectively, and are normalized to the $N_2H^+$ ion abundance. The base peak is the $N_2H^+$ ion, which is shown in both spectra in the upper figure. The relative abundances of the other reactant ions significantly change with pressure and gas flow. The $N_2^+$ population decreased, whereas $H_3O^+$ and $O_2^+$ increased with pressure. The dependence of reactant ions on the sample flow with constant PG flow has been discussed in Section *4.3* in more detail.

The observed analyte ions are $MH^+$, $M^+$, $M(-H)^+$ and $M(-CH_3)^+$ and are shown in the lower graph of *Figure 4.32*). The maximum intensity of protonated molecules for benzene ($M_bH^+$), toluene ($M_tH^+$), and o-xylene ($M_xH^+$) is observed at 8.0 mbar pressure in this experiment, which can be attributed to the highest abundance of reactant ions generated at this pressure. This pressure was achieved by adding 6.5 sccm of total gas flow (3.0 sccm PG and 3.5 sccm analyte).

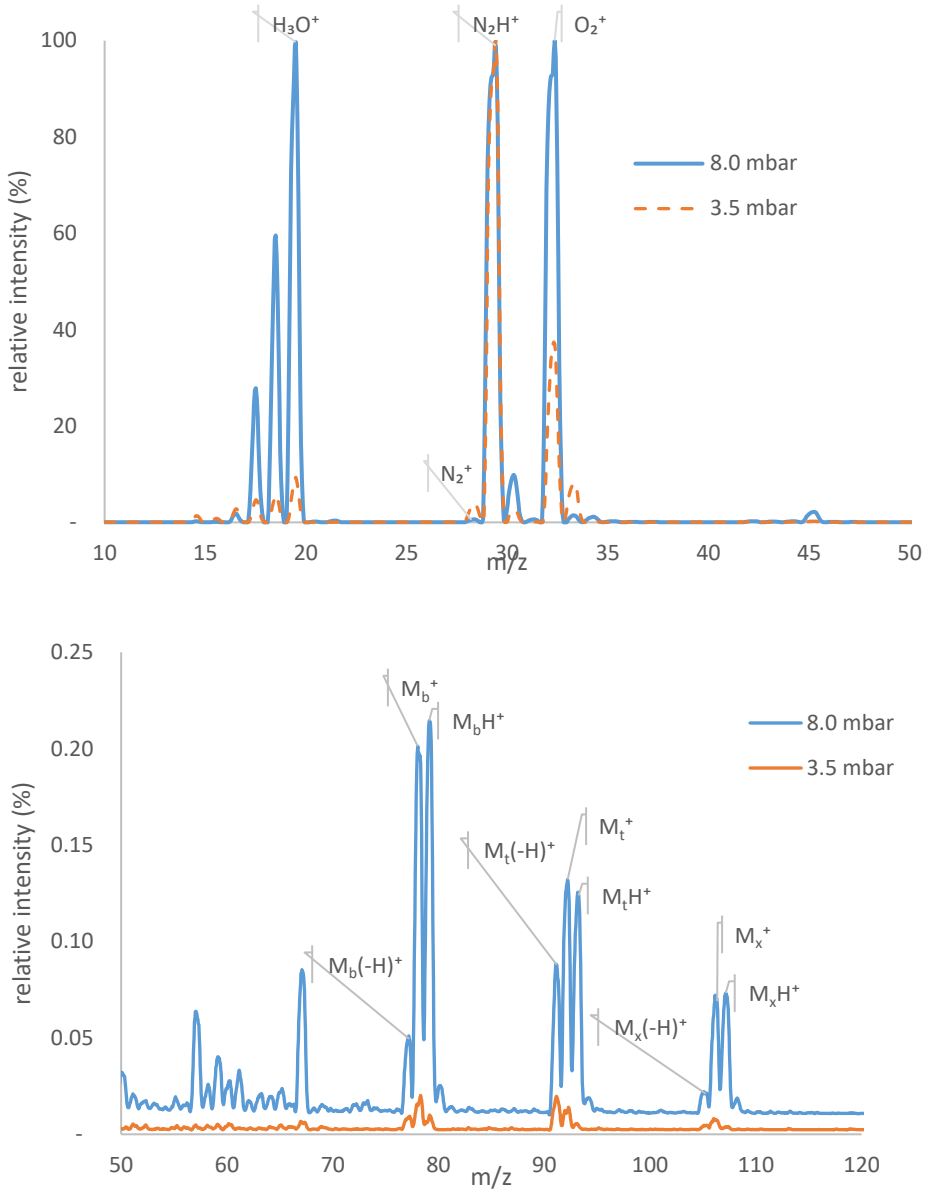


*Figure 4.32: Profile spectra of a BTX/SA mixture with flow rates of 1.0 sccm and 3.5 sccm, corresponding to 3.5 mbar and 8.0 mbar pressure with a constant plasma gas (12% $N_2/H_2$) flow rate of 3.0 sccm. The upper figure shows the reactant ion distribution in the m/z range 10 to 70, while the lower figure shows the molecular ions in the m/z range 70 to 120.*

The formation of analyte ions of toluene and o-xylene with the same reactants ($H_3^+$, $H_3O^+$, $N_2^+$, $N_2H^+$, and $O_2^+$) has been discussed in the previous experiment. Therefore, this experiment focuses on the benzene ion formation only. Since the PA of benzene is greater than that of all of the protonating reactants, the $MH^+$ is formed through proton transfer from $H_3^+$, $H_3O^+$, as well

as $N_2H^+$ (cf. *Rn 1*). Again, the surplus energy should be taken into account to estimate fragmentation tendencies. The ΔPA values of these reagents with benzene are 328.1, 256.6, and 59.4 kJ $mol^{-1}$, respectively. Since these energies are less than the BDE of benzene, these reactions are non-dissociative reactions and form only the $MH^+$ ion.

The radical ion of benzene is also formed through photoionization in the same way as for toluene and o-xylene, which have been discussed in the previous experiment. In addition, the other two reactant ions, $N_2^+$ and $O_2^+$, can generate $M^+$ through charge transfer. The $N_2^+$ reactant tends to induce fragmentation $M(-H)^+$ due to its higher ionization energy (cf. *Rn 18a*). The literature reports that the $M^+$ and $M(-H)^+$ species for benzene are 12% and 24%, respectively, when it reacts with the $N_2^+$ ion [53].

$$C_6H_6 + N_2^+ \rightarrow C_6H_6^+ + N_2 \quad (Rn\ 18)$$

$$\rightarrow C_6H_5^+ + N_2 + H \quad (Rn\ 18a)$$

$$C_6H_6 + O_2^+ \rightarrow C_6H_6^+ + O_2 \quad (Rn\ 19)$$

It was also observed that toluene and o-xylene formed $M(-CH_3)^+$ at m/z 77 and 91. Therefore, in this BTX mixture, these $M(-CH_3)^+$ add to the benzene and toluene signals at these specific m/z values. The reaction between toluene and $H_3^+$ preferably forms a fragmented molecular ion by loss of an H-atom and yields the $C_7H_7^+$ ion. Furthermore, toluene produces about 85% of the $C_7H_7^+$ ion when it reacts with the $N_2^+$ ion [53]. On the other hand, benzene loses only the H-atom when it reacts with $N_2^+$. Therefore, the profile spectrum shows the benzene intensity is the highest as compared to toluene and o-xylene. In the benzene measurement at 8.0 mbar pressure, the relative analyte ion intensities for $MH^+$, $M^+$ and $M(-H)^+$ are 44 ± 2%, 45 ± 2% and 11 ±1%, respectively.

The applied total gas flow produces the maximum reactant ion yield ($H_3O^+$ and $N_2H^+$). Beyond the 3.5 sccm analyte flow, the $MH^+$ starts decreasing due to the decrease in the total reactant ion population (cf. *Section 4.3 Figure 4.25*).

The results show that the $M^+$ fraction increases with increasing pressure, primarily due to the higher analyte flow introduced into the reaction chamber (cf. *Section 4.3 Figure 4.25*). In contrast, the $MH^+$ fraction increases up to 8.0 mbar but subsequently decreases, which can be attributed to the reduction in reactant-ion densities at higher pressures. Additionally, the fragment-ion ($M(-H)^+$) abundances decrease with increasing pressure because the formation of $N_2^+$, the primary contributor to fragmentation, is reduced under higher-pressure conditions.

The pressure-dependent formation of analyte ions (%) is presented in *Figure 4.33*. The branching ratios, calculated from the relative abundances of $MH^+$, $M^+$, and $M(-H)^+$ for benzene, toluene and o-xylene. However, the branching ratio of toluene ions (for instance) is plotted on the y-axis. The x-axis represents the reaction chamber pressure, which was varied by adjusting the sample flow rate of the BTX/SA mixture, while maintaining a constant PG flow rate of 3.0 sccm.

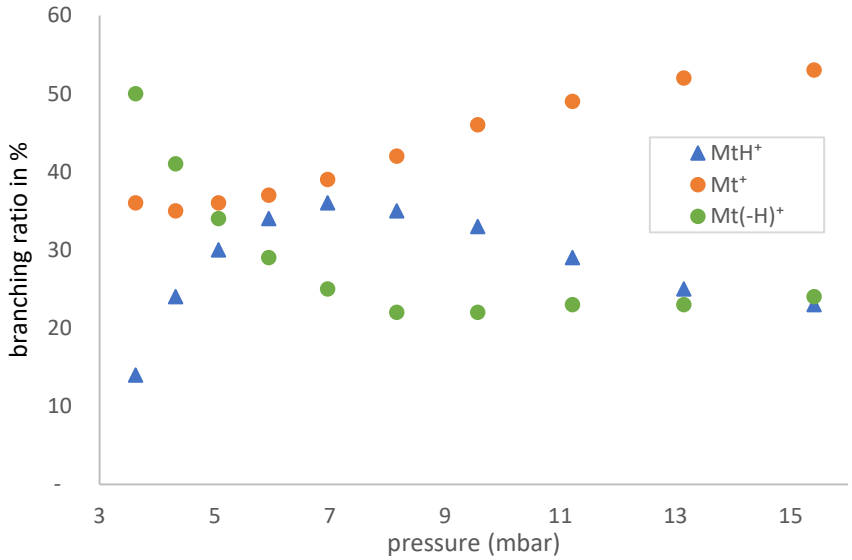


*Figure 4.33: Dependence of the branching ratio of toluene analyte ions on the reaction chamber pressure. The pressure was varied by adjusting the sample flow rate.*

The abundance of protonated toluene increases with increasing pressure up to approximately 7.0 ± 1.0 mbar and beyond this, decreases. In contrast, the abundance of the $M^+$ ion increases continuously with pressure. At lower reaction chamber pressures, corresponding to lower analyte flow, protonation efficiency is reduced, resulting in a relatively higher $M^+$ branching ratio under these conditions. The branching ratio of the observed fragment ion, $M(-H)^+$, decreases with increasing pressure up to approximately 7.0 ± 1.0 mbar, after which it remains relatively constant. The same trend for analyte ions was likewise observed for benzene and o-xylene.

At a chamber pressure of 7.0 ± 1.0 mbar, the $MH^+/M^+$ ratios range between 0.9 and 1.1 for benzene, toluene, and o-xylene. At the lower and upper limits of the investigated pressure range (3.5 mbar and 15.5 mbar, respectively), the $MH^+/M^+$ ratios are 0.45 and 0.65.

Aromatic compounds analyzed with the HPCI–MS system undergo proton transfer reactions with primary reactant ions, such as $H_3^+$, $N_2H^+$, and $H_3O^+$. In addition to these protonation processes, other ionic species - including $N_2^+$ and $O_2^+$ - along with photoionization effects contribute to the overall ionization, yielding molecular ions ($M^+$) and various fragment ions. Ionization and fragmentation caused by VUV radiation from the plasma can be mitigated by increasing the distance between the plasma and the helical resonator; however, this also markedly reduces the population of protonated molecular ions (cf. *Figure 4.22*). Due to the design of the current plasma source, the VUV emission from the plasma directly enters the reaction chamber and ionizes molecules, complicating the distinction between photon-induced effects and those caused by the reactants. To address this issue, two alternative plasma-source designs are described and discussed in section *4.11*.

### 4.7.2 Measurement of Oxygenated Compounds using $N_2/H_2$ Reagent Gas

In the previous experiments, aromatic compounds such as benzene, toluene and o-xylene were investigated in ionization processes with the HPCI source operated with a 12% $N_2/H_2$ plasma gas supply. In the following, oxygenated compounds (methanol, ethanol, iso-propanol and n-butanol) are investigated. The corresponding reaction rate constants with the reactant ions are listed in *Table 3*.

*Methanol/synthetic air measurement*

A methanol/SA mixture at 7 ppmV was introduced into the reaction chamber at a sample flow rate of 3.0 sccm. The plasma was operated with a 3.5 sccm flow of a plasma gas consisting of 12% $N_2$ in $H_2$. The recorded reactant ions are depicted in the upper panel of *Figure 4.34*. In addition, a blank spectrum was recorded under identical conditions, using SA as the sample gas instead of the methanol-containing mixture. The spectra with and without the analyte are marked by a blue line and an orange dotted line, respectively. As in the previous experiments in which synthetic air was the main component of the sample gas, the $O_2^+$ ion at m/z 32 remains the base peak in both spectra. $N_2H^+$ and $H_3O^+$ are present with relative intensities of 40% and 54%, respectively.

The reactions (*Rn 21* and *Rn 22*) of methanol with $N_2H^+$ and $H_3O^+$ proceed through a proton transfer reaction with methanol ($CH_3OH$, M) and should yield $CH_3OH_2^+$ ($MH^+$) at m/z 33, which is shown in the profile spectrum (lower *Figure 4.34*) (y-axis zooming). The relative ion (related to base peak) abundance of $MH^+$ at m/z 33 yielded 0.2%, however, no difference was observed compared to the blank spectrum. With $H_3^+$ (primary ion) and $N_2H^+$ the molecular ion can also fragment into $M(-H)^+$ and $M(-OH)^+$, corresponding to masses at m/z 31 and 15. However, also at these masses no difference between the analyte and the blank spectrum was observed.

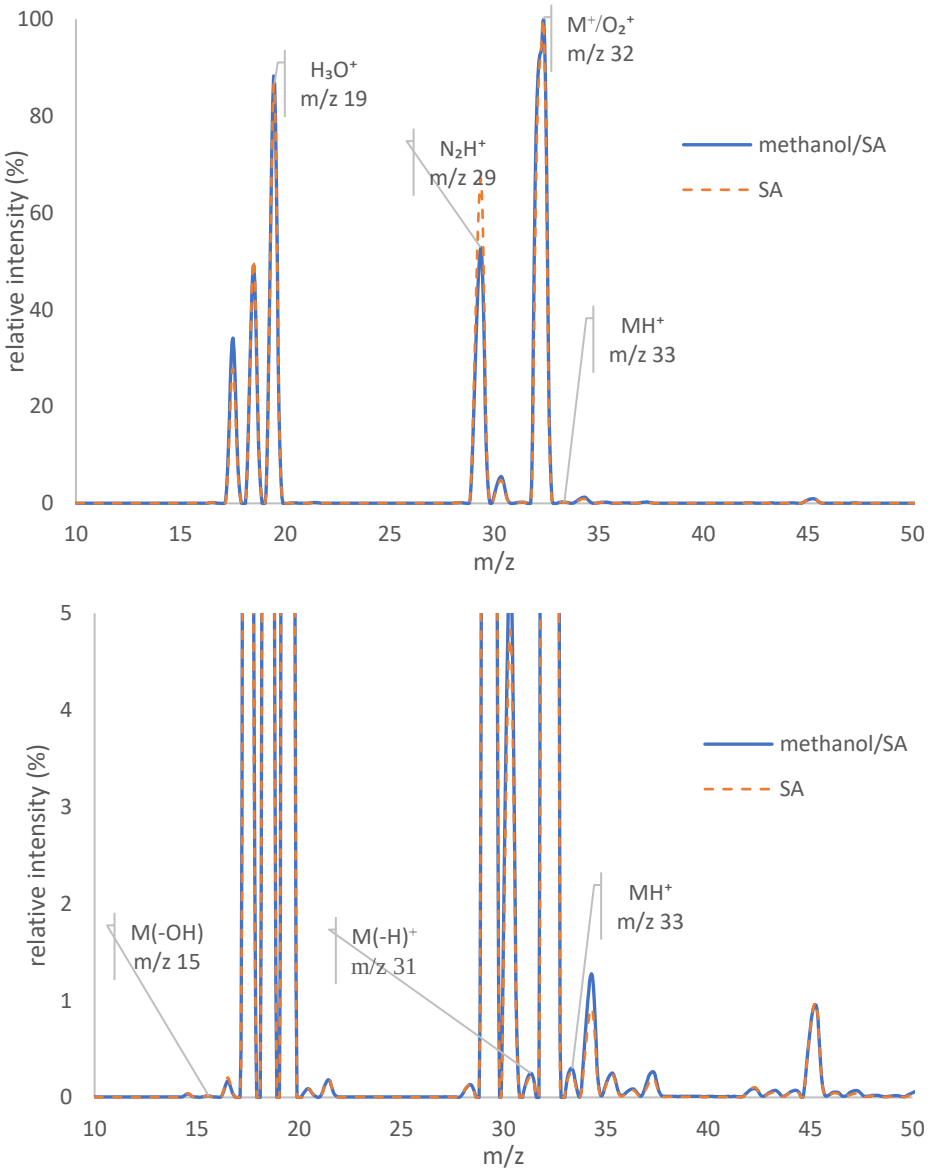


*Figure 4.34: Profile spectra of methanol and synthetic air (upper) using 12% $N_2/H_2$ reagent gas. The lower figure shows a zoom-in on the expected analyte ions.*

The possible reactions of reactants $H_3^+$ (primary reactant), $N_2H^+$, and $H_3O^+$ and the methanol are shown below.

$$CH_3OH + H_3^+ \rightarrow CH_3OH_2^+ + H_2 \quad \textit{(Rn 20)}$$
$$\rightarrow CH_2OH^+ + 2H_2 \quad \textit{(Rn 20a)}$$
$$\rightarrow CH_3^+ + H_2O + H_2 \quad \textit{(Rn 20b)}$$
$$CH_3OH + H_3O^+ \rightarrow CH_3OH_2^+ + H_2O \quad \textit{(Rn 21)}$$
$$CH_3OH + N_2H^+ \rightarrow CH_3OH_2^+ + N_2 \quad \textit{(Rn 22)}$$
$$\rightarrow CH_2OH^+ + N_2 + H_2 \quad \textit{(Rn 22a)}$$
$$\rightarrow CH_3^+ + H_2O + N_2 \quad \textit{(Rn 22b)}$$

According to literature, the reactant ion $H_3^+$ reacts with methanol (*Rn 20, Rn 20a and Rn 20b)*) and produces $CH_3OH_2^+$, $CH_2OH^+$ and $CH_3^+$ with a distribution of 12%, 28% and 53%, respectively [77]. $N_2H^+$ also generates $CH_3OH_2^+$, $CH_2OH^+$ and $CH_3^+$ ions (reaction *Rn 22, Rn 22a, and Rn 22b*) with a distribution of 82%, 7% and 11%, respectively [78].

$O_2^+$ can also react with neutral $CH_3OH^+$ according to.

$$CH_3OH + O_2^+ \rightarrow CH_3OH^+ + O_2 \quad \textit{(Rn 23)}$$
$$\rightarrow CH_2OH^+ + HO_2 \quad \textit{(Rn 23a)}$$

The reactions *Rn 23* and *Rn 23a* proceed with a ratio of 50% as investigated by Patrik *et al*. [68]. The $M^+$ and M(-H) ions should be observed at m/z 32 and 31, respectively. However, the limited mass resolution of the analyzer does not allow to separate $CH_3OH^+$ (32.02622 Da) from the $O_2^+$ (31.98984 Da) base peak with a $\Delta$m/z of 36 mDa.

In conclusion, a 7 ppmV methanol-containing mixture in synthetic air could not be analyzed with the HPCI source operated with 12% $N_2$ in $H_2$. Neither the molecular ion, the quasi-molecular ion, nor fragments or clusters (such as $(CH_3OH)_2H^+$) were observed, partly due to overlapping signals from the reactant ions.

*Ethanol/synthetic air measurement*

Another alcohol, ethanol (M), at a mixing ratio of 2.6 ppmV in SA, is also investigated using the same reagent $N_2/H_2$ mixing gas as the previous experiment (methanol measurement). Therefore, the same reactants may also react with ethanol ($C_2H_5OH$). The profile spectra of ethanol and SA are shown in *Figure 4.35*.

The ethanol molecule with m/z 46 can accept a proton from $H_3^+$, $H_3O^+$, and $N_2H^+$ and form the protonated molecule $MH^+$ at m/z 47. According to the literature, the $MH^+$ can be formed when ethanol reacts with the $H_3O^+$ and $N_2H^+$ [53,70]. However, similarly to the methanol sample, the background at the mass for the quasi-molecular ion seems to be too high, therefore no difference in the blank and the sample spectra were found. The reaction with $H_3^+$ can additionally fragment the ethanol molecule and form up to 10% $M(-H)^+$ and 44% $M(-OH)^+$ at m/z 45 and 29, respectively [77]. However, these ions also possess identical m/z ratios as $CO_2H^+$ (m/z 45) and $N_2H^+$ (m/z 29), respectively. Consequently, also the ions $M(-H)^+$ and $M(-OH)^+$ were not detectable.

$$C_2H_5OH + H_3^+ \rightarrow C_2H_5O^+ + 2H_2 \qquad \textit{(Rn 24)}$$

$$\rightarrow C_2H_5^+ + H_2O + H_2 \qquad \textit{(Rn 24a)}$$

The reaction with $O_2^+$ can proceed via simple charge transfer or fragmentation to produce $M^+$ (25%) and $M(-H)^+$ (75%) as follows [68], again undetectable due to the overlapping background signals.

$$C_2H_5OH + O_2^+ \rightarrow C_2H_5OH^+ + O_2 \qquad \text{(Rn 25)}$$

$$\rightarrow C_2H_5O^+ + O_2 + H \qquad \textit{(Rn 25a)}$$

Just as in the methanol experiment, clusters were not observed either under the present conditions.

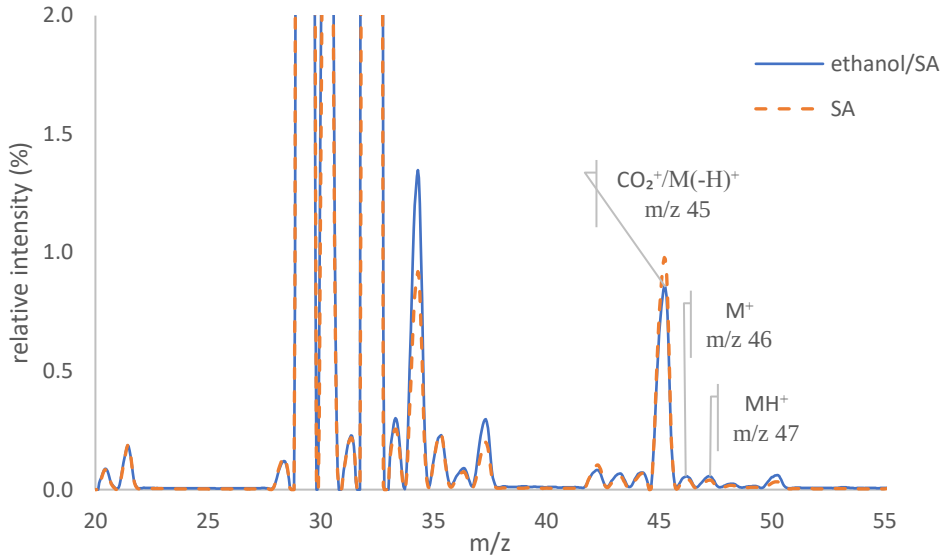


*Figure 4.35: Profile spectrum of a 2.6 ppmV ethanol in synthetic air (SA) sample (blue line) and a blank spectrum with SA (orange dotted). The 12% $N_2/H_2$ PG was used to generate the reactant ions.*

In conclusion, also ethanol could not be analyzed under the employed HPCI operating conditions.

*Iso-propanol/synthetic air measurement*

A 1.4 ppmV iso-propanol ($C_3H_7OH$, M) mixture in SA was investigated as well. Again, the sample flow was set to 3.0 sccm and the plasma gas flow from a 12 % $N_2/H_2$ mixture remained constant at 3.5 sccm. The recorded profile spectrum together with a blank spectrum from synthetic air as the sample are shown in *Figure 4.36*.

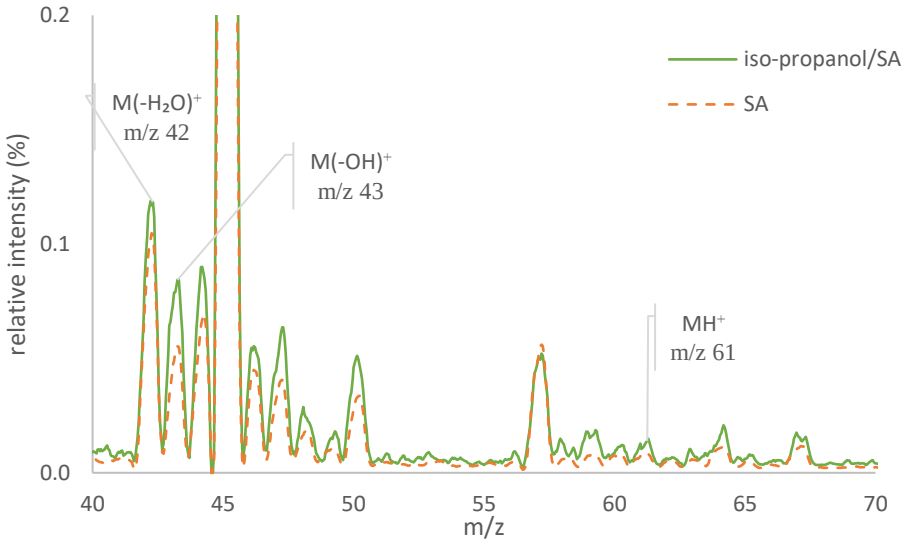


*Figure 4.36: 1.4 ppmV iso-propanol in synthetic air (SA) as the sample gas (green line) and a blank spectrum with SA (orange dotted line) using 12% $N_2/H_2$ reagent gas.*

The protonated propanol ($MH^+$) is expected at m/z 61, when the neutral reacts with $H_3^+$, $H_3O^+$ or $N_2H^+$. However, also in this case the quasi-molecular ion is virtually absent, when comparing the analyte spectrum to the blank spectrum. In literature, yields of 10% for the $MH^+$ and 90% for the fragment $M(-OH)^+$ are reported for the reaction with $H_3O^+$ ions [68]. Indeed, comparing the analyte spectrum and the blank spectrum at the corresponding m/z 43 for the latter fragment, a slight increase is observed, however, not sensitive enough for an analytical system. Additionally, a smaller increase in signal intensity is recognized for the fragment at m/z 42, which corresponds to the loss of a water molecule, a typical fragmentation pathway for the alcohol group. This is, e.g., described by the reaction with $O_2^+$:

$$C_3H_7OH + O_2^+ \rightarrow C_3H_6^+ + O_2 + H_2O \qquad (Rn\ 26)$$

$$CH_3O^+ + O_2 + C_2H_5 \qquad (Rn\ 26a)$$

The reported branching ratio between these reactions is 1/9 [68].

Neither the lower mass range nor the higher mass range showed signals indicative of fragments or clusters for iso-propanol, which could be used for proper identification. Consequently, the current operating conditions of the HPCI source are not suitable for isopropanol analysis either.

*n-butanol/synthetic air measurement*

In the last experiment of this series, n-butanol ($C_4H_9OH$, M) has been introduced as a 14 ppmV mixture in synthetic air for analysis. The flow conditions were slightly changed to 4.0 sccm sample gas and 2.0 sccm plasma gas. Again, a blank spectrum with synthetic air as the sample gas has been recorded as well to easier identify changes in the signal pattern. Both spectra are depicted in *Figure 4.37.*

In this experiment changes at masses corresponding to the $MH^+$, $M^+$, $M(-H_2O)^+$ and $M(-H_2)^+$ of n-butanol were identified. The $M(-OH)^+$ fragment at m/z 57 might be present but overlaps with a background signal in the blank spectrum.

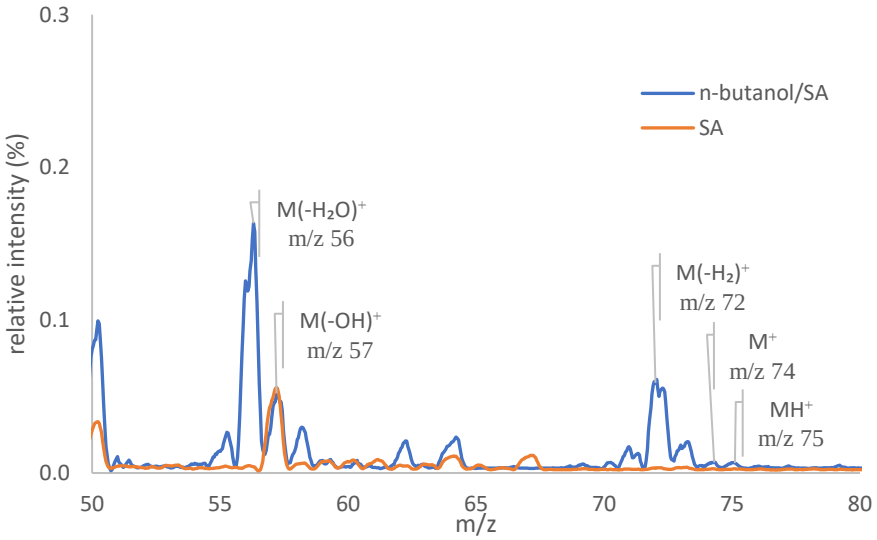


*Figure 4.37: Profile spectra of n-butanol/SA and only synthetic air (SA) using $N_2/H_2$ reactant gas.*

The fragment due to water loss $M(–H_2O)^+$ at m/z 56 showed the highest relative intensity with approximately 67 % relative to the sum of all analyte ion signals. In literature, a yield of 80% for this fragment has been reported for the reaction between $O_2^+$ and n-butanol [68]. Moreover,

the molecular ion ($M^+$) and the protonated form ($MH^+$) were observed with intensities of 4 % and 3%, respectively.

In summary, the alcohol measurements show that the HPCI source with 12% $N_2$ in $H_2$ does not meet the analytical requirements for a practical application. Analyte signals were either masked by background or undetectable, with only isopropanol and n-butanol giving any response, which still remained inadequate. In the next step, the type of reagent ions was altered by adding the saturation vapor from liquid methanol to the reaction chamber. This so called “dopant” was introduced to further improve analyte ion yields.

### 4.7.3 Measurement of Analytes Using Methanol as Dopant

A molecule with a higher proton affinity (PA) can be protonated by another molecule with a lower PA. This property makes methanol particularly suitable for promoting proton transfer reactions under relatively soft ionization conditions (cf. *PA list in Table 1*), and it is therefore frequently used as a reactant in CI techniques [79,80]. In the 7 ppmV of methanol/synthetic air experiment described in *section 4.7.2*, a signal intensity of only 0.2% of protonated methanol ($CH_3OH_2^+$) at m/z 33 relative to the base peak was observed, which is insufficient to provide analytically relevant amounts of reactant ions. Consequently, higher methanol mixing ratios in the percent range are employed in the following and are used as reactant ions.

Based on the reaction *Rn 20*, $H_2$ was introduced into the HPCI source as the plasma gas at a flow rate of 3.0 sccm to generate $H_3^+$ as the primary ion. Further, a synthetic air flow, saturated with up to 12% methanol vapor using a temperature-controlled liquid methanol setup, was introduced through the sample line, as shown in *Figure 3.5*.

Since the maximum sample flow rate 4.0 sccm can be added to the reaction chamber, the methanol mixing ratio was adjusted by varying the flow of SA before entering the reaction chamber. A profile spectrum of 1 % methanol/SA is shown in the upper graph in *Figure 4.38*. The methanol/SA mixing ratio is increased to 3% by adding 1.0 sccm of SA flow into the liquid methanol and the recorded profile spectrum is shown in the lower in *Figure 4.38*.

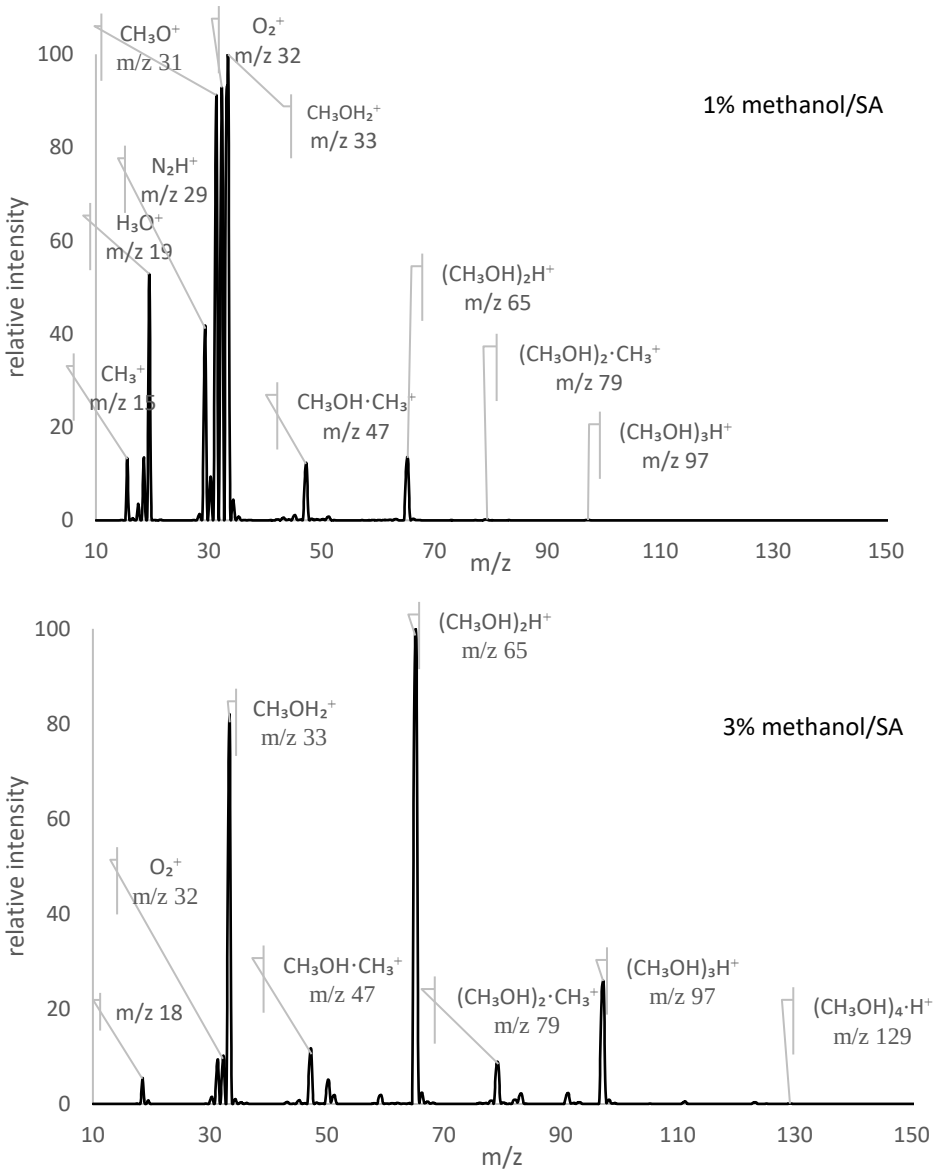


*Figure 4.38: Profile spectra of methanol in SA mixtures. The upper figure illustrates a 1% mixing ratio, while the lower figure represents 3% mixing ratio.*

In the mass spectra, the expected protonated methanol ($CH_3OH_2^+$) at m/z 33 is observed along with further methanol-related ions. Those are $CH_3^+$, $CH_3O^+$, $CH_3OH{\cdot}CH_3^+$, $(CH_3OH)_2H^+$, $(CH_3OH)_2{\cdot}CH_3^+$, $(CH_3OH)_3H^+$ at m/z 15, 31, 47, 65, 79 and 97, respectively. These ion abundances strongly vary with the methanol mixing ratio, with a clear trend to larger clusters from 1% to 3%.

The primary focus is on protonated methanol, $CH_3OH_2^+$ (m/z 33), as a second reactant generated by proton-transfer reaction (*Rn 1*). The secondary reactant can react with the analyte M if the process is thermodynamically favorable, yielding the adduct ion at m/z $M{\cdot}CH_3OH_2^+$, or the protonated analyte $MH^+$.

$$M + CH_3OH_2^+ \rightarrow M{\cdot}CH_3OH_2^+ \quad (Rn\ 27)$$
$$\rightarrow MH^+ + CH_3OH \quad (Rn\ 27a)$$

In the formation of higher cluster ions, the feasibility of building further hydrogen bonds plays a critical role and significantly influences the reaction kinetics [81].

$$nCH_3OH + CH_3OH_2^+ \rightarrow (CH_3OH)_nH^+ \quad (Rn\ 28)$$

Here, n denotes the number of methanol molecules forming the cluster. This number increases depending on the concentration of neutral molecules and pressure [82,83]. Within the applied pressure range up to 8.0 mbar, even the $(CH_3OH)_4H^+$ cluster was observed, albeit with rather low abundance. The thermodynamic stability, and thus the equilibrium cluster distribution, depends on the reduction in potential energy per added neutral molecule as well as on the manifold of possible cluster configurations. In contrast to proton-bound water clusters [84,85], methanol clusters provide only a limited variety of configurations around the proton and are unable to form an extended, delocalized hydrogen-bonded network, which partially explains this pronounced cut-off.

A further cluster sequence is observed for the fragment $CH_3^+$, formed when methanol reacts with the primary ion $H_3^+$ (cf. *Rn 20b*). This ion reacts with neutral methanol molecules to form the clusters $CH_3OH{\cdot}CH_3^+$ at m/z 47 and $(CH_3OH)_2{\cdot}CH_3^+$ (at m/z 79), respectively [82], which are also shown in *Figure 4.38*.

$$CH_3OH + CH_3^+ \rightarrow CH_3OH{\cdot}CH_3^+ \quad (Rn\ 29)$$
$$\rightarrow (CH_3OH)_n{\cdot}CH_3^+ \quad (Rn\ 29a)$$

The base peak (cf. *Figure 4.38*) for the 1% methanol/SA mixing is observed at m/z 33 with an abundance of ($420 \pm 1 \times 10^9$ cps). The methanol-related relative ion intensities (related to m/z 33) are $11 \pm 0.2\%$, $14 \pm 0.2\%$, 0.2±0.02% and $0.1 \pm 0.01\%$ for m/z 47, 65, 79 and 97, respectively. The increase of the mixing ratio to 3% methanol changes the base peak to the first

cluster at m/z 65 ( $37.7 \pm 1 \times 10^9$ cps) and the relative ion abundances (related to m/z 65) are $83 \pm 1\%$, $14 \pm 0.2\%$, $7.6 \pm 0.1\%$ and $16 \pm 0.2\%$ for m/z 33, 47, 79 and 97, respectively.

As shown in *Figure 4.39*, the abundances of protonated methanol clusters change with increasing the mixing ratio, however, the cluster distribution is not simply shifted toward higher mass clusters; rather, it appears to saturate at n=3 corresponding to $(CH_3OH)_3H^+$ at m/z 97. Consequently, in the 12% methanol/SA mixture the base peak is clearly observed at m/z 97 (cf. *Figure 4.39*), while all other methanol-related ions appear at relatively (related to base peak) low intensities of 2.6±0.1%, 0.8±0.1%, 12.6±0.1%, and 4.7±0.1% for $CH_3OH_2^+$, $CH_3OH{\cdot}CH_3^+$, $(CH_3OH)_2H^+$ and $(CH_3OH)_2{\cdot}CH_3^+$ at m/z 33, 47, 65 and 79, respectively. The absolute intensity recorded for $(CH_3OH)_3H^+$ is $98.7 \pm 2 \times 10^9$ cps.

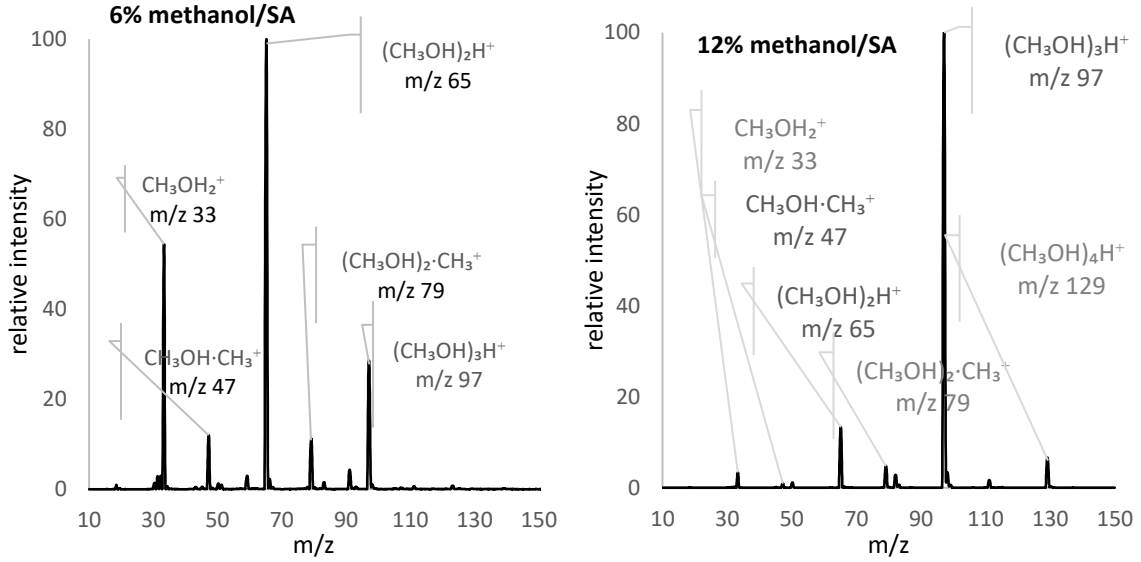


*Figure 4.39: Profile spectra of different mixtures of methanol/SA. The observed mixing ratios were 6% on the left and 12% on the right.*

*Measurement of oxygenated compounds using $CH_3OH$/synthetic air mixing reagent*

A series of alcohols (methanol, ethanol, iso-propanol, and n-butanol) were investigated in the previous section using $N_2/H_2$ reagent gas. In the following experiments, the methanol/SA mixing gas is used as a reagent (cf. profile spectrum in *Figure 4.38*) and ethanol, iso-propanol, and n-butanol are used as analytes. Due to the methanol/SA mixing gas being used as a reagent, the background ions with higher abundance of $CH_3OH_2^+$, $CH_3OH{\cdot}CH_3^+$, $(CH_3OH)_2H^+$, $(CH_3OH)_2{\cdot}CH_3^+$ and $(CH_3OH)_3H^+$ at m/z 33, 47, 65, 79, 97, and so forth are formed. These reactants may react with the neutral molecules and the possible ions may form via protonation and/or electrophilic addition. It is noted that the reaction rate coefficient (k) for the reaction between reactant ions (e.g., $CH_3OH_2^+$) and alcohols has not been reported in the scientific literature; therefore, the value of k has not been provided.

*Measurement of ethanol/SA*

In this experiment, ethanol ($C_2H_5OH$, M) at a mixing ratio of 2.6 ppmV in synthetic air (~ 4.0 sccm) was used as the analyte gas, and hydrogen was supplied as the plasma gas at a flow rate of 3 sccm. In addition, a 1.5% methanol/SA mixture was introduced into the sample line as the reagent gas. Under these conditions, the profile spectra of ethanol/SA and SA shown in *Figure 4.40* were recorded. The y-axis is normalized to the maximum signal of the protonated methanol dimer ($(CH_3OH)_2H^+$) at m/z 65, with an absolute intensity of $478 \pm 10 \times 10^9$ cps, and all signals are expressed as relative intensities in %. The expected molecular ions are indicated in the profile spectra over the m/z range 20 to 150. In addition, the region from m/z 58 to 64 is presented in an enlarged (zoomed) view to highlight the $M{\cdot}CH_3^+$ at m/z 61, as shown in *Figure 4.40.*

In the profile mass spectra of ethanol/SA, a peak at m/z 47 is observed, which is commonly assigned to the protonated ethanol ($MH^+$) ion $C_2H_5OH_2^+$. This ion can be formed via the following reaction:

$$M + CH_3OH_2^+ \rightarrow MH^+ + CH_3OH \qquad \textit{(Rn 30)}$$

However, the nominal m/z 47 value also corresponds to the $CH_3OH{\cdot}CH_3^+$ ion (cf. *Rn 29*) or $((CH_3OH)_2H^+ - H_2O)$ [80], which is likewise detected when SA is introduced into the reaction

chamber. In addition, a signal at nominal m/z 79 is also shown in both the ethanol/SA and SA-only spectra (cf. *Figure 4.40*). This peak originates from the methanol/SA reagent gas and can be attributed to the methanol-cluster ion $(CH_3OH)_2 \cdot CH_3^+$ (cf. *Rn 29*a) and the ethanol–methanol adduct ion, $CH_3OH \cdot MH^+$ (cf. *Rn 31*).

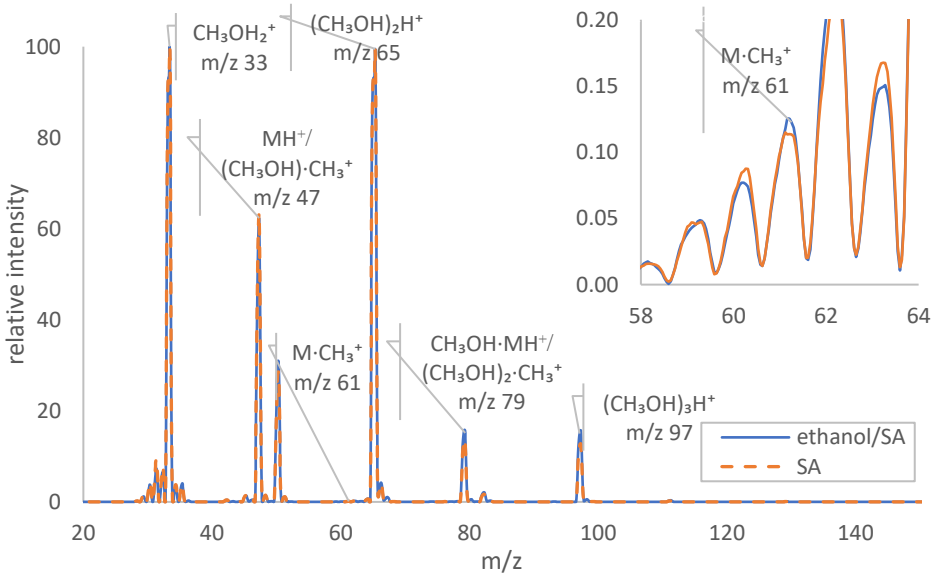


*Figure 4.40: Profile spectra of ethanol/SA mixture as analyte and only SA using 1.5% methanol/SA mixing reagent.*

The formation of $CH_3OH \cdot MH^+$, a proton from $CH_3OH_2^+$ transfers to the ethanol molecule (cf. *Rn 30*) and then protonated ethanol reacts again with a methanol molecule. Due to the higher methanol concentration, an adduct ion ($CH_3OH \cdot MH^+$) is formed, which is given below:

$$CH_3OH \quad + \quad MH^+ \rightarrow \quad CH_3OH \cdot MH^+ \qquad (Rn\ 31)$$

Since signals at m/z 47 and 79 are also present in the background when only the methanol/SA mixture is introduced, their net abundances were obtained by subtracting the background intensities from those measured with 2.6 ppmV ethanol/SA in this system. The resulting intensities are $2.7 \pm 0.6 \times 10^9$ and is $8.0 \pm 0.5 \times 10^9$ cps, respectively. The background signals of these ions, however, were likewise high (on the order of $10^9$ cps). Hence, to further assess whether ethanol has any effect on these signals, a variation study of the ethanol/SA mixture was carried out. An ethanol/SA mixture at 90 ppmV was introduced at different dilution levels, with 1% methanol/SA as reagent gas. The results are shown in *Figure 4.41*,

where the x-axis represents the mixing ratio of ethanol and the y-axis the absolute intensity in cps.

In this figure, the left panel shows the dependence of ion intensities of $CH_3OH{\cdot}MH^+/(CH_3OH)_2{\cdot}CH_3^+$ at m/z 79 and $CH_3OH_2^+$ at 33 on the mixing ratio, while the right panel shows the corresponding dependence for $CH_3^+$, $MH^+/CH_3OH{\cdot}CH_3^+$ and $(CH_3OH)_2H^+$, at m/z 15, 47 and 65, respectively.

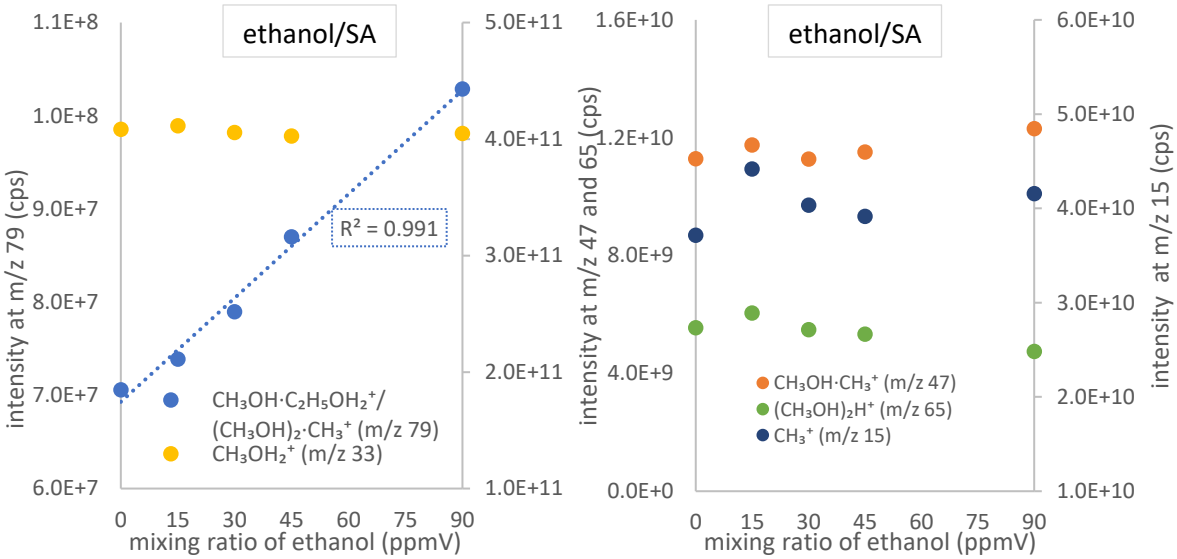


*Figure 4.41: Dependency of ion abundances on varying the mixing ratios of ethanol/SA using 1% methanol/SA mixing reagent gas.*

The left panel of *Figure 4.41* shows that the ion abundances $CH_3OH_2^+$ at m/z 33 remain stable at $430 \pm 10 \times 10^9$ cps, where as the ion intensity of $CH_3OH{\cdot}MH^+/(CH_3OH)_2{\cdot}CH_3^+$ at m/z 79 increases with increasing ethanol mixing ratio, with a linear correlation coefficient of $R^2$ = 0.991. However, the ion intensities of $CH_3^+$ (m/z 15), $MH^+/CH_3OH{\cdot}CH_3^+$ (m/z 47) and $(CH_3OH)_2H^+$ (m/z 65) remain constant (cf. right panel of *Figure 4.41*) over the investigated range of ethanol/SA mixing ratios. Therefore, the increasing intensity at m/z 79 indicates that the generated ion is related to the ethanol adduct ion $CH_3OH{\cdot}MH^+$.

Another possible adduct ion at m/z 61 forms via reaction between $C_2H_5OH$ (M) and $CH_3^+$, as also shown in *Figure 4.40* in the m/z 58 - 64. The reaction is:

$$M + CH_3^+ \rightarrow M{\cdot}CH_3^+ \qquad \textit{(Rn 32)}$$

This adduct ion is observed only as a small peak compared to the corresponding signal in the mixing gas (SA). Its abundance of $M{\cdot}CH_3^+$ at m/z 61 was determined by subtracting the contribution of the mixing gas at the same m/z, yielding an abundance of $2.8 \pm 2 \times 10^7$ cps.

In summary, ethanol (M) can be quantified using the methanol/SA reagent via the signal of $CH_3OH{\cdot}MH^+$ at m/z 79, as evidenced by the linear correlation between its ion abundance and the ethanol mixing ratio. However, the corresponding background signal in the absence of ethanol is relatively high due to the methanol cluster ion. In addition, the signals at m/z 47 and 61 are also associated with methanol- and ethanol-related species.

Since a QMS is employed in this study, these ions can be subjected to further fragmentation in the Q2 mass filter to obtain structural information and to confirm the assignment of ethanol-related ions. Accordingly, the fragmentation behavior of the ions at m/z 47, 61, and 79 is examined in *section 4.8.1*.

*Measurement of iso-propanol/synthetic air*

Isopropanol ($C_3H_7OH$, denoted as M) at a mixing ratio of 1.4 ppmV in SA was used as the analyte gas, and a 1% methanol/SA mixture served as the reagent. The PG ($H_2$) flow rate was set to 3.0 sccm, and the analyte flow rate to 4.0 sccm. The corresponding profile spectra of isopropanol/SA (blue line) and SA alone (orange dotted line) are shown in *Figure 4.42*. The y-axis is normalized to the signal of $(CH_3OH)_2H^+$ at m/z 65 ($460 \pm 0.3 \times 10^9$ cps) and displays the relative intensity in %. Because the abundance of the molecular ion is relatively low, the y-axis is shown on an expanded scale.

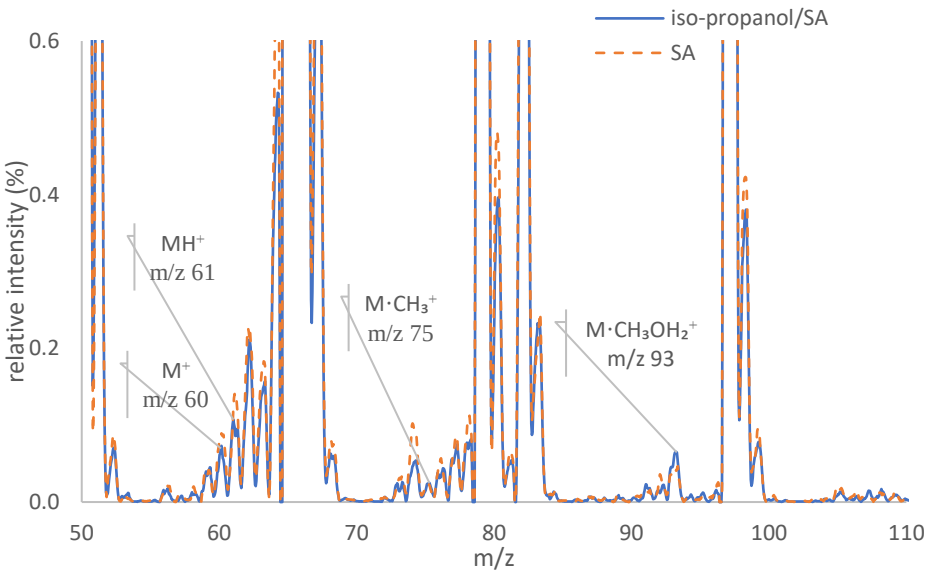


*Figure 4.42: Profile spectra of iso-propanol/SA mixture as the analyte gas (blue) and only SA (orange) within m/z 50 to 110 using a 1% methanol/SA mixture as the reagent gas.*

In the profile spectrum, analyte-related ions $M^+$, $MH^+$, and $M{\cdot}CH_3^+$ are observed at m/z 60, 61, and 75, respectively. The molecular ion $M^+$ can be generated either via reaction with $O_2^+$ or by photoionization, as discussed in *section 4.7.2*. The protonated molecule $MH^+$ is formed by proton-transfer reactions between neutral iso-propanol and $CH_3OH_2^+$, as well as other relevant protonated methanol cluster ions originating from methanol/SA reagent. The abundance of these reactant ions is approximately 90% of the base peak, whereas the product ion intensity is only about 0.1% of the base peak, which may indicate a relatively low reaction rate coefficient or reduced interaction time. As noted previously, the corresponding rate coefficient k has not been reported in the literature.

Moreover, the reactant ion $CH_3^+$ (cf. *Rn 21b*) can also react with M to form an adduct at m/z 75 (cf. e.g., *Rn 32*). These ions ($M^+$, $MH^+$, and $M{\cdot}CH_3^+$) are likewise observed in the SA reference,

where they appear with higher abundances than in the analyte gas, presumably due to a higher level of impurities in the methanol/SA reagent gas. Consequently, the ions at m/z 60, 61, and 75 cannot be used for the analysis of $C_3H_7OH$ in this system.

At m/z 93, a signal is observed in both the reference and the iso-propanol spectra (cf. *Figure 4.42*), however, with lower abundance in the reference. This ion species can be generated via reaction of the $CH_3OH_2^+$ reactant ion with the $C_3H_7OH$ molecule (M), forming the adduct ion $CH_3OH{\cdot}MH^+$, as described by:

$$M + CH_3OH_2^+ \rightarrow CH_3OH{\cdot}MH^+ \qquad (Rn\ 33)$$

Therefore, the ion abundance of iso-propanol (1.4 ppmV) at m/z 93 was determined by subtracting the intensity of the mixing gas, which is $6.4 \pm 3 \times 10^6$ cps. The ion $CH_3OH_2^+$ may be considered the primary reactant ion for the analysis of $C_3H_7OH$. In addition, iso-propanol/SA with a mixing ratio of 45 ppmV was employed in a separate experiment to evaluate the sensitivity at different mixing ratios (cf. *Figure 4.43*). At m/z 93, a coefficient of determination $R^2 = 0.9937$ was obtained. To verify the absence of interferences during the dilution experiment, the signal intensity at m/z 33, corresponding to protonated methanol ($CH_3OH_2^+$), was also plotted and was found to remain essentially constant.

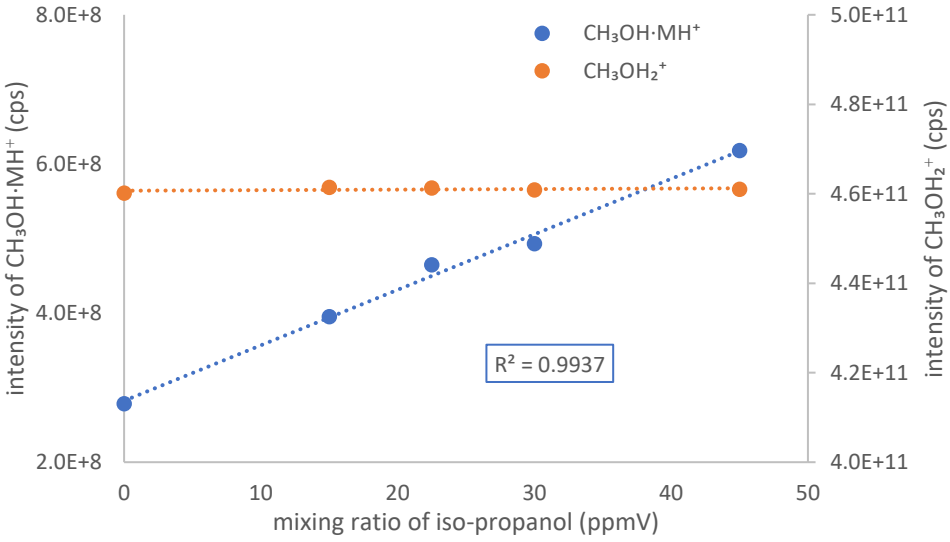


*Figure 4.43: Dependence of ion intensities of $CH_3OH_2^+$ and $CH_3OH.MH^+$ on the iso-propanol/SA mixing ratio using 1% methanol/SA as the reagent. Iso-propanol/SA with 45 ppmV was used for preparing mixing ratios.*

*Measurement of n-butanol/synthetic air*

In this experiment, 14 ppmV n-butanol (M) in synthetic air (SA) was investigated using a reagent gas consisting of 3% methanol in SA. The n-butanol/SA mixture and SA with reagent gas were introduced into the system as analyte gas and background gas, respectively. The resulting profile spectra in the m/z range 50–140 are shown in *Figure 4.44*. In these spectra, the blue line and the orange dotted line correspond to n-butanol/SA and SA, respectively. The y-axis is again normalized to the $(CH_3OH)_2H^+$ ion and represents the relative intensity in %.

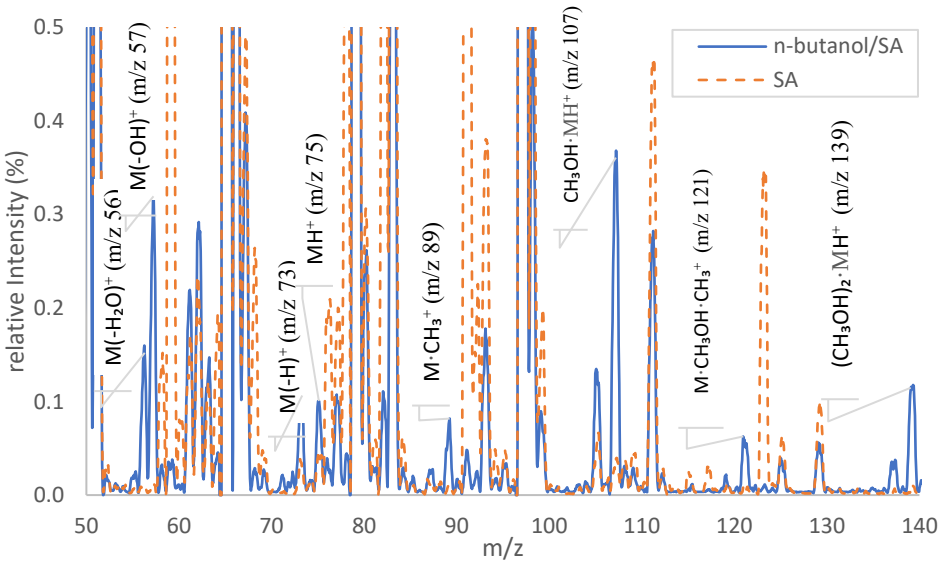


*Figure 4.44: Profile spectra of n-butanol/SA and SA with 3% methanol/SA mixing reagent are shown as blue line and dotted orange line, respectively.*

The primary target ion is the protonated molecular ion $MH^+$ at m/z 75, which is clearly observed in the profile spectra. It is formed via proton transfer from the $CH_3OH_2^+$ reactant ion to the n-butanol molecule. Additional butanol-related ions, $M(-H)^+$, $M(-OH)^+$ and $M(-H_2O)^+$ are detected at m/z 73, 57 and 56, respectively. These fragment ions are produced when n-butanol reacts with the $O_2^+$, as discussed in the previous section (cf. *Section 4.7.2*).

In addition to the protonated molecular ion and its fragment ions (cf. *Figure 4.44*), a series of adduct ions $M{\cdot}CH_3^+$, $CH_3OH{\cdot}MH^+$, $M{\cdot}CH_3OH{\cdot}CH_3^+$, and $(CH_3OH)_2{\cdot}MH^+$ are observed at m/z 89, 107, 121, and 139, respectively. These ions can be formed via electrophilic addition reactions between $C_4H_9OH$ and the reactant ions $CH_3^+$, $CH_3OH_2^+$, $CH_3OH{\cdot}CH_3^+$, and $(CH_3OH)_2H^+$, respectively. The corresponding reactions are given below:

| | | | | | |
|---|---|---|---|---|---|
| M | + | $CH_3^+$ | → | $M \cdot CH_3^+$ | (*Rn 34*) |
| M | + | $CH_3OH_2^+$ | → | $CH_3OH \cdot MH^+$ | (*Rn 35*) |
| M | + | $(CH_3OH) \cdot CH_3^+$ | → | $M \cdot CH_3OH \cdot CH_3^+$ | (*Rn 36*) |
| M | + | $(CH_3OH)_2H^+$ | → | $(CH_3OH)_2 \cdot MH^+$ | (*Rn 37*) |

Among the detected ions, the species at m/z 107, assigned to $CH_3OH \cdot MH^+$, is the most abundant, with an absolute intensity of $(13.5 \pm 0.2) \times 10^7$ cps. The relative abundances of the molecular and fragment ions $MH^+$, $M^+$, $M(-H)^+$, $M(-OH)^+$ and $M(-H_2O)^+$, normalized to the total molecular-ion signal (including methanol-associated ions), are $7 \pm 2\%$, $2 \pm 1\%$, $7 \pm 1\%$, $22 \pm 2\%$, and $12 \pm 3\%$, respectively. The relative abundances of the adduct ions are $6 \pm 2\%$ for $M \cdot CH_3^+$, $29 \pm 4\%$ for $CH_3OH \cdot MH^+$, $5 \pm 1\%$ for $M \cdot CH_3OH \cdot CH_3^+$ and $10 \pm 1\%$ for $(CH_3OH)_2 \cdot MH^+$.

It is noteworthy that the ion abundance of the $CH_3OH \cdot MH^+$ species at m/z 107 is approximately four times higher than that of the protonated analyte ion $MH^+$ at m/z 75. Consequently, the ion intensities at m/z 107 were examined as a function of the n-butanol/SA mixing ratio using 1% methanol/SA reagent gas, as shown in *Figure 4.45*. The x-axis represents the mixing ratio in ppmV, and the y-axis shows the absolute intensity in cps.

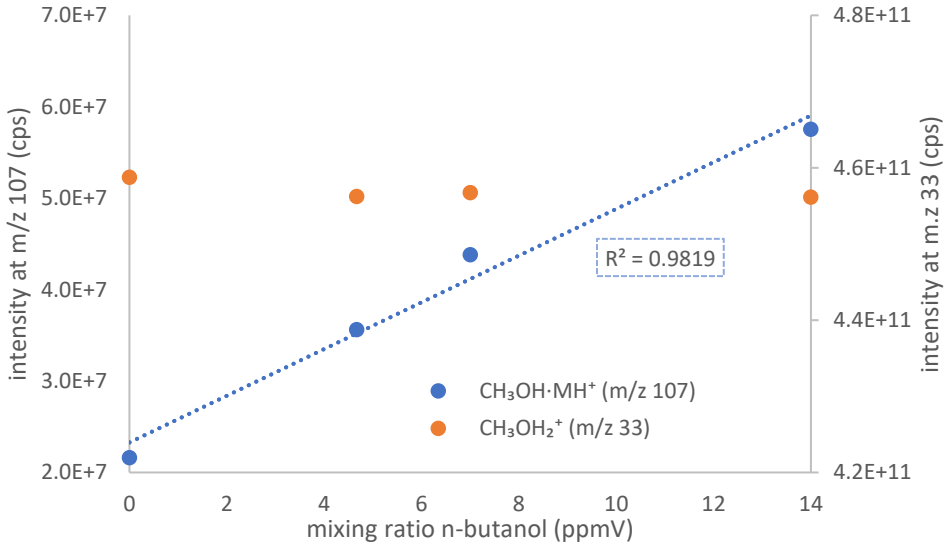


*Figure 4.45: Ion intensities of $CH_3OH \cdot MH^+$ (m/z 107) and $CH_3OH_2^+$ (m/z 33) as a function of n-butanol/SA mixing ratio, using 1% methanol/SA reagent gas.*

In this experiment, a 14 ppmV n-butanol mixture was prepared and further diluted with synthetic air. The ion intensity of $CH_3OH{\cdot}MH^+$ at m/z 107 was found to increase with increasing mixing ratio, yielding a linear correlation with $R^2 = 0.9819$. While the reactant ion $CH_3OH_2^+$ intensity at m/z 33 was stable with increasing mixing ratio of n-butanol. This result indicates that, in the presence of methanol/SA reagent gas, adduct formation is more favorable than simple proton-transfer, leading to a higher abundance of the adduct ion.

In summary, it was observed that the expected protonated molecular ions ($MH^+$) were not formed during the analysis of alcohols (ethanol, iso-propanol, and n-butanol) when using the $N_2/H_2$ reagent gas; instead, extensive molecular fragmentation occurred under these conditions. In contrast, when a methanol/SA mixed reagent gas was employed, adduct ions ($CH_3OH{\cdot}MH^+$) were formed for ethanol, iso-propanol, and n-butanol at m/z 79, 93, and 107, respectively, with $CH_3OH_2^+$ acting as the reactant ion. The corresponding ion abundances were measured to be $3.1 \pm 0.2 \times 10^9$, $0.5 \pm 0.2 \times 10^7$ and $1.0 \pm 0.1 \times 10^7$ cps/ppmV, respectively. These results indicate that the methanol/SA reagent gas is, to some extent, suitable for the qualitative and quantitative analysis of alcohols, enabling molecule detection with reduced fragmentation.

## 4.8 Characterization of Adduct Ion

### 4.8.1 Adduct Ion Fragmentation

The measurement of the analyte (M) using a 1% methanol/SA reagent gas leads to the formation of adduct ions whose nominal masses overlap with those of other ion species. For example, in the case of ethanol, the adduct ions $MH^+$ and $CH_3OH{\cdot}MH^+$ are observed at m/z 47 and m/z 79, respectively, when 1% methanol/SA is used as reagent gas (cf. *section 4.7.3*). The ion at m/z 47 corresponds to the $((CH_3OH)_2H^+ - H_2O)$, which is formed from a methanol cluster ion. Schubert *et al.* reported that additional ions originating from methanol clusters can form according to the general formula $(CH_3OH)_nH^+ - H_2O$ [80]. Consequently, fragmentation of the adduct ions is required for further structural characterization and thus unambiguous identification.

For molecular fragmentation induced by collision induced dissociation (CID) at relatively high pressure (mTorr range, 1mTorr = 1.33 mbar), the TQMS technique has been developed [86,87]. In this section, the product-ion scan mode is employed to fragment the molecular adduct ions of ethanol, isopropanol, and n-butanol that were observed in the previous experiments (cf. *section 4.7.3*).

*Ethanol*

In this experiment, ethanol was investigated first. Since the adduct ions of ethanol in SA are observed at m/z 47, 61, and 79 (cf. *Figure 4.40*), these ions were selected for further characterization. Each ion was isolated in the Q1 mass filter as a precursor ion ($M_{pe}{}^+$), and the Q3 mass filter was set to scan over a defined m/z range. In this configuration, Q1 transmits only the selected precursor ion to Q2, where argon at a pressure of 0.5 mTorr is used as the CID gas and a collision energy of 5 eV is applied to induce fragmentation. Subsequently, Q3 scans the mass range from m/z 10 to 100 to record the product ion spectra. The resulting spectra are shown in *Figure 4.46;* the upper-left, upper-right and lower-left panels correspond to the precursor ions at m/z 47 (denoted PI mz 47), 61 (denoted PI mz 61) and 79 (denoted PI mz 79), respectively. For comparison, the spectrum at m/z 79 obtained from methanol/SA alone is shown in the lower-right panel.

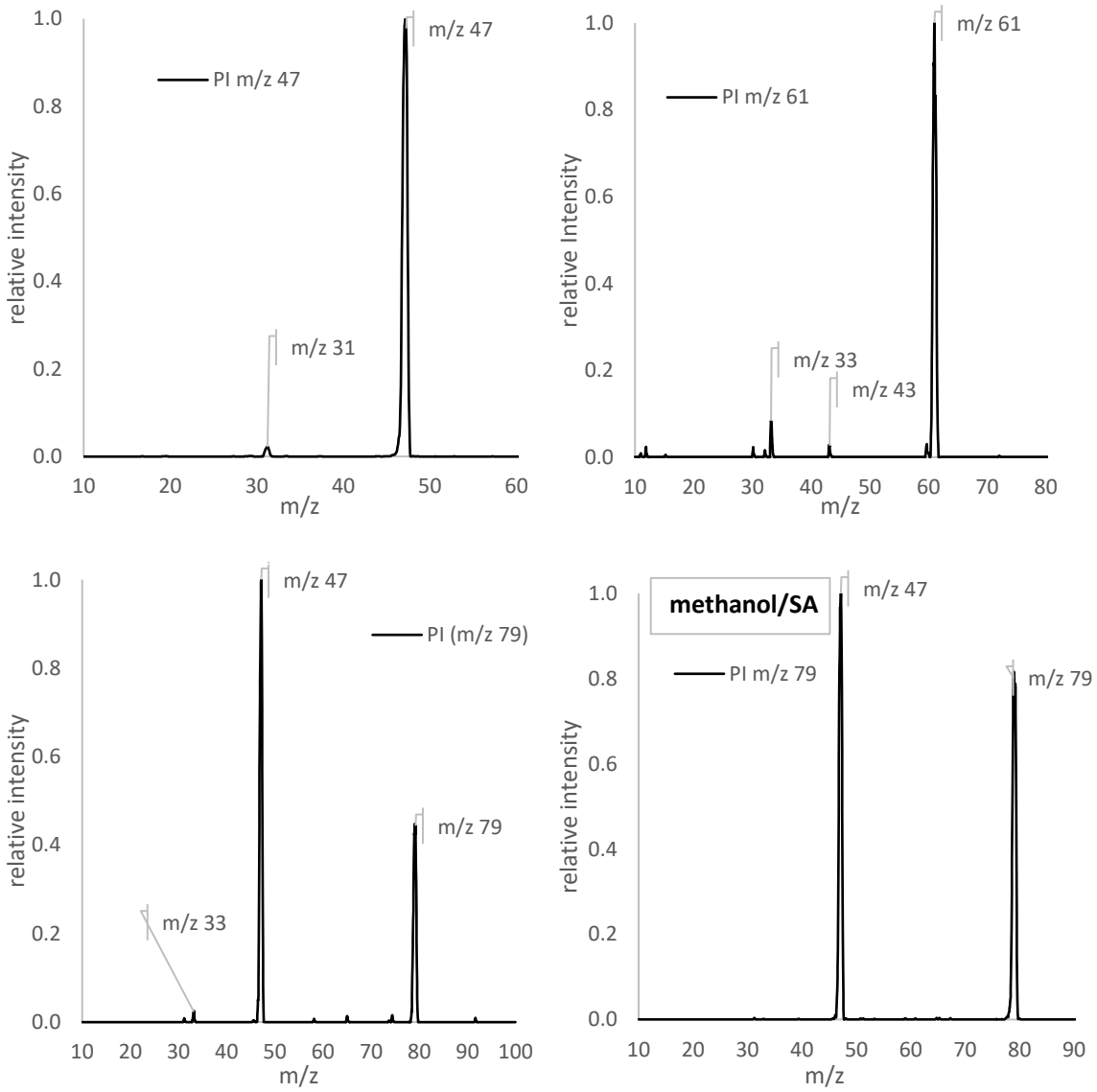


*Figure 4.46: Profile spectra of fragmented adduct ions of ethanol in SA, obtained with a CID gas pressure of 0.5 mTorr and a collision energy of 5 eV. The product-ion spectra for precursor ions at m/z 47, 61, and 79 are shown in the upper-left, upper-right, and lower-left panels, respectively. The lower-right panel displays the fragmentation pattern of the m/z 79 ion obtained using methanol/SA alone.*

The upper-left *Figure 4.46* illustrates the dissociation of the ion at m/z 47. The observed ions using CID gas pressure of 0.5 mTorr and a collision energy of 5 eV are m/z 47 and 31. The fragment ion at m/z 31 is attributed to the loss of a $CH_3$ group from the ethanol molecule ($C_2H_5OH$). In this process, protonated ethanol ($MH^+$) initially undergoes hydrogen loss to form

the molecular ion ($M^+$), which subsequently eliminates a $CH_3$ fragment to produce the $CH_2OH^+$ ion at m/z 31.

The NIST mass spectrometry database provides reference EI spectra of ethanol (NIST MS number 118507) [25], in which m/z 31 is the dominant fragment ion. However, in the present CID experiment, the m/z 31 fragment was observed with relatively low intensity. In addition, ethanol-related product ions expected from the loss of OH or $H_2O$, which would appear at m/z 30 and/or 29, were not detected in the profile spectrum. To further elucidate the fragmentation behavior of this precursor ion, the collision energy and CID gas pressure were systematically varied in subsequent experiments, as discussed in *Sections 4.8.2 and 4.8.3*.

For the precursor ion at m/z 61, the corresponding fragment spectrum is shown in the upper-right panel of *Figure 4.46*. The signals at m/z 33 and 43 can be attributed to $CH_3OH_2^+$ and to background-related species, respectively. However, the expected fragment ions corresponding to $MH^+$ and/or $M^+$, at m/z 47 and 46, respectively, were not observed under these conditions. Furthermore, no characteristic ethanol fragment ions arising from the loss of $CH_3$, OH or $H_2O$, typically expected at m/z 31, 30 and 29, were not detected. Consequently, this ion at m/z 61 is not considered to be related to ethanol.

Furthermore, the ethanol-related ion at m/z 79 was investigated, and the corresponding product-ion spectrum is shown in the lower-left panel of *Figure 4.46.* Fragmentation of the m/z 79 precursor ($M_{pe}{}^+$) yields ions at m/z 33, m/z 47, as well as a residual signal at m/z 79. The peak at m/z 47 is assigned to protonated ethanol ($C_2H_5OH_2{}^+$), formed by loss of methanol from the precursor ($M_{pe}{}^+ - CH_3OH$). This fragmentation pathway indicates that the adduct ion at m/z 79 is directly associated with ethanol. However, an ion at m/z 79 is also observed when only methanol/SA is introduced into the system. The corresponding fragmentation pattern is shown in the lower-right panel of *Figure 4.46.* In this case, an ion at the m/z 47 is also produced, but with lower intensity than in the ethanol/SA experiment.

At a CID gas pressure of 0.5 mTorr and a collision energy of 5.0 eV, $C_2H_5OH_2{}^+$ at m/z 47 is the dominant ion, accounting for $62 \pm 3\%$ of the total fragment ion signal. A minor contribution from protonated methanol is observed at m/z 33, with a relative abundance of $1 \pm 0.2\%$. The remaining unfragmented precursor at m/z 79 constitutes $37 \pm 1\%$ of the total ion intensity. In contrast, for methanol/SA alone (lower-right panel of *Figure 4.46)*, the relative ion abundances are $51.9 \pm 3\%$ for m/z 47, $48 \pm 2\%$ for 79 and 0.1% for m/z 33. These results

demonstrate that ethanol can be reliably detected via the ion at m/z 79 when using the $CH_3OH$/SA mixed reagent gas.

*Iso-propanol*

Isopropanol was investigated in a subsequent experiment. The corresponding adduct ion had previously been identified at m/z 93 (cf. *Figure 4.36*). Therefore, the precursor ion ($M_{pp}{}^+$) at m/z 93 was selected in the Q1 mass filter. CID conditions were initially set to a gas pressure of 0.5 mTorr and a collision energy of 5 eV. Under these conditions, no fragmentation of the m/z 93 ion was observed, and only background noise was detected over the m/z range of 20–100.

Consequently, the collision energy was increased to 10 eV while maintaining the same CID gas pressure. Under these conditions, the adduct ion (denoted as PI m/z 93) underwent fragmentation, yielding several product ions at m/z 61, 47 and 33, as shown in *Figure 4.47*.

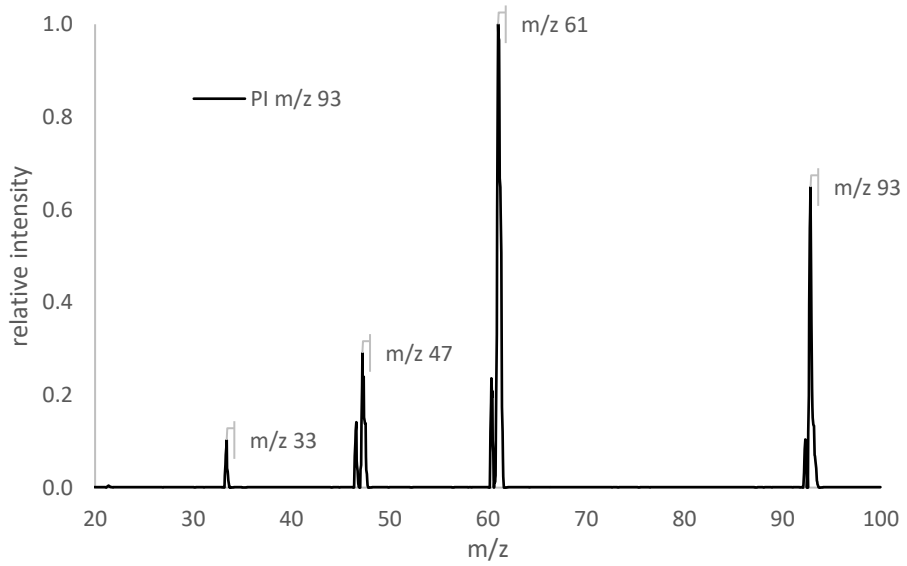


*Figure 4.47: Fragmented adduct ion of iso-propanol using 1% methanol/SA reagent gas. Argon with 0.5 mTorr as CID gas is introduced and 10 eV energy is applied.*

The fragment ion at m/z 61 is formed by loss of methanol from the precursor ion ($M_{pp}{}^+ - CH_3OH$) and is assigned to protonated isopropanol ($C_3H_7OH_2{}^+$, $MH^+$). A further ion is observed at m/z 47, which is likely attributable to impurities; the expected fragment corresponding to loss of an OH group from isopropanol was not detected. Another fragmented ion at m/z 33 is observed and assigned to protonated methanol.

The relative abundances of fragment ions are $63 \pm 10\%$ at m/z 61, $4 \pm 2\%$ at m/z 33, while the remaining unfragmented precursor at m/z 93 accounts for $33 \pm 6\%$ of the total ion signal.

*n-butanol*

The adduct ion of n-butanol (M, m/z 74) was observed at m/z 107 upon addition of the methanol/SA reagent gas (cf. *Figure 4.44*). To further characterize this adduct ion in product-ion mode, the precursor ion at m/z 107 was selected in Q1, and CID was performed using argon at a pressure of 0.5 mTorr and a collision energy of 5 eV. The mass filter was then scanned over the m/z range 20–120 to record the product-ion spectrum, which is shown in *Figure 4.48*.

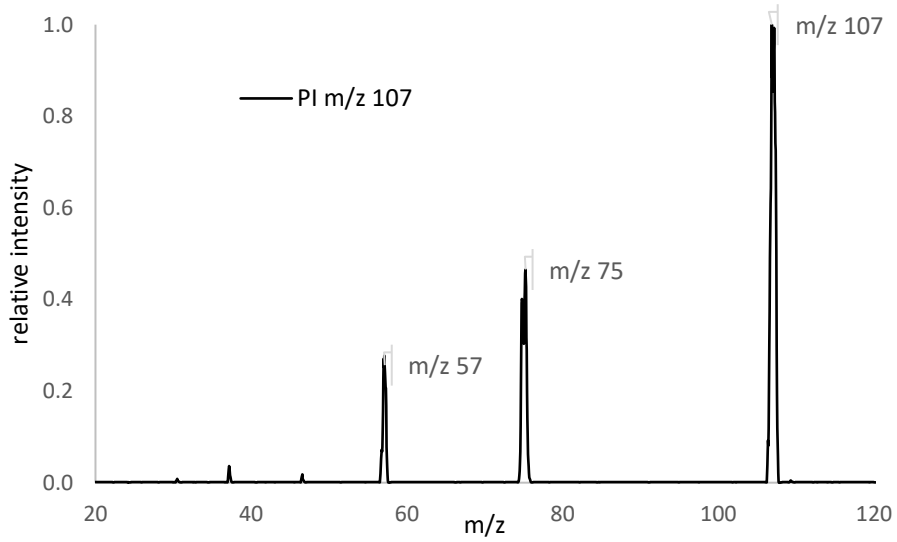


*Figure 4.48: Profile spectrum of fragmented n-butanol using 1% methanol/SA reagent gas. Argon with 0.5 mTorr as CID gas is introduced and 5 eV energy is applied.*

The product ion spectrum shows the precursor ion ($M_{pb}$), at m/z 107, together with prominent fragment ions at m/z 75 and m/z 57. The ion at m/z 75 is attributed to the loss of methanol from the precursor ion ($M_{pb}{}^{+} - CH_3OH$), yielding protonated n-butanol $C_4H_9OH_2^+$ ($MH^+$). The fragment at m/z 57 is assigned to $M(-OH)^+$, formed by loss of both methanol and water from the precursor, consistent with typical fragmentation pathways of alcohols. These fragmentation patterns confirm the structural assignment at m/z 107 of n-butanol associated with the $CH_3OH_2^+$, i.e. $CH_3OH \cdot C_4H_9OH_2^+$.

### 4.8.2 Adduct Ion Fragmentation using Fixed CID Energy with Pressure Variation

In the previous section, the precursor ion was fragmented at a fixed CID gas pressure and collision energy in order to identify the analyte molecule. However, further characterization is required to investigate how the fragmentation behavior changes with increasing CID gas pressure. Therefore, in the present section, the adduct ion of n-butanol was investigated as an example; the CID gas pressure was systematically varied, while the collision energy is kept constant.

The adduct ion ($CH_3OH \cdot C_4H_9OH_2^+$) of n-butanol at m/z 107 was identified in the previous n-butanol experiment. Therefore, this m/z has been selected as a precursor ion. To investigate the ion fragmentation dynamics, a constant energy (5 eV) is applied while the CID gas pressure is varied (0.5 to 3.0 mTorr). As the pressure increases from 0.5 to 3.0 mTorr, the observed fragmented ions change their intensity, which is shown in *Figure 4.49*. The y-axis of the following spectra is shown in relative intensity, with the x-axis representing the m/z scale.

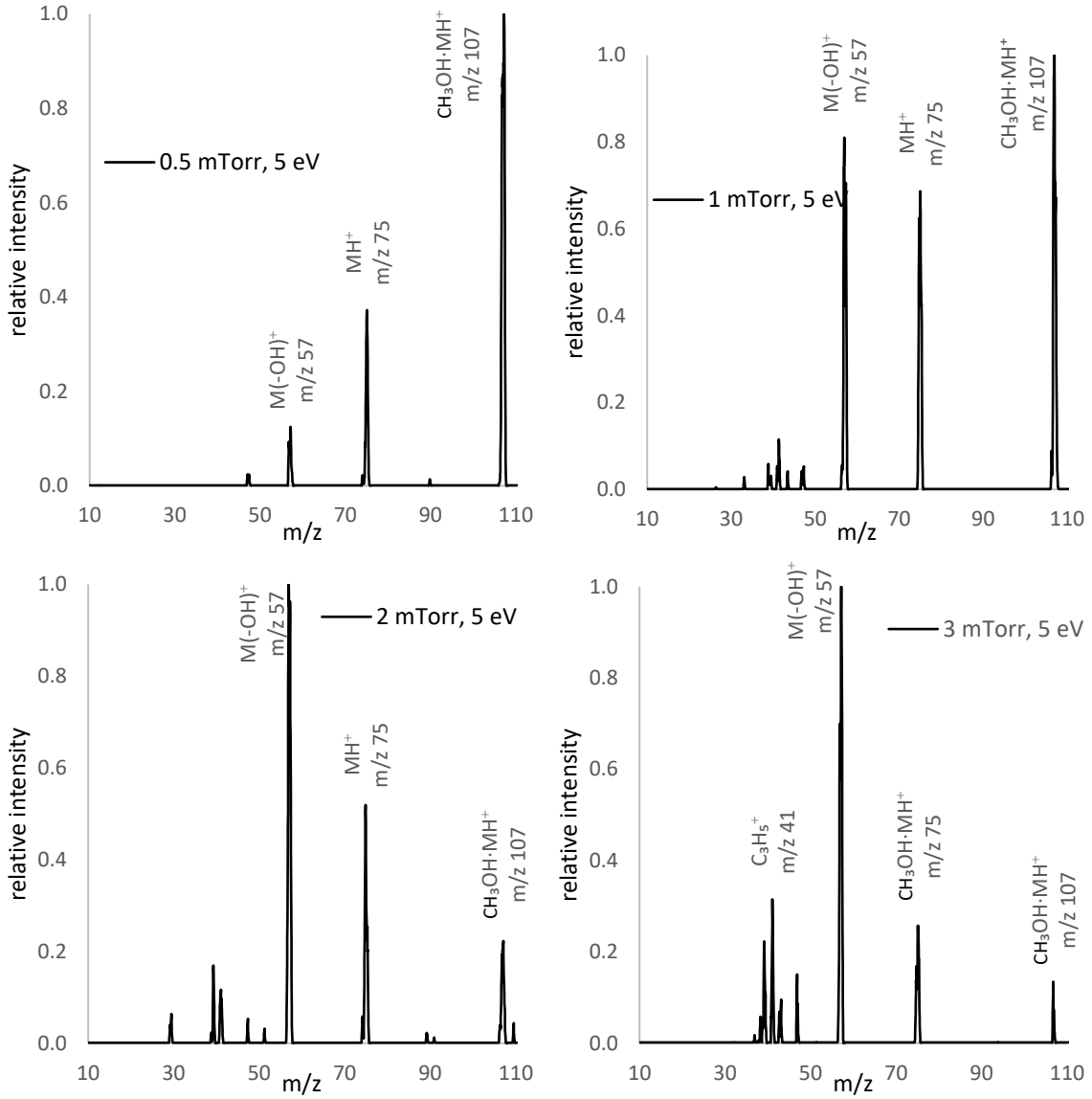


*Figure 4.49: Fragmented ion spectra of n-butanol/$CH_3OH_2^+$ adduct. Argon was used as the CID gas at different pressures, with energy set at 5 eV.*

As shown in the upper-left figure, at a collision-cell pressure of 0.5 mTorr, the n-butanol adduct ion ($CH_3OH{\cdot}MH^+$) undergoes partial fragmentation. Under these conditions, the product-ion spectrum exhibits relative intensities of $22 \pm 1\%$ and $8 \pm 0.5\%$ for the fragment ions $C_4H_9OH_2^+$ and $C_4H_9OH_2^+ - H_2O$ at m/z 75 ($MH^+$) and m/z 57 ($M(-OH)^+$), respectively, while the unfragmented precursor ion $CH_3OH{\cdot}MH^+$ at m/z 107 remained predominant with $70 \pm 1.5\%$ relative intensity. *Figure 4.50* summarizes the dependence of relative ion abundances (in %) on the induced CID gas pressure.

Upon increasing the collision-cell pressure, the abundance of the parent ion at m/z 107 progressively decreased, whereas the intensity of the fragment ion $M(-OH)^+$ at m/z 57 increased. In contrast, the behavior of $MH^+$ at m/z 75 fragment ion followed a different pattern: its intensity initially increased with pressure, reaching a maximum at approximately 1.0 mTorr. Beyond this point, further increases in pressure resulted in a gradual decline in its abundance.

Additionally, once the pressure increased from 0.5 to 1.0 mTorr, a new fragment ion at m/z 41 ($C_3H_5^+$) appeared. This species is formed through sequential losses of $H_2O$ and $CH_3$ from $MH^+$. As the pressure within the collision cell increases, the frequency of collisions rises, enhancing the transfer of kinetic energy to the precursor ions. Additional energy promotes the cleavage of increasingly stronger chemical bonds, thereby enabling the formation of lower-m/z product ions as the pressure is elevated [88].

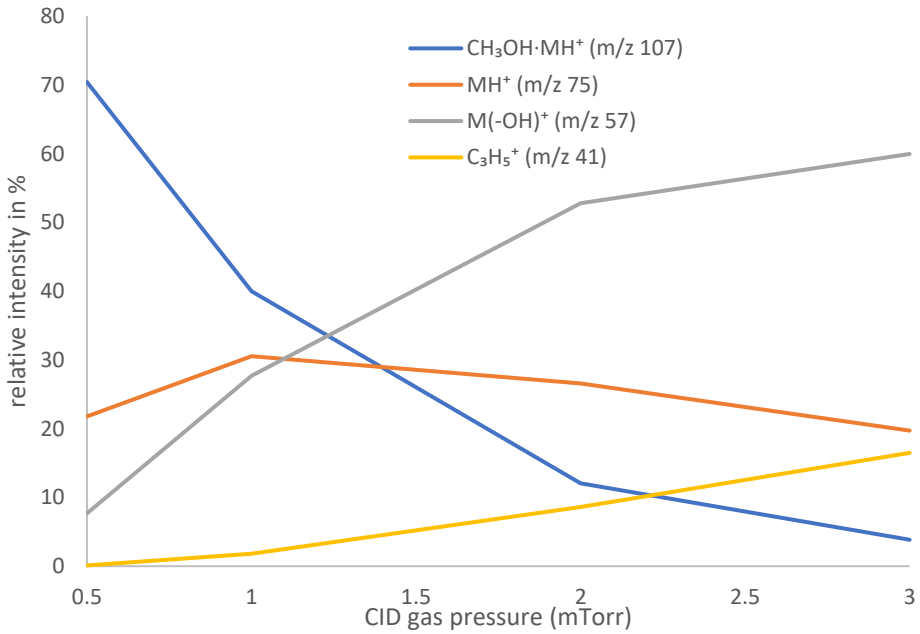


*Figure 4.50: Relative intensity of precursor and fragment ions at 5 eV collision energy with varying CID gas pressure.*

At the highest pressure investigated (3.0 mTorr), the relative intensities shifted significantly toward extensive fragmentation, yielding 4% for the precursor ion of $CH_3OH{\cdot}MH^+$ at m/z 107, 20% for the intermediate product $MH^+$ at m/z 75, 60% for $M(-OH)^+$ at m/z 57 and 16% for $C_3H_5^+$ at m/z 41.

The *Figure 4.50* demonstrates that increasing the CID gas pressure leads to a decrease in the precursor ion intensity while increasing the fragment ion abundances. Specifically, increasing

the pressure from 0.5 mTorr to 3.0 mTorr results in a 98% reduction in the precursor ion intensity.

In addition, fragmentation efficiency ($E_f$) is calculated from the precursor-to-product ion abundance ratios by the following equation: [86]

$$E_f = \frac{I_f}{(I+I_f)} \quad (7)$$

Where I and $I_f$ are the precursor ion intensity and total fragment ion intensity in the presence of CID, respectively, the calculated fragment efficiency of the precursor ion of $CH_3OH{\cdot}MH^+$ at m/z 107 at 0.5, 1.0, 2.0 and 3.0 mTorr CID gas pressures with 5 eV energy are 30%, 60%, 88% and 96%, respectively.

### 4.8.3 Adduct Ion Fragmentation using Fixed CID Gas Pressure with Energy Variation

Investigation of the effect of varying collision energy at a constant CID gas pressure of 0.5 mTorr revealed pronounced changes in the fragmentation behavior of the n-butanol (M) adduct ion $CH_3OH{\cdot}MH^+$ at m/z 107, as shown in *Figure 4.51*. Increasing the dissociation energy in the collision cell enhances the effectiveness of ion–molecule collisions, thereby altering the fragmentation pattern of the precursor ion.

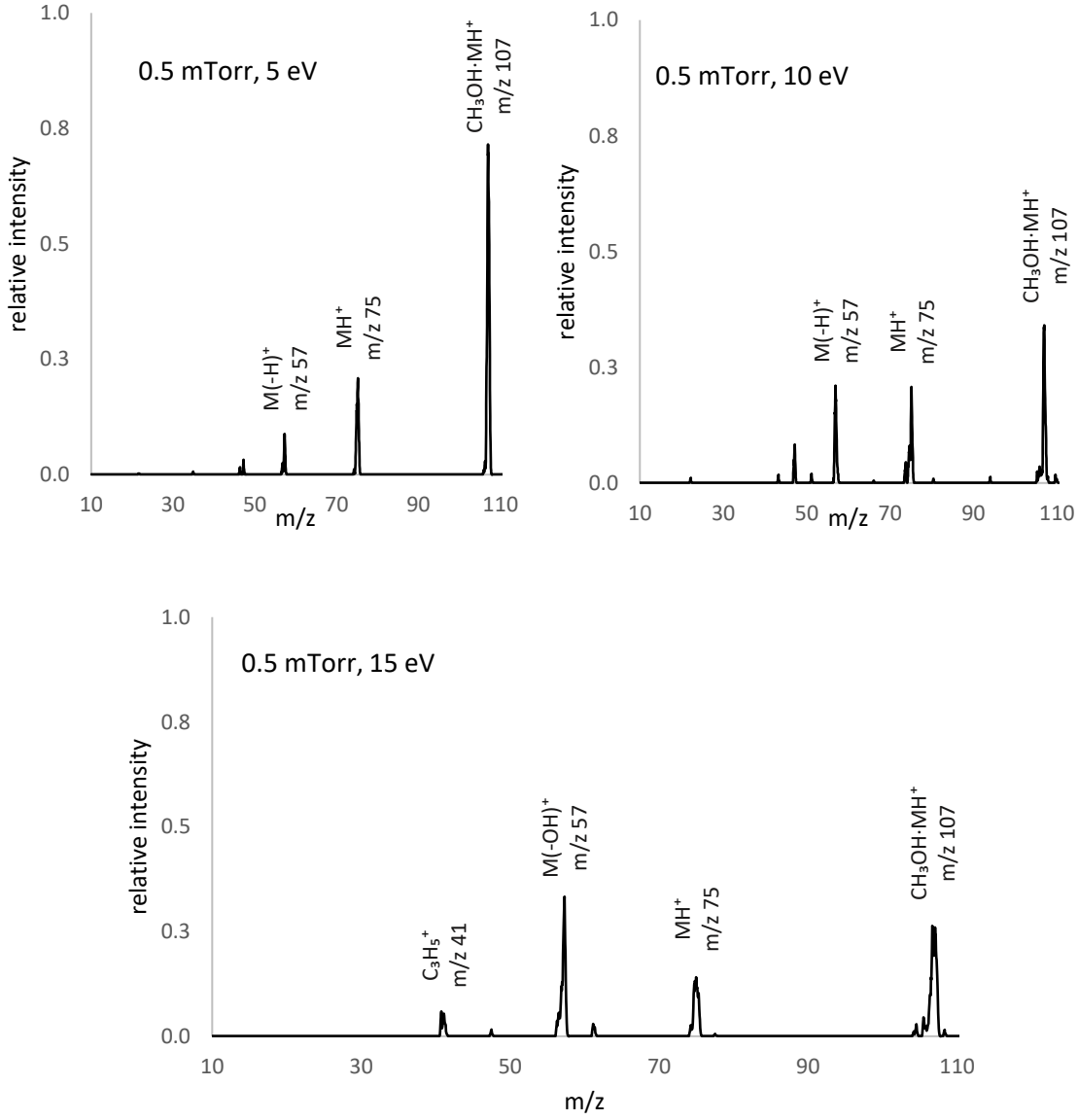


*Figure 4.51: Fragment spectra of the adduct ion m/z 107 of n-butanol using $CH_3OH$/SA reagent gas at 0.5 mTorr CID gas with varying collision energies.*

At an applied energy of 5 eV and a CID gas pressure of 0.5 mTorr, the precursor ion at m/z 107 exhibited a relative intensity of 70%. The fragment ions assigned to protonated n-butanol $MH^+$ at m/z 75 and the butyl cation $C_4H_9^+$ at m/z 57 showed relative intensities of 22% and 8%, respectively, consistent with the results of the previous experiment.

Upon increasing the collision energy to 10 eV, the relative intensities of the fragment ions at m/z 75 and m/z 57 increased to 32% and 19%, respectively, corresponding to enhancements by factors of approximately 1.3 and 2.3 compared to their values at 5 eV. Under these conditions, about 51% of the precursor ions undergo fragmentation, with a particularly pronounced increase in the formation of the ion at m/z 57.

When the collision energy was further increased to 15 eV, 53% of the precursor ions ($CH_3OH{\cdot}MH^+$) underwent fragmentation. The fragment ions at m/z 75 ($MH^+$) and m/z 57 ($M(-OH)^+$) were observed with relative intensities of 25% and 26%, respectively. The relative intensity of the ion at m/z 57 thus increased to 3.3 times its value at 5 eV, highlighting the enhanced formation of the butyl cation at higher collision energies. In addition, a further fragment ion at m/z 41 was observed with a relative intensity of approximately 2%.

A key insight from the experiments is that the efficiency of precursor ion fragmentation increases with rising pressure in the collision cell, primarily due to the increased frequency of ion-molecule collisions. However, a minimum dissociation energy threshold remains essential to initiate fragmentation. Under conditions of 15 eV applied energy and 0.5 mTorr CID gas pressure, approximately 53% of the precursor ions were fragmented. By contrast, at 5 eV and 3.0 mTorr pressure, the fragmentation efficiency reached 96%. These results highlight the interplay between pressure and energy in governing fragmentation processes, demonstrating that higher pressure can, to a large extent, compensate for lower collision energy to achieve substantial precursor-ion dissociation.

## 4.9 Background Signal of HPCI-MS System

In general, the analytical performance of an instrument depends not simply on how the signal intensity changes with the amount or concentration of analyte, but rather on the corresponding signal-to-noise ratio (S/N). In mass spectrometry, an elevated level of noise can be caused either by electronic perturbations, unwanted ions or even electronically excited species and photons impinging on the detector [89]. Unwanted ions can originate from impurities in the source or impurities in the gas or liquid supply that generate signals at the same m/z as the analyte. These effects can complicate data interpretation, interfere with analyte signals and reduce the overall sensitivity of the system. Understanding and mitigating the effects of noise is critical for the limit of detection (LOD) and sensitivity, particularly in the analysis of atmospheric samples. The subsequent experiment has been conducted to assess the origins and implications of background noise in HPCI-MS.

### 4.9.1 Background Signal of Blank Sample

An experiment has been performed to analyze a 12.6 ppmV toluene in synthetic air mixture, with synthetic air as a blank sample. The investigated ion for the analyte and blank samples was protonated toluene at m/z 93. Data have been recorded in full scan and profile mode. The corresponding single ion chromatogram (93 ± 0.2 m/z) is plotted on a logarithmic scale on the y-axis in *Figure 4.52*. The analyte was added between 0 and 9 min and the blank sample between 9 and 15 minutes, respectively.

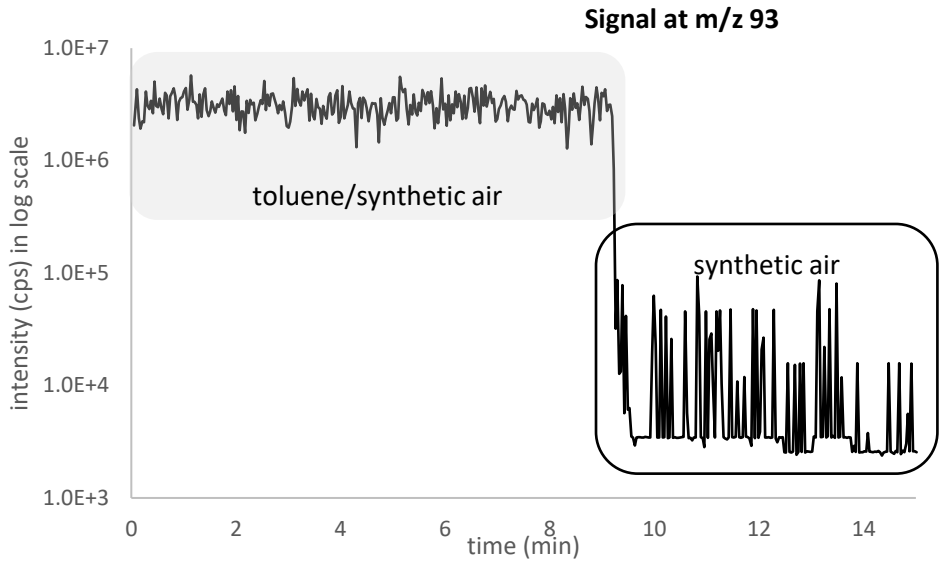


*Figure 4.52: Chromatogram at m/z 93 of toluene ($MH^+$) and blank signal of synthetic air.*

It is observed that the signal of the blank sample shows notable fluctuations. The average absolute background signal is $1.1 \pm 1.7 \times 10^4$ cps. However, this fluctuation was not observed in the analyte signal because of the much higher ion intensity. Such fluctuations can adversely affect the system stability and analytical performance. It is assumed that the noise signal arises from impurities in the blank sample, residual gas compounds or other sources within the system. The background signal fluctuation is observed independent of m/z and scan time. To investigate this effect, several experiments within the analyzer and detector region were performed.

*Block the ion transfer between Q1 and Q2*

To investigate the source of the fluctuation signal, ion transmission to Q2 was intentionally blocked using a non-conductive paper barrier placed between Q1 and Q2 (cf. *Figure 4.53 (b)*). Therefore, ions will not be transmitted to Q2 and, consequently, will not reach the detector of this system. The plasma gas and synthetic air have been continuously introduced into the system to generate ions as before. Under these conditions, the signal was recorded and is presented in the profile spectrum in *Figure 4.53 (a)*.

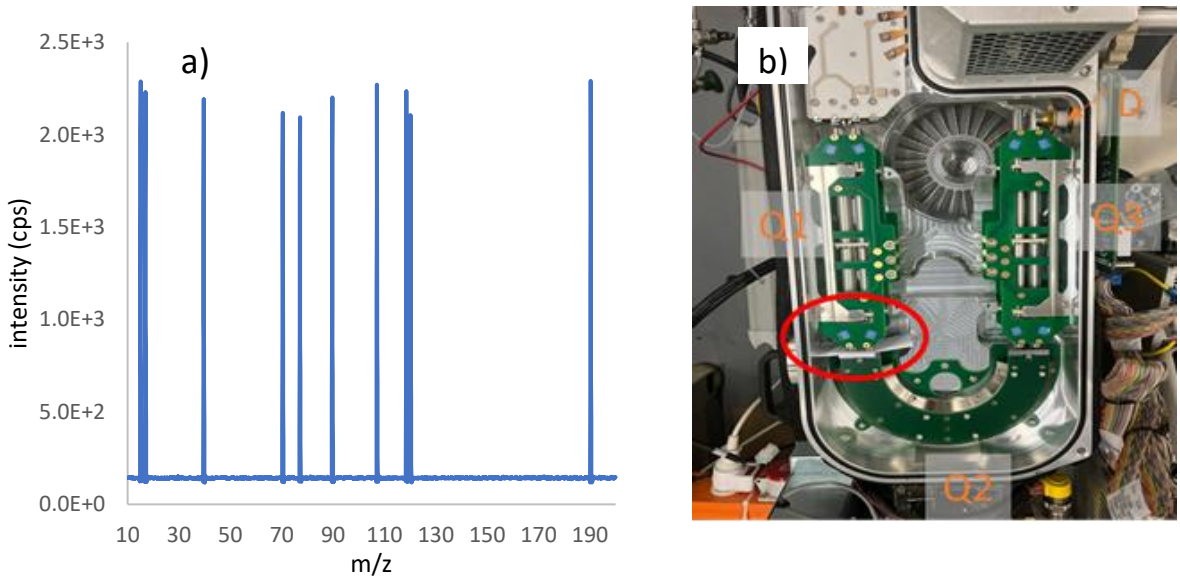


*Figure 4.53: Profile spectra of a synthetic air blank sample with blocked ion transmission between Q1 and Q2(a); Internal view of the analyzer chamber is shown in (b), and a non-conducting paper marked with a red circle is placed between Q1 and Q2 (b).*

Spikes are observed in the recorded profile spectrum (cf. *Figure 4.53 (a)*). As noted previously, these spikes are independent of m/z and occur randomly, which is also evident in this profile spectrum shown. However, their presence was unexpected, as ion transmission was assumed to be blocked (cf. *Figure 4.53 (b)*). It was further hypothesized that these extraneous signals might be transmitted directly from Q1 to Q3.

*Shield the Q3*

As described in the experimental section, the Q1 mass filter is configured to transmit ions within a user-defined mass range, while a vacuum pump removes the undesirable ions from the system. However, some of these undesired ions may not be completely removed and could still enter Q3. To address this, an aluminum foil with a thickness of 0.024 mm was employed as a protective shield for the Q3 mass filter (cf. *Figure 4.54*).

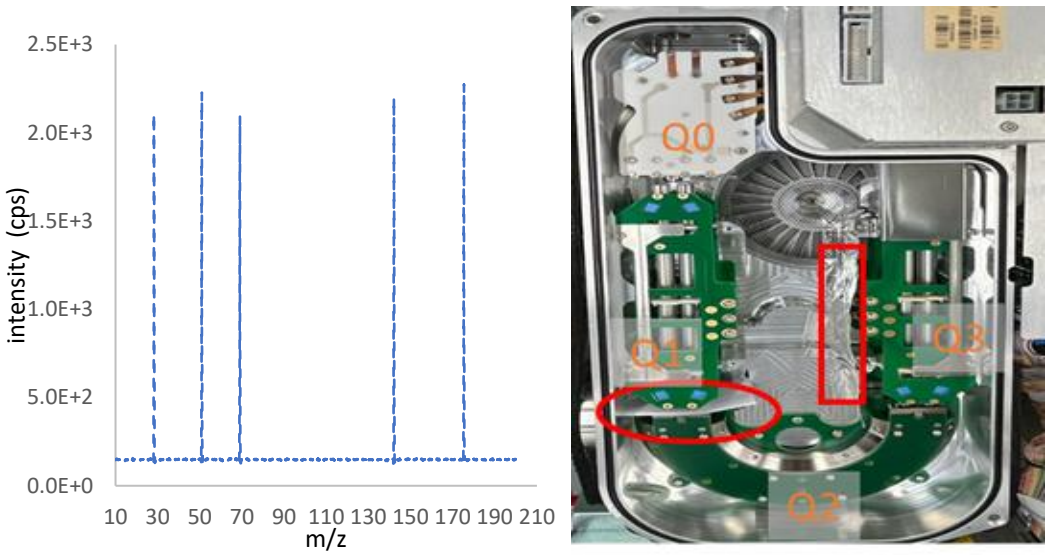


*Figure 4.54: Background profile spectrum of synthetic air with blocked Q1-Q2 transmission and protective Q3 shielding (left figure). The ion transmission is blocked (red circle) and shielded in front of the Q3 mass filter (right figure).*

In this experiment, the same sample and plasma gas flow as in the previous setup were used, but a protective shield was placed along the Q3 mass filter. Even under these conditions, spikes were still observed in the recorded profile spectra. However, their frequency was lower than when the ion transmission path was blocked without the shield. Thus, the spikes may originate from sources other than ions transmitted from Q1 and detected at the detector. To investigate this possibility, an additional experiment was conducted in which the detector was physically blocked.

*Blocked the Detector*

A small piece of paper was placed in front of the detector to prevent ions, photons, and metastable species from impinging on its surface. Under these conditions, the detector should not register any signal originating from the ion source or reaction chamber. Measurements were conducted in this configuration, and the corresponding profile spectrum is shown in *Figure 4.55*.

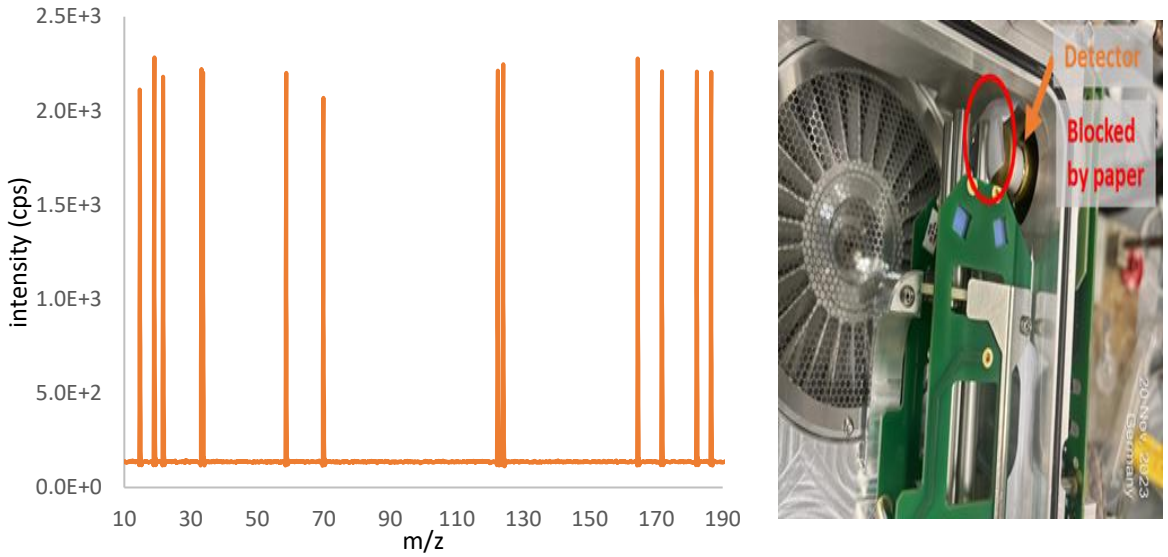


*Figure 4.55: The detector was blocked with non-conducting paper (right), and the corresponding recorded profile spectrum of synthetic air is shown on the left.*

Under these conditions, spikes were again observed, as in the previous experiment. Because the detector was blocked, no spikes were expected to be detected. However, the system still recorded signal spikes, indicating that these signals must originate from other sources. Consequently, a further experiment was conducted to investigate additional system components (e.g., the pressure gauge). Since the Q3 mass filter shield had been shown to reduce the frequency of spikes, it was left in place for this experiment.

### 4.9.2 Pressure Gauge Effects

As discussed in the experimental section, the MS system was initially a classical EI/CI source, which was later changed to an HPCI source. The ion source pressure is maintained at 2 to15 mbar,[8] which is slightly higher than the CI source. To observe the vacuum pressure of the MS system, a Pirani and a Penning pressure gauge have been integrated. The Pirani gauge was installed to measure the vacuum pressure of the ion source and lens chamber, while the Penning gauge was used to monitor the pressure in the mass analyzer section.

Initially, both pressure gauges were disconnected from the system, and a clear profile spectrum without any spike signal was recorded. It indicates that the spikes were generated from the pressure gauge. However, the HPCI source is required to check the pressure. Consequently, the Pirani pressure gage was installed, while the Penning pressure gage was decoupled from the system. Under these conditions, spikes were not observed, indicating that the unwanted signal originated from the Penning pressure gauge. This gauge was further installed in the system and its effect was checked by switching ON and OFF the power supply of this gauge.

*Figure 4.56* illustrates the spectral profiles under power-on and power-off conditions of the Penning pressure gauge, with the x-axis representing ion intensity and the y-axis denoting m/z values. The dotted blue line corresponds to the Penning gauge source 1 (PGS 1) in the ON state, while the solid orange line represents PGS 1 in the OFF state.

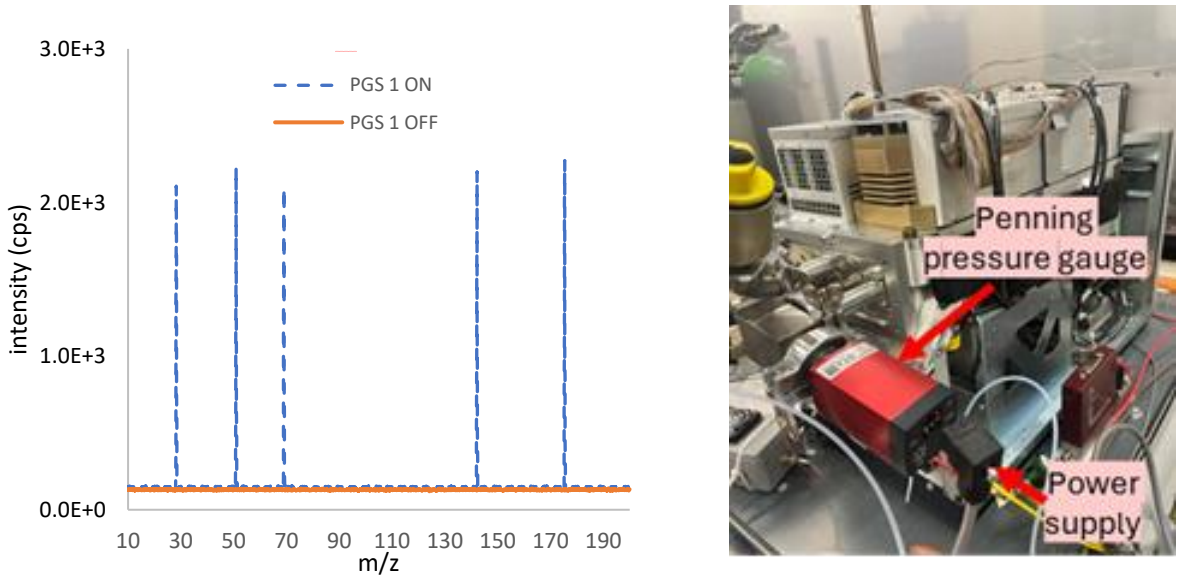


*Figure 4.56: BKG check dependence on Penning gauge (PGS1) power ON and OFF.*

The profile spectrum recorded with the Penning gauge (PGS 1) switched on exhibits pronounced spikes, whereas no such spikes are observed when the gauge is switched off. These data clearly demonstrate that the signal spikes are generated when the Penning gauge power supply is connected to the system.

The Penning gauge operates with a cold cathode at a high voltage of 3.0–4.5 kV, which, during operation, induces transient spikes that increase the background noise level.

In summary, the Pirani gauge has no detectable influence on the noise signal, while the Penning gauge produces substantial spikes that significantly elevate the system noise. To ensure accurate analyte measurements with the MS system, it is therefore essential to disconnect the Penning gauge power supply during MS operation.

### 4.9.3 Impact of Further Different Parameters on Background Signal

To evaluate the background signal, the power supply to the pressure gauge was disconnected during the measurements. In this section, the effects of the plasma gas and the analyte under both activated and deactivated HPCI source conditions are examined. All data were acquired in full-scan, profile mode; however, for each condition, only the single-ion chromatogram at m/z 107 is presented as an example, corresponding to the targeted molecular adduct ion of n-butanol.

*Plasma gas and analyte effect on the background signal under HPCI source-off conditions*

Prior to the introduction of the sample and the plasma gas into the MS system, the baseline vacuum conditions were established. The measured pressures within the ion source, lens chamber, and mass analyzer chamber were $1.7 \times 10^{-2}$ mbar, $5 \times 10^{-4}$ mbar, and $1.3 \times 10^{-6}$ mbar, respectively. The pressure in the analyzer chamber was measured using a Penning gauge; subsequently, the power supply to the gauge was disconnected during measurement. Under these conditions, characterized by the absence of both sample and plasma gas, and with the ion source turned off, mass spectra were recorded between m/z 10 and 200. The extracted single ion chromatogram at m/z 107 is shown in *Figure 4.57 (A)*.

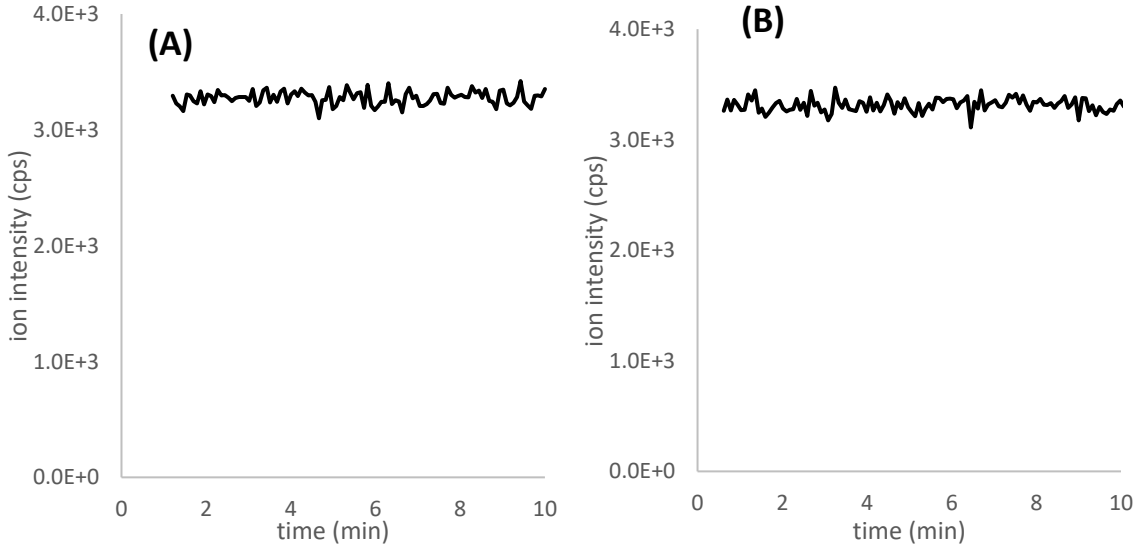


*Figure 4.57: Extracted single ion chromatogram at m/z 107 showing the background signal with sample but without plasma gas (A), and with plasma gas and sample (B). The power supply for the pressure gauge was disconnected, and the ion source was turned off.*

The plasma gas and analyte were sequentially introduced into the MS system. In both cases, the ion source was turned off. The recorded mass spectral signals in *Figure 4.57 (B)* were consistent with the background spectrum previously observed in the absence of both plasma gas and sample. The average signal is $3.3 \pm 0.1 \times 10^3$ cps for both spectra. This consistency indicates that the addition of these gases did not contribute to any significant change in ion intensity within the analyzed m/z range (m/z 10 – 200). This signal is attributed to the fact that the added gases remained in their neutral molecular states, as no ionization occurred under the ion source turned-off condition.

*HPCI source effect*

To investigate the influence of the HPCI source, only the $H_2$ plasma gas (7.0 sccm) was introduced into the ion source, while the sample line was closed by an end cap. Subsequently, spectra were recorded and the extracted single ion chromatogram of m/z 107 is shown in *Figure 4.58 (a)*. Subsequently, 3.0 sccm PG and synthetic air (4.0 sccm) was added as a sample to the system and the observed chromatogram is displayed in *Figure 4.58* (b).

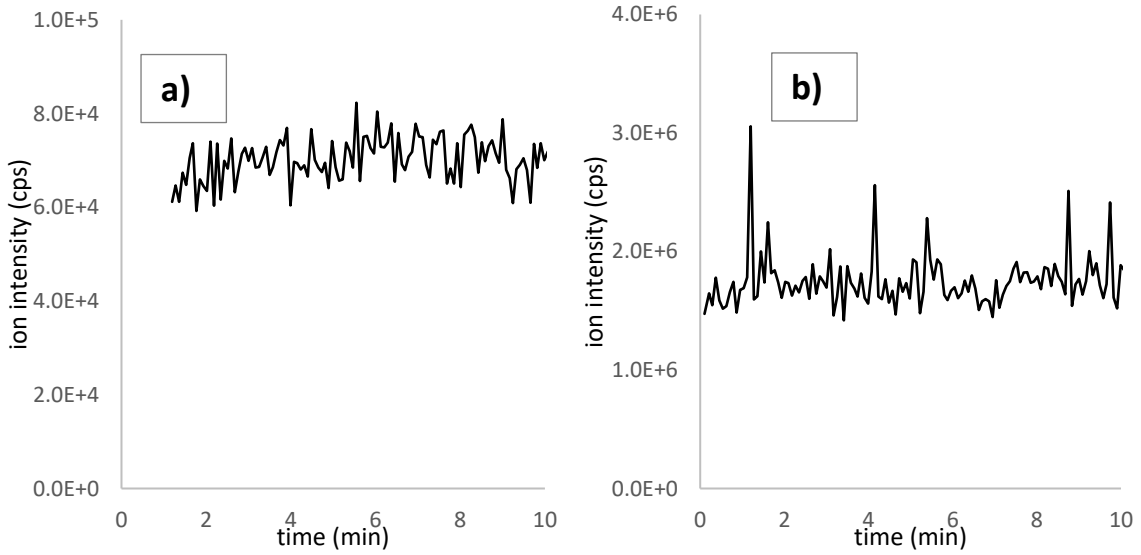


*Figure 4.58: Extracted single ion chromatogram of m/z 107 with 7 sccm $H_2$ plasma gas (a) and including synthetic air as sample (b).*

In figure (a) the data were recorded with only plasma gas added to the system and the plasma source turned on. The average intensity at m/z 107 was $6.8 \pm 0.1 \times 10^4$ cps. Subsequently, synthetic air was introduced as the sample into the reaction chamber. As a result, a strong elevation in background signal was observed, as shown in *Figure 4.58 (b)*. Under these

conditions, the average signal intensity was $1.7 \pm 0.2 \times 10^6$ cps. The presence of impurities in the sample may have contributed to an enhanced ion signal. These impurities are capable of reacting with the reactant species, potentially forming ions. Therefore, the signal was approximately 2 orders of magnitude higher than the background signal recorded in the absence of the sample.

It was hypothesized that the elevated noise in the signal was attributable to residual hydrogen impurities. To mitigate these impurities, the hydrogen gas was purified using a Bruker purifier. Subsequently, spectra were recorded with the plasma ion source turned on and off. The extracted single ion chromatogram of m/z 107 is presented in *Figure 4.59*.

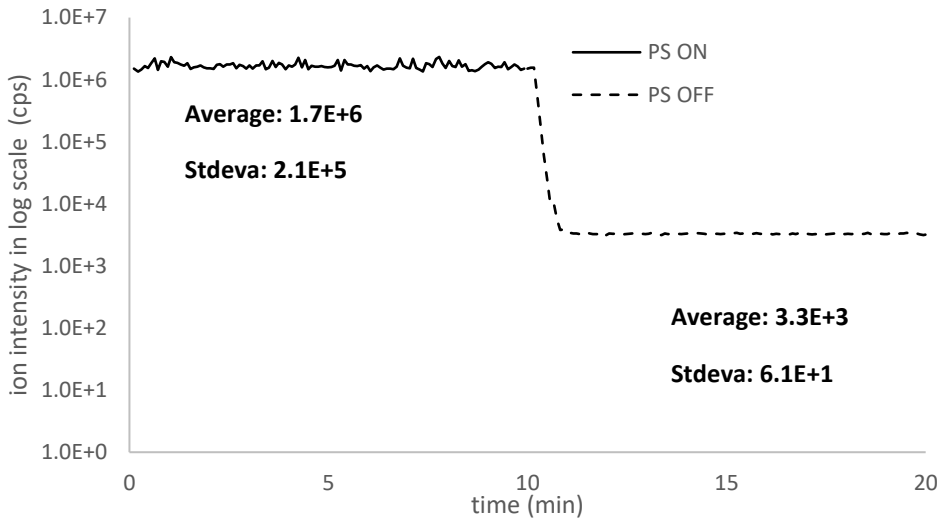


*Figure 4.59: Extracted single ion chromatogram at m/z 107, under plasma ON and OFF conditions, respectively.*

In this experiment, the background signal for synthetic air was the same as that without the purifier ($1.7 \pm 0.2 \times 10^6$ cps). Hence, the noise of this signal is independent of the purifier. To further evaluate the noise and LOD, an oxygenated compound, butanol, was employed in the analysis.

*Impact of dopant-assisted signal*

An experiment was conducted using high-purity liquid methanol as a dopant, combined with 0.5 sccm of synthetic air, to facilitate the detection of oxygenated compounds, such as butanol (M). Hydrogen gas at a flow rate of 3.0 sccm was introduced as the plasma gas, while 4.0 sccm of synthetic air, including the dopant, was added to the sample line, resulting in a total flow of 7.0 sccm into the system. This configuration yielded a system pressure of approximately 8.0 mbar. Full-scan profile data were acquired over a m/z range of 10 to 200, with the background signal at m/z 107 (corresponding to $CH_3OH{\cdot}MH^+$) specifically measured. The background signal ($3.4 \pm 0.1 \times 10^7$ cps) was estimated to be approximately 1 magnitude higher than the observed signal without the dopant.

In summary, the background noise can originate both from the electronics and from the analyte gases, and its level depends on the intensity of the background signal. The noise is typically estimated to be on the order of 10% of the background signal. The electronic noise alone is relatively low, for example about $\pm 0.1 \times 10^4$ cps for the Penning pressure gauge. However, upon introducing the mixing gas, the noise amplitude increases to approximately $\pm 0.2 \times 10^6$ cps, reflecting the higher background signal. Consequently, for high background signals, the overall noise is dominated by the background rather than by the electronic noise. During the measurements presented here, the Penning pressure gauge was disconnected and therefore did not contribute to the molecular analysis.

## 4.10 Analytical Performance

The analytical performance of HPCI mass spectrometry was evaluated with a particular emphasis on sensitivity and limit of detection (LOD). For this purpose, a series of VOCs was selected as target analytes, namely a BTX mixture in synthetic air (benzene, toluene, and xylene) and a set of alcohols (ethanol, isopropanol, and n-butanol). BTX analysis was conducted using $N_2/H_2$ as the reagent gas, and the signal intensities of the corresponding protonated ions ($MH^+$) were used for evaluation. Alcohols were analyzed using a $CH_3OH$/synthetic air mixture as the reagent gas, and the signal intensities of the methanol adduct ions ($M{\cdot}CH_3OH_2^+$) served as the performance metric. Data were acquired in two operational modes—full scan (FS) and selected ion monitoring (SIM)—each recorded in both profile and centroid formats. This configuration enabled a systematic comparison of the influence of acquisition mode and data type on analytical performance under optimized operating conditions.

### 4.10.1 Sensitivity

*BTX in synthetic air mixture*

To assess the analytical performance of the MS system, a BTX/synthetic air mixture was employed. Different mixing ratios were generated by diluting a standard BTX/synthetic air mixture containing approximately 10.5 ppmV benzene, 9.9 ppmV toluene, and 9.5 ppmV o-xylene with synthetic air using calibrated mass flow controllers. A plasma gas composed of 12% $N_2$ in $H_2$ was used. Profile data were acquired in FS mode, and the resulting calibration curves are shown in *Figure 4.60*. The x- and y-axes represent the mixing ratio in ppbV and the absolute signal intensity, respectively.

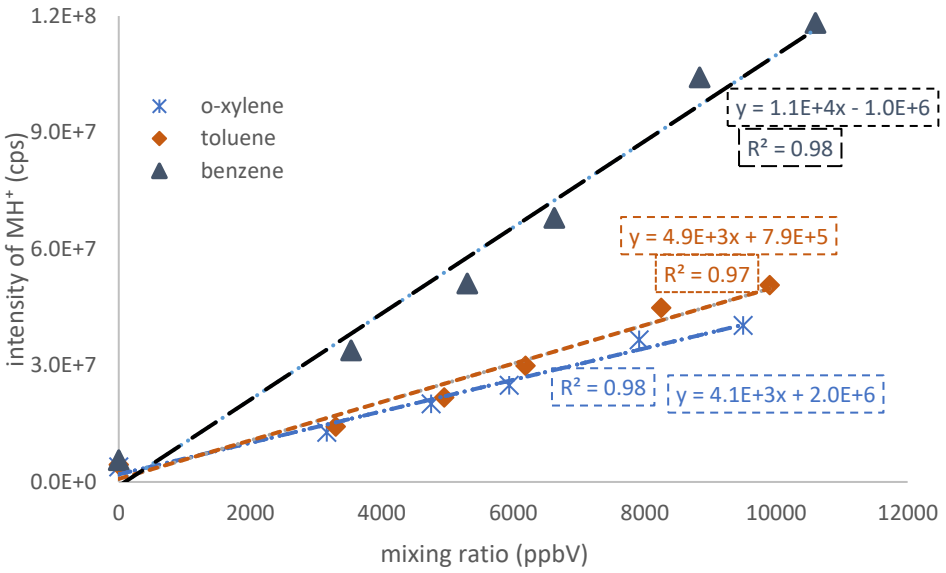


*Figure 4.60: Calibration curves of BTX based on the protonated molecular ion ($MH^+$) signal using $N_2/H_2$ as reagent gas. The profile data were recorded in FS mode.*

In the previous experiment (cf. *section 4.7.1),* BTX compounds were ionized to yield $MH^+$, $M^+$, $M(-H)^+$, and $M(-CH_3)^+$ ions. Among these, the $MH^+$ (at m/ 79, 93 and 107 for protonated benzene, toluene and o-xylene, respectively) ion was selected for sensitivity evaluation due to its highest signal intensity. The ion signal intensities increase linearly with the BTX mixing ratio, as evidenced by the coefficients of determination ($R^2$) of 0.98 for benzene, 0.97 for toluene, and 0.98 for o-xylene obtained from linear regression. The corresponding regression equations are shown in *Figure 4.60*. The slope of each regression line was taken as a measure of analyte sensitivity and is reported in units of cps/ppbV.

Additionally, sensitivity was evaluated under different data acquisition modes. In full-scan mode using centroid data, sensitivities between $0.4 \times 10^3$ to $1.1 \times 10^3$ cps/ppbV were obtained for the BTX compounds, with benzene exhibiting the highest sensitivity among the analytes investigated. Further experiments were carried out to compare the sensitivity obtained with different acquisition modes and data types, specifically FS and SIM modes, using either profile or centroid data. The corresponding sensitivities are summarized in *Table 4.*

*Table 4: Sensitivity assessment (cps/ppbV) of benzene, toluene, and o-xylene in different measurement modes.*

| | | **Sensitivity (cps/ppbV) ($\times 10^3$)** | | |
|---|---|---|---|---|
| ***Scan mode*** | ***Data type*** | ***benzene*** | ***toluene*** | ***o-xylene*** |
| FS | Profile | $11.0 \pm 1.0$ | $4.9 \pm 1.0$ | $4.1 \pm 1.0$ |
| FS | Centroid | 1.1 ± 0.1 | 0.7 ± 0.1 | 0.4 ± 0.1 |
| SIM | Profile | 240 ± 2 | 121 ± 3 | 78 ± 6 |
| SIM | centroid | 1.3 ± 0.1 | 0.7 ± 0.1 | 0.4 ± 0.1 |

The results show that profile data acquired in SIM mode are approximately twenty times more sensitive than those obtained in FS mode. This enhanced sensitivity in SIM mode is attributed to its targeted monitoring of specific m/z values of $MH^+$, namely m/z 79 for benzene, m/z 93 for toluene, and m/z 107 for o-xylene.

*Ethanol in synthetic air mixture*

In the following experiment, a 90 ppmV ethanol/SA mixture was used to evaluate sensitivity. Different ethanol mixing ratios were prepared by diluting this stock mixture with synthetic air using calibrated mass flow controllers. $H_2$ was employed as the plasma gas, and a 1% methanol/SA mixture was introduced into the sample line as a dopant to generate the $CH_3OH_2^+$ reagent ion. Ethanol/synthetic air mixtures at various mixing ratios were then introduced into the system, and profile data were acquired in full-scan mode. The analytical signal was evaluated for the ethanol–methanol adduct ion $CH_3OH{\cdot}C_2H_5OH_2^+$ at m/z 79. The resulting calibration curves are shown in *Figure 4.61*, where the x-axis represents the ethanol mixing ratio in ppbV and the y-axis the absolute signal intensity in cps.

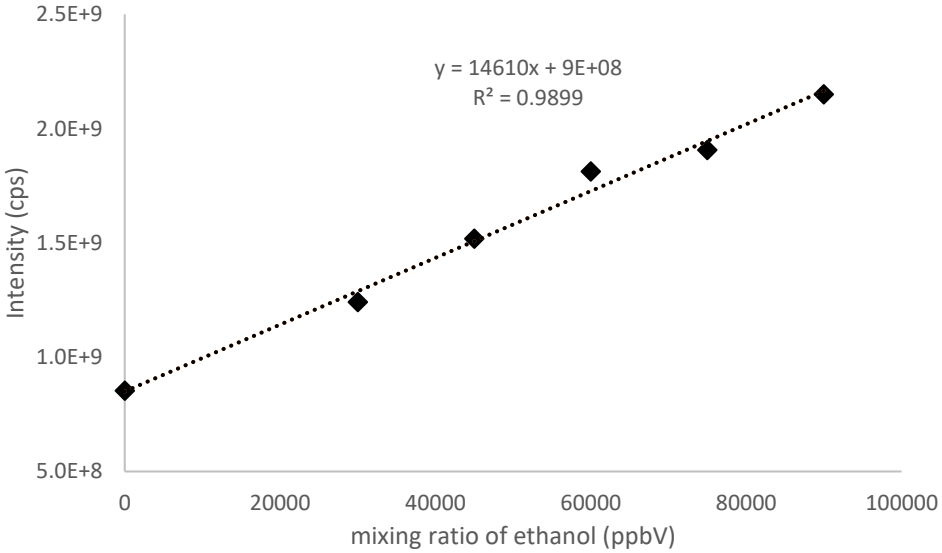


*Figure 4.61: Calibration curves of ethanol as the analyte with 1% methanol in synthetic air as the reagent gas.*

The calibration curves for m/z 79 exhibited good linearity, as demonstrated by the coefficient of determination ($R^2$) values of 0.9899. This $R^2$ value indicates an excellent fit of the experimental data to a linear regression model across the tested mixing ratios, confirming the quantitative analysis of ethanol compounds. The system's sensitivity $(1.5 \pm 0.1) \times 10^4$ cps/ppbV was quantified as the slope of the calibration curve. Based on these findings, the analytical signal is therefore evaluated using the ethanol–methanol adduct ion, $CH_3OH{\cdot}C_2H_5OH_2^+$, at m/z 79.

It is observed that the intercept in the linear equation shows ($9 \times 10^8$) cps. This intercept can be explained by the overlaying methanol cluster ($(CH_3OH)_3H^+$-$H_2O$) from the reagent gas at m/z 79 as explained in detail in *section 4.7.3*.

*Iso-propanol in synthetic air and n-butanol in synthetic air mixture*

Furthermore, isopropanol and n-butanol at mixing ratios of 1.4 and 14.0 ppmV, respectively, were investigated using full-scan acquisition in profile mode. The corresponding methanol adduct ions, $CH_3OH{\cdot}C_3H_7OH_2^+$ for isopropanol and $CH_3OH{\cdot}C_4H_9OH_2^+$ for n-butanol, were monitored at m/z 93 and 107, respectively. The resulting sensitivities were determined to be $(1.8 \pm 0.5) \times 10^4$, and $(2.5 \pm 0.1) \times 10^4$ cps/ppbV.

However, as demonstrated for the BTX analysis (*cf. Table 4*), SIM mode is approximately twenty times more sensitive than the full-scan mode. Consequently, the sensitivity of n-butanol was determined using SIM mode and found to be $(58 \pm 3) \times 10^4$ cps/ppbV, which is likewise about twenty times higher than in FS mode. These findings support the use of SIM mode with profile data for quantitative analysis.

### 4.10.2 Limits of Detection (LODs)

The limit of detection (LOD) is commonly defined as the lowest analyte concentration (or mixing ratio) that can be reliably distinguished from the background. It is determined from replicate measurements of the background signal obtained using a blank sample. The noise in this background signal is quantified by its standard deviation σ and used in the LOD calculation. Assuming a normal distribution, approximately 99.7% of data points lie within 3σ of the mean. Accordingly, a factor t = 3 was chosen to ensure a high confidence level. The LOD was calculated using the following expression:

$$\text{LOD} = t \times \sigma \quad (8)$$

At a threshold of LOD = 3σ, the analyte signal can be distinguished from the background with a detection probability of approximately 50%. This approach was applied consistently across all experiments to determine the LOD values for benzene, toluene, xylene (BTX), and the investigated alcohols.

*LODs for BTX with $N_2/H_2$ reagent gas*

The LODs for the BTX analytes were determined under optimized system conditions using $N_2/H_2$ as the reagent gas. Both profile and centroid data were acquired in SIM and FS modes. Initially, measurements were carried out in SIM mode with centroid data, monitoring the protonated ions at m/z 79, 93, and 107 for benzene, toluene, and o-xylene, respectively. Under these conditions, the calculated LODs for BTX were in the range of 3–7 ppbV.

Subsequently, additional measurements were performed using the different acquisition modes and data types, and the corresponding LOD values are summarized in *Table 5*. Notably, the LODs obtained in SIM mode were approximately 70-fold lower than those measured in FS mode (cf. profile data in *Table 5*).

*Table 5: LOD (ppbV) of benzene, toluene, and o-xylene on different measurement modes.*

| Scan mode | Data type | benzene | toluene | o-xylene |
|---|---|---|---|---|
| **FS** | Profile | 274 ± 22 | 418 ± 13 | 332 ± 19 |
| **FS** | Centroid | 169 ± 22 | 125 ± 3 | 209 ± 14 |
| **SIM** | Profile | 4 ± 0.1 | 8 ± 0.1 | 5 ± 0.1 |
| **SIM** | centroid | 3 ± 0.2 | 7 ± 0.2 | 4 ± 0.2 |

*LODs for alcohols with methanol/synthetic air as the reagent gas*

Experiments were carried out to determine the LOD for ethanol, propanol, and butanol in synthetic air using a methanol/synthetic air reagent gas. Noise was evaluated at m/z 79, 93, and 107, corresponding to the methanol adduct ions of ethanol, propanol, and butanol, respectively. In FS mode profile data, the LODs for ethanol, isopropanol, and n-butanol were found to be approximately 13 ppmV, 101 ppbV, and 106 ppbV, respectively. The comparatively high LOD for ethanol (in the ppmV range) is attributed to spectral interference at m/z 79, where an additional methanol-derived ion, ($(CH_3OH)_3H^+$-$H_2O$), may also be formed.

In previous experiments with BTX/synthetic air mixtures, LOD measurements in different acquisition modes showed that the LOD in SIM mode can be lower than in FS mode. Therefore, n-butanol was evaluated as an example for alcohol in SIM mode, yielding an LOD of approximately 4 ppbV, which is about 64 times lower than the LOD obtained in FS mode. These results are consistent with earlier findings and confirm the substantial improvement in detection sensitivity achieved in SIM mode compared to FS mode.

In summary, the choice of acquisition mode and data type has a pronounced impact on the analytical performance of the system. For example, LOD values obtained in SIM mode (e.g., 3 ppbV for benzene, 7 ppbV for toluene and 4 ppbV for o-xylene using centroid data) were substantially lower than those measured in FS mode (274 ppbV for benzene, 418 ppbV for toluene and 332 ppbV for o-xylene using profile data), highlighting the enhanced sensitivity of SIM due to its targeted ion monitoring. In addition, the use of centroid data in SIM mode reduces noise contributions and thereby improves the signal-to-noise ratio relative to profile data. These findings emphasize the importance of selecting the acquisition strategy in line with the analytical objective: SIM mode with centroid data is optimal for achieving low LODs in quantitative BTX analysis, whereas FS mode with profile data is more suitable for qualitative characterization and improved selectivity in complex mixtures.

## 4.11 Different Plasma Glass Tube

The HPCI source configuration used in this study consists of a helical RF resonator integrated with a cylindrical glass tube, referred to as tube-1 (cf. *Figure 3.1*). The resonator is mounted around tube-1, and both components are aligned along a horizontal axis. The plasma gas is introduced at one end of tube-1, while the opposite end is directly coupled to the reaction chamber.

However, the original configuration of tube-1 presents a significant experimental limitation. Specifically, the axial geometry permits the transmission of plasma fluorescence, from the discharge region directly into the reaction chamber. This fluorescence enables the photoionization of neutral molecules present within the reaction chamber, leading to the unintended formation of molecular cations ($M^+$) along with undesired ions such as $O_2^+$. The generation of such ions via photoionization introduces an undesired background signal, which complicates the accurate interpretation of ion-molecule reaction mechanisms, particularly those involving proton transfer processes.

To mitigate this issue, the HPCI glass tube was redesigned to attenuate or eliminate the impact of plasma fluorescence. Two additional glass tubes were developed and incorporated into a modified geometry. These redesigned configurations should substantially reduce the influence of plasma fluorescence on the reaction chamber. Consequently, all subsequent experiments were carried out using these newly designed plasma glass tubes.

### 4.11.1 Design of Glass Tube-2

In this section, a newly designed glass tube, referred to as glass tube-2, was used, as illustrated in *Figure 4.62*. This tube retains the same axial geometry as tube-1 and incorporates two additional inlets, labeled A and B. Inlets A and C can be used either for pressure measurements inside the plasma source or as sample gas inlets, whereas inlet B is used to connect the helical resonator of the HPCI source.

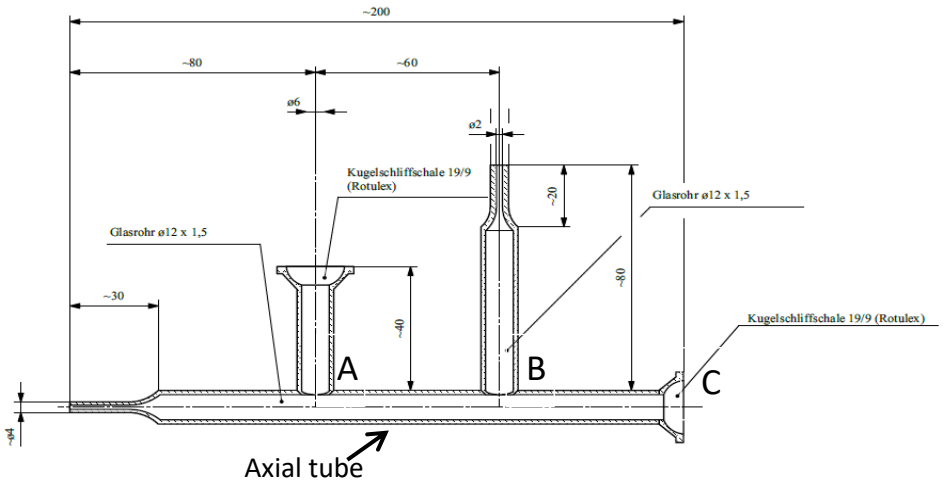


*Figure 4.62: Schematic of the glass tube-2 configuration for the plasma ion source.*

In this design, the helical resonator is mounted perpendicular to the axial tube at a distance of 140 mm from the end of the tube connected to the reaction chamber. The plasma source distance (PSD), defined as the distance from the center of the helical resonator to the end of the glass tube, is 170 mm. As a result, plasma fluorescence should not propagate directly into the reaction chamber, thereby reducing photoionization effects.

The design provides two alternative sampling inlets for analyte introduction. The first sampling inlet, A, is located adjacent to the HPCI source, approximately 80 mm from the end of the tube connected to the reaction chamber. This position affords a longer reaction time between analyte molecules and plasma ions, potentially enhancing ionization efficiency. As described in *section 4.7.1*, the reaction time of 82 ms was previously calculated from the reaction chamber length (10 mm) and the total gas flow velocity of 12.1 $cm \cdot s^{-1}$. In the new configuration, an additional reaction volume is introduced within the axial tube, with a length of 80 mm and an inner diameter of 10 mm. At the same gas flow velocity (12.1 $cm \cdot s^{-1}$), the overall reaction time increases to 740 ms.

The second sampling inlet C is located at the end of the tube, approximately 200 mm from the end of the tube connected to the reaction chamber. Since the sample is added through a 0.25 mm capillary tube, it is possible to adjust the capillary tube through inlet C to the axial tube. As a result, the reaction time of the ion-molecule reaction can be adjusted by changing the capillary position.

A schematic of the glass tube-2 configuration is shown in *Figure 4.63*. In this setup, an $N_2/H_2$ mixture at a flow rate of 3.0 sccm was introduced through inlet B as the plasma gas, and the HPCI source pressure was monitored at inlet A (denoted as P3). An analyte gas flow of 4.0 sccm (toluene in synthetic air (SA), or alternatively $N_2$) was introduced via sample inlet-1, while sample inlet-2 (inlet C) was sealed with an end cap. Under these gas-flow conditions, the HPCI source pressure measured at inlet A was 8.0 mbar. Profile spectra for toluene/SA (blue trace) and $N_2$ (orange trace) were subsequently recorded, as shown in *Figure 4.63*. The x-axis represents m/z, and the y-axis represents relative intensity; the m/z range 70–110 is displayed in an enlarged view on the y-axis.

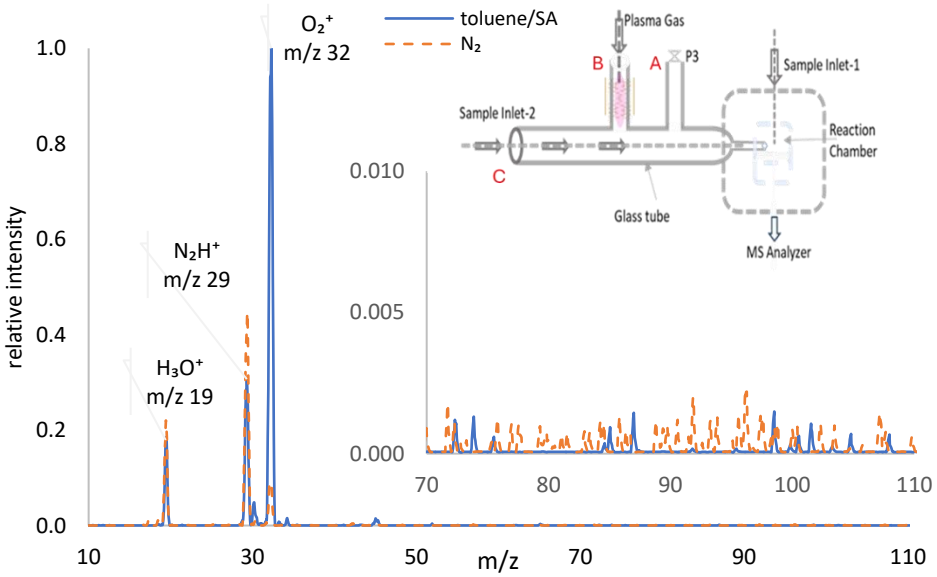


*Figure 4.63: Profile spectra of $N_2$ (orange line) and toluene/SA (blue line) recorded with the glass tube-2 configuration.*

In this figure, signals at m/z 19, 29, and 32, corresponding to $H_3O^+$, $N_2H^+$, and $O_2^+$, respectively, are observed for the toluene/synthetic air mixture (blue trace, toluene/SA in *Figure 4.63*). These ions were also detected when the system was operated with plasma glass tube-1 (cf. *section 4.1.4*). In the present experiment, the ion abundances of $N_2H^+$ and $O_2^+$ were measured to be $(1.1 \pm 0.1) \times 10^8$ and $(4.1 \pm 0.2) \times 10^8$ cps, respectively. For comparison, when $N_2$ was introduced as the analyte gas, the ion abundances of $N_2H^+$ and $O_2^+$ were $(1.6 \pm 0.2) \times 10^8$ and $(0.3 \pm 0.1) \times 10^8$ cps, respectively.

The ion count of $N_2H^+$ increased by approximately 45% when $N_2$ was introduced, compared to the signal obtained with the toluene/SA analyte. However, this abundance is about three orders of magnitude lower than that measured with the glass tube-1 configuration ($(3840 \pm 20) \times 10^8$ cps) at 8.0 mbar PS pressure and a plasma ion source distance of 100 mm (cf. *section 4.1.4*). This reduction is likely due to losses of $N_2H^+$ during transport toward the reaction chamber. In the present configuration (tube-2), ions generated in the HPCI source must travel approximately 170 mm before entering the reaction chamber, which likely leads to substantial ion loss through collisions with the glass tube walls. Consistent with this interpretation, previous measurements with glass tube-1 (cf. *section 4.2*) showed that $N_2H^+$ losses increased with plasma ion source distance, reaching up to 90% when the ion source was positioned 20 mm farther from its initial location.

The ion counts of $O_2^+$ at m/z 32 were reduced by 93% when $N_2$ was added compared to the signal of toluene in synthetic air. In this case, the $O_2$ molecules were absent from the reaction chamber because $N_2$ was added to the system.

When toluene in synthetic air was introduced into the system, the $N_2H^+$ and $O_2^+$ ions were expected to react with toluene to form $MH^+$ and $M^+$ ions. However, no corresponding analyte ion peaks were observed. The spectrum was therefore inspected in the m/z range 70–110 (cf. *Figure 4.63*). From a kinetic standpoint, the concentration of reactant ions appears to be too low, and the ion–molecule reaction time in the reaction chamber is likely too short to generate detectable analyte ion signals. To increase the reaction time, sample inlet-2 was used instead of inlet-1, and the sample was introduced via a 0.25 mm capillary. The position of the capillary along tube-2 was systematically varied, but even under these conditions the toluene ion peaks remained undetectable.

Since the analyte ion could not be observed using glass tube-2, a third glass tube (tube-3) with a reduced HPCI source distance was employed, with the expectation that reactant ion losses would be diminished.

## 4.11.2 Design of Glass Tube-3

A third tube configuration, referred to as *glass tube-3*, was fabricated based on the design of *glass tube-2*, with the primary modification being a repositioning of the HPCI source, as shown in *Figure 4.64*. In this design, the HPCI source is mounted 60 mm closer to the reaction chamber than in *Glass Tube-2*. Due to the new configuration of tube-3, the positions of the HPCI source and the pressure gauge were interchanged (from inlet B to A and from inlet A to B, respectively). As a result, reactant ions generated in the HPCI source experience reduced transport losses due to the shorter travel distance.

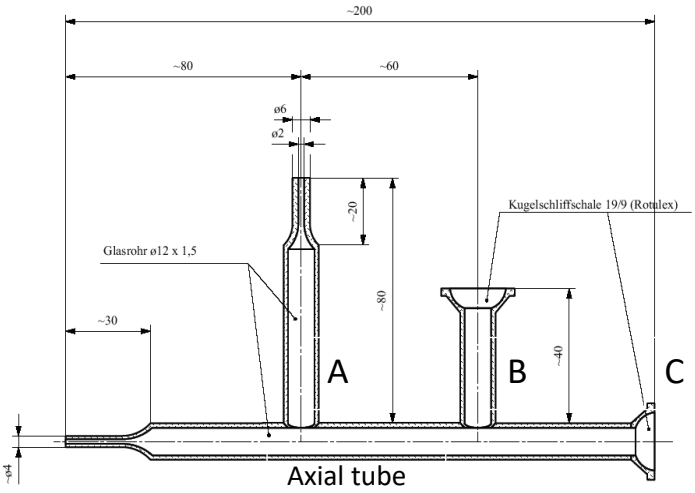


*Figure 4.64: Schematic of the glass tube-3 for the plasma ion source.*

This tube was connected to the system, and analyte gas and plasma gas were supplied at the same flow rates as in the previous experiment with tube-2. The analyte gas was introduced via sample inlet-1, while sample inlet-2 (position C) was sealed with an end cap. Accordingly, the pressure of the plasma source, measured at inlet position B, was also 8.0 mbar. Two profile spectra for toluene in synthetic air (blue trace) and in $N_2$ (orange trace) were then recorded, as shown in the lower panel of *Figure 4.65*. The m/z range 70–110 is displayed with an expanded y-axis.

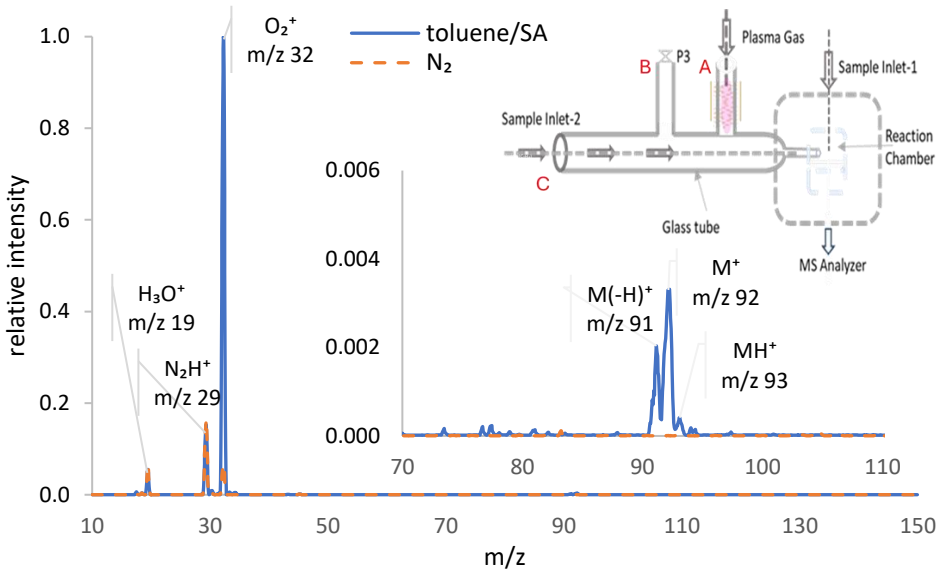


*Figure 4.65: Analysis of toluene in synthetic air using glass tube-3. Schematic of the MS system with tube-3 installed, and mass spectra of toluene in synthetic air and in $N_2$ over the m/z range 10–150. An expanded view of the m/z 70–110 region highlights the toluene molecular ion peaks.*

In these profile spectra, the ions at m/z 19, 29, and 32 originate from the plasma gas and the toluene carrier gas, whereas the ions at m/z 91, 92, and 93 are assigned to toluene-related species.

Upon introduction of the toluene analyte, the $O_2^+$ ion at m/z 32 exhibited the highest intensity, owing to the use of synthetic air as the mixing gas. Its abundance was $(91 \pm 2) \times 10^8$ cps, representing a 22.2-fold increase compared with glass tube-2. Furthermore, the $N_2/H_2$ plasma gas supplied to the HPCI source led to the formation of the reactant ion $N_2H^+$, with an abundance of $(14 \pm 0.6) \times 10^8$ cps.

As discussed previously (cf. *section 4.7.1*), the $N_2H^+$ and $O_2^+$ ions can undergo ion–molecule reactions with neutral toluene (M), leading to the expected formation of $MH^+$, $M^+$ and $M(-H)^+$. However, the $MH^+$ ion at m/z 93 appears only as a minor peak in *Figure 4.65*. From a kinetic perspective, this can be attributed to the comparatively low concentration of the $N_2H^+$ reactant ion. In contrast, the molecular ions M+ and $(M–H)^+$ are observed with relatively higher amount in *Figure 4.65*. Among these, $M^+$ is formed predominantly via reaction with $O_2^+$, although both $M^+$ and $M(-H)^+$ can also be generated by photoionization (cf. *Section 4.7.1*).

As mentioned previously, in the original setup the $O_2^+$ and toluene molecular ions were predominantly generated in the reaction chamber via photoionization, suggesting that plasma fluorescence may also enter the chamber in the present configuration. Based on the design of plasma *glass tube-3*, such fluorescence would not be expected to reach the reaction chamber, as the HPCI source is mounted perpendicular to the axial tube. However, the experimental results indicate that a fraction of the plasma fluorescence does, in fact, propagate along the axial glass tube and is in line of sight with the reaction chamber, as evidenced in *Figure 4.66*.

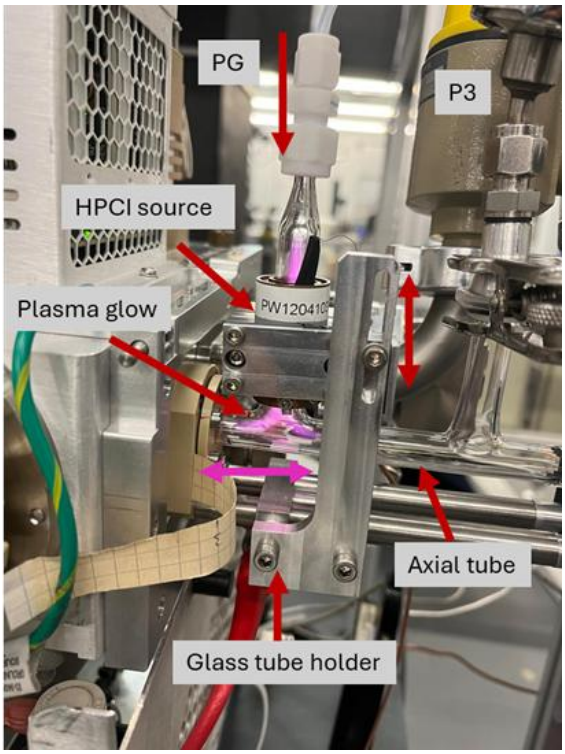


*Figure 4.66: Picture of the new glass tube-3 configuration with the HPCI source installed perpendicularly to the axial tube. The plasma glow extends into the axial tube and is in line of sight with the reaction chamber inside the instrument.*

Because plasma fluorescence propagates into the reaction chamber, one possible mitigation strategy is to increase the distance between the HPCI source and the axial glass tube. Within the current design constraints, this distance can be extended by approximately 25 mm. However, the effective plasma glow length is about 40 mm, implying that even with a 25 mm increase, fluorescence can still reach and influence the reaction chamber. Thus, increasing this distance is expected to substantially reduce photoionization effects and consequently decrease the formation of $O_2^+$ and $M^+$ ions. At the same time, a larger separation between the HPCI

source and the reaction chamber would increase wall losses of the reactant ion $N_2H^+$, potentially lowering the abundance of the protonated analyte ion $MH^+$ in the reaction chamber.

Subsequently, sample inlet-2 was employed instead of inlet-1 in order to increase the effective length of the reaction volume. To achieve this, the analyte was introduced through inlet-2 via a 0.25 mm inner diameter capillary tube, and the position of the capillary tip was systematically adjusted to different locations along tube-2. The selected distances between the capillary tip and the reaction chamber aperture were 10, 15, 20, and 40 mm. As a result of this configuration, molecular ion peaks of toluene were detected, as shown in the upper *Figure 4.67*. The y-axis of the upper figure represents the relative intensity (%), normalized to the reactant ion, while the x-axis shows the m/z values. The corresponding molecular ion intensities (y-axis) are plotted as a function of the length of the reaction volume, expressed in mm (x-axis), in the lower *Figure 4.67*.

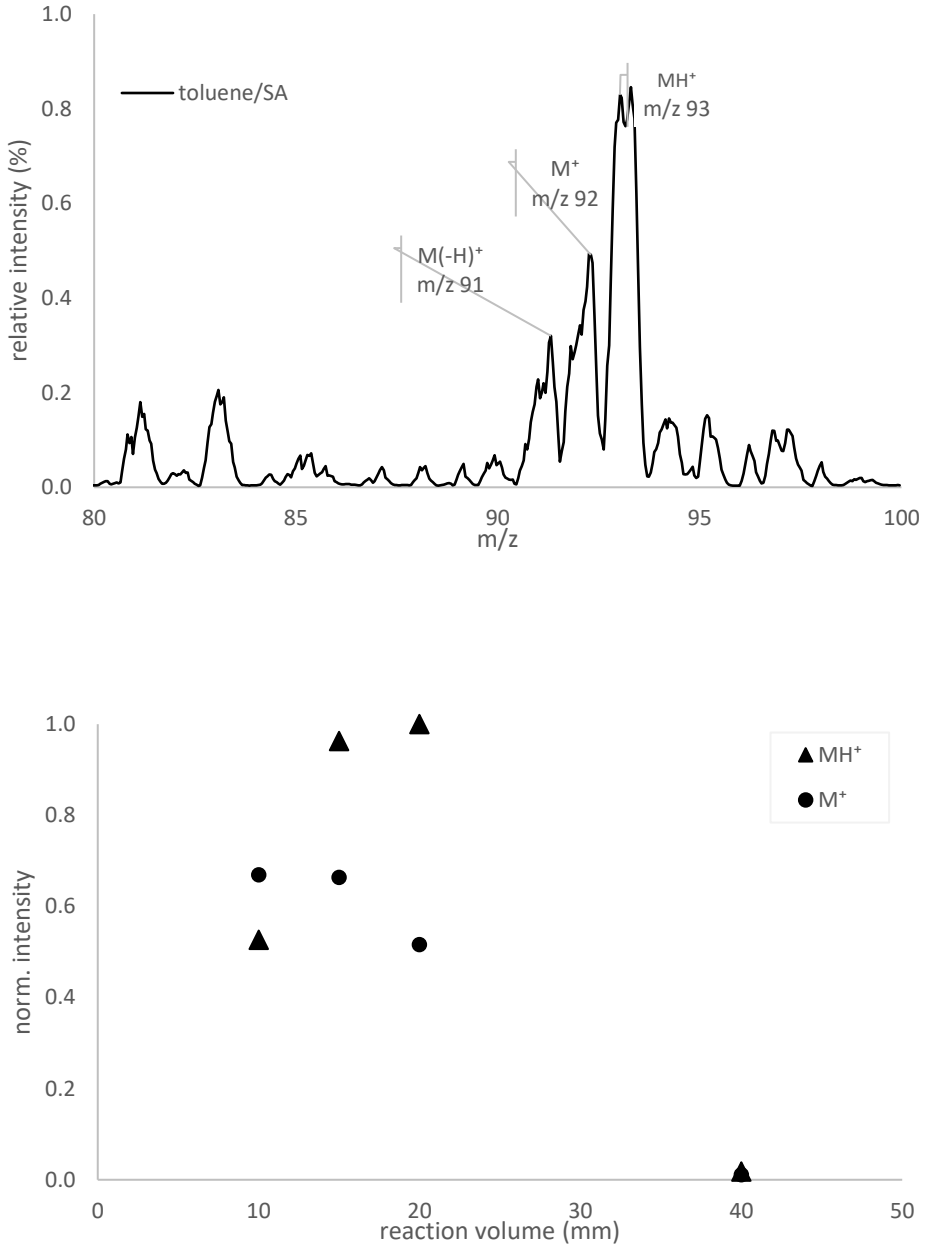


*Figure 4.67: Analysis of toluene molecules using the new glass tube 3. Upper panel: profile spectrum of toluene at a reaction length of 20 mm. Lower panel: dependence of the signal intensities of $M^+$ and $MH^+$ on reaction length (in mm).*

The profile mass spectrum of toluene/SA (shown in the upper panel of *Figure 4.67*) was recorded at a reaction chamber length of 20 mm. This spectrum exhibits the molecular ions $M(-H)^+$, $M^+$, and $MH^+$. However, only the intensities of the $M^+$ and $MH^+$ ions were evaluated as a function of the length of the reaction volume, and these results are presented in the lower panel of *Figure 4.67*.

As shown in the figure, the intensity of the protonated molecular ion ($MH^+$) increases with the length of the reaction volume up to 20 mm. At a length of 40 mm, however, a pronounced decrease in ion intensity is observed. This reduction can be attributed to the geometry of the glass tube. Specifically, the 30 mm of the glass tube has an ID of 4 mm, which then expands to 12 mm toward the HPCI source (cf. *Figure 4.64*). When the analyte is introduced into the 4 mm diameter section, ions are transported more efficiently toward the analyzer due to the reduced ID of the glass tube.

In contrast, previous experiments have demonstrated that ion losses increase with longer transport distances in the glass tube, as ions must traverse a greater path length before reaching the analyzer. Consequently, the maximum $MH^+$ intensity is observed at the length of the reaction volume of 20 mm, with a measured value of $(2.5 \pm 0.5) \times 10^7$ cps. At 10, 15 and 20 mm lengths, ion intensities in the range of $(1.3\ to\ 2.5) \times 10^7$ cps are recorded. Nevertheless, a significantly higher $MH^+$ ion intensity of $(64 \pm 3) \times 10^7$ cps was obtained at a reaction length of 10 mm using glass tube-1 (cf. *section 4.7.1*), which is approximately 20 times larger than that measured at 20 mm using glass tube-3.

In contrast, the intensity of the molecular ion $M^+$ remains relatively constant at $(1.3\ to\ 1.7) \times 10^7$ cps for reaction lengths 10, 15, and 20 mm (cf. lower panel of *Figure 4.67*). However, this intensity is lower than the $MH^+$, except at a reaction length of 10 mm. The $MH^+/M^+$ ratios are 0.8, 1.5, and 1.9 for reaction lengths of 10, 15, and 20 mm, respectively. For comparison, at a reaction length of 10 mm using glass tube-1, a ratio of 0.9 was obtained for toluene in a BTX–synthetic air mixture at 8 mbar (cf. *section 4.7.1*). Since $M^+$ is formed predominantly by photoionization, the increase in the $MH^+/M^+$ ratio when using glass tube-3 can be attributed to reduced photoionization and an increased reaction volume.

In summary, in the newly fabricated glass tube designs the HPCI source was positioned at 90° relative to the axial glass tube. As a result, the generated ions traverse a curved transfer path before entering the reaction chamber. Although substantial amounts of reactant ions are likely produced within the HPCI source, significant ion losses probably occur during transport through this curved configuration, leading to a reduced yield of protonated molecular ions. For this reason, the glass tube-1 configuration was reinstalled, which provided more efficient ionization.

# 5 Summary and Conclusion

This work has focused on the development, optimization, and analytical characterization of a hydrogen plasma-driven chemical ionization (HPCI) source integrated into a triple quadrupole mass spectrometer (TQ-MS) for the investigation of atmospheric-relevant gas-phase species under medium-pressure conditions. The motivation was to provide a robust soft-ionization alternative to filament-based EI/CI sources, which suffer from extensive fragmentation and limited lifetime in oxygen-containing matrices typical for atmospheric samples. By using a helical resonator to generate a cold hydrogen plasma and by tailoring the plasma chemistry through suitable reagent gas compositions, the HPCI-TQMS was designed to deliver efficient proton transfer and adduct-forming ionization while minimizing fragmentation, thus enabling sensitive detection of aromatic and oxygenated compounds at ambient compositions.

## 5.1 Development and Optimization of the HPCI–TQMS System

A custom-built HPCI source was adapted to a commercial Bruker EVOQ GC-TQ system by replacing its original filament-based EI/CI source, mechanically and vacuum-wise integrated into the existing reaction, lens, and analyzer chamber assembly. The helical resonator operates at 13.56 MHz with input powers below 2 Watt, sustaining a low-temperature, medium-pressure hydrogen plasma in a glass tube directly coupled to the reaction chamber. This configuration provides high densities of primary reagent ions at pressures of 1–15 mbar while maintaining high vacuum ($\leq 10^{-5}$ mbar) in the analyzer region by means of a staged pumping system with a turbomolecular pump and backing pump.

A first key task was to establish controlled formation of defined reactant ions and to stabilize plasma operation over a wide range of pressures and gas compositions. Pure $H_2$ plasma experiments showed that $H_3^+$ is the dominant primary ion (though not directly observable due to the low-mass cut-off), while impurity-derived ions such as $H_3O^+$, $N_2H^+$, and $O_2^+$ grow strongly with increasing plasma source (PS) pressure, as evidenced by mass spectra and optical emission measurements of the Balmer series and $N_2$ second positive emission bands. Introducing small, defined fractions of $N_2$ into $H_2$ produced $N_2H^+$ as a secondary reactant ion via proton transfer from $H_3^+$, with a pronounced maximum in $N_2H^+$ signal at about 9% $N_2/H_2$ mixing ratio for a given total flow. At higher $N_2$ fractions the overall ionization efficiency

decreased, consistent with increasing electron-energy losses in $N_2$ and changes in plasma kinetics.

The reaction chamber geometry and conductance proved to be critical. Initially, a 1.0 mm aperture between reaction and lens chamber led to strong pressure-dependent shifts in reactant distributions and, at higher PS pressure, to dominance of $NH_4^+$ ions originating from heterogeneous $NH_3$ formation on walls and subsequent protonation. Increasing the aperture to 1.5 mm, the pressure regime could be adjusted such that $N_2H^+$ remained the predominant reactant ion at PS pressures around 7.0 – 8.0 mbar while suppressing excessive $NH_4^+$ formation. Systematic variation of plasma gas flow without and with analyte demonstrated that $N_2H^+$ intensity exhibits a maximum at about 5.5 sccm PG without analyte and at a total flow of about 6.5 sccm when 3.0 sccm sample gas is present, corresponding to a reaction chamber pressure of approximately 8.0 mbar.

The spatial configuration between plasma and reaction region was optimized by studying the dependence of reactant and analyte ion intensities on the plasma source distance (PSD) and on the analyte inlet position in the reaction chamber. Increasing the PSD from 100 to 120 mm resulted in losses of up to 90% of $N_2H^+$ and a corresponding reduction in $MH^+$ signals for BTX analytes, highlighting significant wall losses during ion transport through the glass tube. Similarly, moving the analyte capillary away from the intersection with the plasma outflow reduced protonated-ion signals by up to two orders of magnitude, demonstrating that efficient ionization requires both spatial overlap and sufficient reaction time between reactant ions and analyte molecules. Variation of the sample line temperature from 80 °C to 180 °C led to up to 75% decrease in analyte signal intensities at constant flow and pressure, likely due to viscosity-related transport changes. An externally applied repeller potential up to +75 V increased $N_2H^+$ intensities but did not significantly improve $MH^+$ yields, so subsequent measurements were performed with the repeller grounded.

Finally, extensive work was devoted to understanding and minimizing background noise. A key finding was that high-voltage operation of a Penning pressure gauge in the analyzer chamber introduced strong, m/z-independent spikes in the mass spectra, even when ion transmission paths and the detector were physically blocked. Disconnecting the Penning gauge eliminated these spikes, while the Pirani gauge remained benign, leading to the recommendation that the Penning gauge be powered down during analytical measurements. Additional contributions to background were traced to plasma-driven reactions of impurities in

plasma and sample gases and, in dopant-assisted operation, to high-intensity methanol cluster ions.

## 5.2 Ionization Chemistry and Analytical Performance

Using the optimized HPCI conditions with 12% $N_2/H_2$ reagent gas, the ionization behavior of aromatic compounds and oxygenated VOCs was investigated in detail. For BTX (benzene, toluene, o-xylene) in synthetic air, the dominant reactant ions are $N_2H^+$ and $H_3O^+$, while $O_2^+$ and a smaller fraction of $N_2^+$ act primarily as charge-transfer and photoionization partners. Aromatic analytes are ionized via a combination of proton transfer, charge transfer, and VUV photoionization from hydrogen plasma emission. Proton transfer from $H_3O^+$ and $N_2H^+$ proceeds with moderate exothermicity (ΔPA well below typical bond dissociation energies), giving rise to "soft" $MH^+$ spectra, whereas reactions with $H_3^+$, $N_2^+$, $O_2^+$, and VUV photons generate $M^+$ and characteristic fragments such as $M(–H)^+$ and $M(–CH_3)^+$. For toluene, typical distributions of ~25% $MH^+$, ~66% $M^+$, and minor fragments were observed in synthetic air; replacing synthetic air by $N_2$ reduces $O_2^+$-driven charge transfer and $M^+$ formation, but fragmentation channels via $H_3^+$ and $N_2^+$ remain relevant.

For BTX mixtures, the relative contributions of $MH^+$, $M^+$, and $M(–H)^+$ depend sensitively on reaction chamber pressure and thus on total flow. Increasing pressure from 3.5 to about 8.0 mbar increases the fraction of $MH^+$ at the expense of $M(–H)^+$, due to higher $N_2H^+$ and $H_3O^+$ densities and suppressed $N_2^+$ formation, whereas further pressure increase beyond 8 mbar decreases $MH^+$ again because reactant-ion densities decline. At 8.0 mbar, $MH^+$ and $M^+$ signals for BTX are roughly comparable in magnitude, offering a favorable compromise between soft protonation and sensitivity.

In contrast to aromatics, small oxygenated compounds (methanol, ethanol, iso-propanol, n-butanol) could not be measured satisfactorily using $N_2/H_2$ reagent gas alone. Under these conditions, their protonated molecular ions are either not detectable above background, or the spectra are dominated by fragments and overlapping signals from reactant-ions (e.g., $CO_2H^+$, $N_2H^+$). To enable selective and soft ionization of alcohols, a second ionization scheme was introduced in which methanol vapor in synthetic air is used as a dopant/reagent. Primary $H_3^+$ ions from the hydrogen plasma protonate methanol to $CH_3OH_2^+$ and generate methanol clusters $(CH_3OH)_nH^+$ and $(CH_3OH)_n{\cdot}CH_3^+$, whose distributions depend on methanol mixing ratio,

plasma gas flow, and pressure. At percent-level methanol in synthetic air, $CH_3OH_2^+$ and its clusters at m/z 33, 65, 79, and 97 become the dominant reagent population.

Alcohol analytes then react with $CH_3OH_2^+$ and selected clusters via proton transfer and electrophilic addition to form stable adduct ions $M{\cdot}CH_3OH_2^+$ or, in some cases, $M{\cdot}CH_3^+$. For ethanol, the most suitable analytical signal is the adduct at m/z 79, assigned to $CH_3OH{\cdot}C_2H_5OH_2^+$, whose abundance scales linearly with ethanol mixing ratio despite overlay from methanol-cluster background ($(CH_3OH)_3H^+–H_2O$). For iso-propanol and n-butanol, analogous adducts at m/z 93 and 107 are formed, again displaying linear concentration–response behavior. Tandem MS (CID in Q2) at controlled argon pressures and collision energies was used to confirm these structural assignments by demonstrating characteristic loss of $CH_3OH$ and/or $H_2O$ to yield $MH^+$ and typical alkyl fragments. In particular, for n-butanol $CH_3OH{\cdot}C_4H_9OH_2^+$ at m/z 107 produces $MH^+$ at m/z 75 and $M(–OH)^+$ at m/z 57, with fragmentation efficiencies tunable via CID pressure and energy.

The analytical performance was quantified in terms of sensitivity and limits of detection for BTX and alcohols. For BTX analyzed with $N_2/H_2$ reagent gas and evaluated via $MH^+$, sensitivities in full-scan profile mode were on the order of $4.1 - 11 \times 10^3$ cps/ppbV, while in SIM profile mode sensitivities increased by roughly two orders of magnitude up to $2.4 \times 10^5$ cps/ppbV for benzene. Correspondingly, LODs in full scan were in the several-hundred-ppbV range, whereas in SIM mode (centroid data) LODs of 3–7 ppbV were achieved for benzene, toluene, and o-xylene. For alcohols measured with the methanol/air reagent and evaluated via $M{\cdot}CH_3OH_2^+$ adducts, sensitivities in full-scan mode were typically $0.5 - 2.5 \times 10^4$ cps/ppbV, with LODs strongly affected by dopant-related background. Ethanol suffers from spectral interference at m/z 79 and consequently exhibits an LOD in the low-ppmV range in FS mode, whereas iso-propanol and n-butanol can be detected down to single-digit ppbV levels in SIM mode, with n-butanol reaching an LOD of about 4 ppbV.

A systematic background study revealed that electronic noise is comparatively low ($\approx 10^3 - 10^4$ cps level), whereas plasma-induced background from impurities and dopant-related clusters can raise baseline signals to $10^6 - 10^7$ cps at critical m/z values. Under such conditions, noise is dominated by chemical background rather than electronics, and the effective LOD is determined by the stability and reproducibility of this background. For BTX with $N_2/H_2$ reagent gas, background at the $MH^+$ masses remained sufficiently low, enabling ppbV-level detection; for alcohols in methanol-doped mode, careful choice of evaluation m/z

and operating conditions is required to balance reactant-ion intensity against cluster-derived background.

## 5.3 Source Geometry and Outlook

To reduce photoionization artifacts from VUV emission propagating directly from the plasma into the reaction chamber, alternative plasma glass tube geometries (tube-2 and tube-3) were designed and tested. In these configurations, the helical resonator was mounted perpendicular to an axial glass tube, with the aim of removing the plasma glow from the direct line of sight of the reaction chamber and, at the same time, increasing the reaction volume for ion–molecule processes upstream of the chamber. Although these designs indeed reduced direct VUV illumination, they also significantly increased the ion-transport path length along curved glass tubes, leading to substantial wall losses of $N_2H^+$ and a corresponding decrease in $MH^+$ signals. Even with optimized sampling positions and increased reaction lengths, the intensity of protonated toluene obtained with tube-3 remained about 20 times lower than with the original axial tube-1 at comparable pressures, while $M^+$ formation due to residual fluorescence remained non-negligible. In consequence, tube-1 was reinstalled as the standard configuration for most measurements, accepting VUV-induced $M^+$ contributions and controlling them via pressure and plasma-gas optimization.

Overall, this thesis demonstrates that an HPCI source based on a helical hydrogen plasma can be successfully integrated into a triple quadrupole MS and optimized to provide a flexible chemical ionization platform for atmospheric-relevant analytes. With $N_2/H_2$ reagent gas, the system delivers robust protonation and complementary charge-transfer/photoionization channels for aromatic compounds, enabling ppbV-level detection of BTX with soft ionization and tunable fragmentation under SIM operation. With methanol/air dopant as a secondary reagent, the platform is extended to alcohols via stable methanol adduct ions that can be structurally confirmed by tandem MS and exploited for quantitative analysis at low-ppbV levels for multi-carbon alcohols.

Future developments should focus on further decoupling of plasma excitation and reaction regions, for instance by improved optical baffling or alternative plasma geometries that minimize VUV transport while preserving ion flux into the reaction chamber. The use of additional reagent schemes (e.g., tailored dopants with specific proton affinity windows) and

higher-resolution mass analyzers could help to resolve overlapping reagent- and analyte-related peaks, especially in dopant-assisted measurements. Moreover, coupling the HPCI-TQMS to real atmospheric sampling in the field, including humidity- and matrix-tolerant operation, would be a natural next step to fully exploit the potential of the HPCI concept for in-situ studies of atmospheric processes.

# 6 References


(1) Alam, M. S.; Stark, C.; Harrison, R. M. Using Variable Ionization Energy Time-of-Flight Mass Spectrometry with Comprehensive GC×GC to Identify Isomeric Species. *Anal. Chem.* **2016**, *88* (8), 4211–4220. https://doi.org/10.1021/acs.analchem.5b03122.

(2) Ludányi, K.; Dallos, A.; Kühn, Z.; Vékey, K. Mass Spectrometry of Very Large Saturated Hydrocarbons. *Journal of Mass Spectrometry* **1999**, *34* (4), 264–267.

(3) Munson, M. S. B.; Field, F. H. Chemical Ionization Mass Spectrometry. I. General Introduction. *J. Am. Chem. Soc.* **1966**, *88*, 2621–2630.

(4) Newsome, G. A.; Steinkamp, F. L.; Giordano, B. C. Isobutane Made Practical as a Reagent Gas for Chemical Ionization Mass Spectrometry. *J. Am. Soc. Mass Spectrom.* **2016**, *27* (11), 1789–1795. https://doi.org/10.1007/s13361-016-1463-4.

(5) Allan, A. R.; Roboz, J. Neopentane as a Possible Replacement for Isobutane in Chemical Ionization Mass Spectrometry. *Rapid Communications in Mass Spectrometry* **1988**, *2* (11), 235–237. https://doi.org/10.1002/rcm.1290021106.

(6) Hunt, D. F.; McEwen, C. N.; Harvey, T. M. Positive and Negative Chemical Ionization Mass Spectrometry Using a Townsend Discharge Ion Source. *Anal. Chem.* **1975**, *47* (11), 1730–1734.

(7) Schneider, B.; Breuer, M.; Hartmann, H.; Budzikiewicz, H. Chemical Ionization with Aggressive Gases—a Simple Glow Discharge Source for Sector Field Instruments. *Organic Mass Spectrometry* **1989**, *24* (4), 216–218. https://doi.org/10.1002/oms.1210240403.

(8) Bräkling, S.; Kroll, K.; Klee, S.; Benter, T.; Kersten, H. Hydrogen Plasma-Based Medium Pressure Chemical Ionization Source for GC-TOFMS. *J. Am. Soc. Mass Spectrom.* **2022**, *33*, 499–509. https://doi.org/10.1021/jasms.1c00329.

(9) Sackmann, T. Adaption Einer Plasmaionisationsquelle an Ein GC-MS-System. Master thesis, University of Wuppertal, 2021.

(10) Hunter, E. P. L.; Lias, S. G. Evaluated Gas Phase Basicities and Proton Affinities of Molecules: An Update. *J. Phys. Chem. Ref. Data* **1998**, *27* (3), 413–656. https://doi.org/10.1063/1.556018.

(11) Gross, J. H. Mass Spectrometry: A Textbook; Springer International Publishing: Cham, 2017.

(12) Märk, T. D. Fundamental Aspects of Electron Impact Ionization. **1982**, *45*, 125–145.

(13) Bräkling, S. Development of a Dual Ionization Source Time-of-Flight Mass Spectrometer for Gas Chromatography. Ph.D. thesis, Page: 3-5, University of Wuppertal, 2022.

(14) Beckey, H. D. Determination of the Structures of Organic Molecules and Quantitative Analyses with the Field Ionization Mass Spectrometer. *Angew. Chem. Int. Ed.* **1969**, *8* (9), 623–639. https://doi.org/10.1002/anie.196906231.

(15) Lattimer, R. P.; Schulten, H.-R. Field Ionization and Field Desorption Mass Spectrometry: Past, Present, and Future. *Anal. Chem.* **1989**, *61* (21), 1201–1215.

(16) Butcher, D. J. Vacuum Ultraviolet Radiation for Single-Photoionization Mass Spectrometry: A Review. *Microchemical* **1999**, *62*, 354–362.

(17) Eschner, M. S.; Welthagen, W.; Gröger, T. M.; Gonin, M.; Fuhrer, K.; Zimmermann, R. Comprehensive Multidimensional Separation Methods by Hyphenation of Single-Photon Ionization Time-of-Flight Mass Spectrometry (SPI-TOF-MS) with GC and GC×GC. In *Analytical and Bioanalytical Chemistry*; 2010; Vol. 398, pp 1435–1445. https://doi.org/10.1007/s00216-010-4021-0.

(18) Lipok, C.; Uteschil, F.; Schmitz, O. J. Development of an Atmospheric Pressure Chemical Ionization Interface for GC-MS. *Molecules* **2020**, *25* (14), 3253(1)-(14). https://doi.org/10.3390/molecules25143253.

(19) Todd, J. F. J. Recommendations for Nomenclature and Symbolism for Mass Spectroscopy. *Int. J. Mass Spectrom. Ion Process.* **1995**, *142* (3), 211–240. https://doi.org/10.1016/0168-1176(95)93811-F.

(20) Murray, K. K.; Boyd, R. K.; Eberlin, M. N.; Langley, G. J.; Li, L.; Naito, Y. Definitions of Terms Relating to Mass Spectrometry (IUPAC Recommendations 2013). *Pure and Applied Chemistry* **2013**, *85* (7), 1515–1609. https://doi.org/10.1351/PAC-REC-06-04-06.

(21) Hunt, D. F.; Ryan, J. F. Chemical Ionization Mass Spectrometry Studies. I. Identification of Alcohols. *Tetrahedron Lett.* **1971**, *12* (47), 4535–4538. https://doi.org/10.1016/S0040-4039(01)97523-9.

(22) Herman, J. A.; Harrison, Alex. G. Effect of Reaction Exothermicity on the Proton Transfer Chemical Ionization Mass Spectra of Isomeric $C_5$ and $C_6$ Alkanols. *Can. J. Chem.* **1981**, *59* (14), 2125–2132. https://doi.org/10.1139/v81-307.

(23) Lias, S. G.; Liebman, J. F.; Levin, R. D. Evaluated Gas Phase Basicities and Proton Affinities of Molecules; Heats of Formation of Protonated Molecules. *J. Phys. Chem. Ref. Data* **1984**, *13* (3), 695–808. https://doi.org/10.1063/1.555719.

(24) Harrison, A. G. The Gas-Phase Basicities and Proton Affinities of Amino Acids and Peptides. *Mass Spectrom. Rev.* **1997**, *16* (4), 201–217.

(25) *NIST Standard Reference Database Number 69*. https://webbook.nist.gov/chemistry/. https://doi.org/https://doi.org/10.18434/T4D303.

(26) Hunter, E. P. L.; Lias, S. G. Evaluated Gas Phase Basicities and Proton Affinities of Molecules: An Update. *J. Phys. Chem. Ref. Data* **1998**, *27* (3), 413–656. https://doi.org/10.1063/1.556018.

(27) Hartungen, E.; Jürschik, S.; Jordan, A.; Edtbauer, A.; Feil, S.; Hanel, G.; Seehauser, H.; Haidacher, S.; Schottkowsky, R.; Märk, L.; Jaksch, S.; Agarwal, B.; Becker, K.; Mayhew, C. A.; Sulzer, P.; Märk, T. D. Proton Transfer Reaction-Mass Spectrometry: Fundamentals, Recent Advances and Applications. *The European Physical Journal Applied Physics* **2013**, *61* (2), 24303(1)-(6). https://doi.org/10.1051/epjap/2012120401.

(28) Mazzucotelli, M.; Farneti, B.; Khomenko, I.; Gonzalez-Estanol, K.; Pedrotti, M.; Fragasso, M.; Capozzi, V.; Biasioli, F. Proton Transfer Reaction Mass Spectrometry: A Green Alternative for Food Volatilome Profiling. *Green Analytical Chemistry* **2022**, *3 (2022) 100041*, 100041(1)-(15). https://doi.org/10.1016/j.greeac.2022.100041.

(29) Sekimoto, K.; Li, S. M.; Yuan, B.; Koss, A.; Coggon, M.; Warneke, C.; de Gouw, J. Calculation of the Sensitivity of Proton-Transfer-Reaction Mass Spectrometry (PTR-MS) for Organic Trace Gases Using Molecular Properties. *Int. J. Mass Spectrom.* **2017**, *421*, 71–94. https://doi.org/10.1016/j.ijms.2017.04.006.

(30) Holzinger, R.; Joe Acton, W. F.; Bloss, W. W.; Breitenlechner, M.; Crilley, L. L.; Dusanter, S.; Gonin, M.; Gros, V.; Keutsch, F. F.; Kiendler-Scharr, A.; Kramer, L. L.; Krechmer, J. J.; Languille, B.; Locoge, N.; Lopez-Hilfiker, F.; Materi, D.; Moreno, S.; Nemitz, E.; Quéléver, L. L.; Sarda Esteve, R.; Sauvage, S.; Schallhart, S.; Sommariva, R.; Tillmann, R.; Wedel, S.; Worton, D. D.; Xu, K.; Zaytsev, A. Validity and Limitations of Simple Reaction Kinetics to Calculate Concentrations of Organic Compounds from Ion Counts in PTR-MS. *Atmos. Meas. Tech.* **2019**, *12* (11), 6193–6208. https://doi.org/10.5194/amt-12-6193-2019.

(31) Boris M. Smirnov. General Concepts in Physics of Excited and Ionized Gases. In *Fundamentals of Ionized Gases*; WILEY-VCH Verlag GmbH & Co. KGaA, 2011; pp 1–5.

(32) Kenro Miyamoto. Nature of Plasma in Fundamentals of Plasma Physics and Controlled Fusion, 3rd Edt. In *Fundamentals of Plasma Physics and Controlled Fusion*; 2011; pp 1–6.

(33) Lieberman, M. A.; Lichtenberg, A. J. Plasmas and Sheaths in Principles of Plasma Discharges and Materials Processing. In *Principles of Plasma Discharges and Materials Processing*; John Wiley & Sons, Inc., Hoboken, New Jersey., 2005; pp 6–13.

(34) Porter, C. J.; Beynon, J. H.; Ast, T. The Modern Mass Spectrometer—a Complete Chemical Laboratory. *Organic Mass Spectrometry* **1981**, *16* (3), 101–114. https://doi.org/10.1002/oms.1210160302.

(35) Munson, M. S. B.; Field F. H. Reactions of Gaseous Ions. XV. Methane + 1% Ethane and Methane +1% Propane. *J. Am. Chem. Soc* **1965**, *87*, 3294–3299.

(36) Bräkling, S.; Kroll, K.; Stoermer, C.; Rohner, U.; Gonin, M.; Benter, T.; Kersten, H.; Klee, S. Parallel Operation of Electron Ionization and Chemical Ionization for GC-MS Using a Single TOF Mass Analyzer. *Anal. Chem.* **2022**, *94* (15), 6057–6064. https://doi.org/10.1021/acs.analchem.2c00933.

(37) Bräkling, S.; Hinterleitner, C.; Cappellin, L.; Vetter, M.; Mayer, I.; Benter, T.; Klee, S.; Kersten, H. Gas Chromatography Coupled to Time-of-Flight Mass Spectrometry Using Parallel Electron and Chemical Ionization with Permeation Tube Facilitated Reagent Ion Control for Material Emission Analysis. *Rapid Communications in Mass Spectrometry* **2023**, *37* (7), e9461(1)-(11). https://doi.org/10.1002/rcm.9461.

(38) Kroll, K. S. Development of an $H_3^+$ Driven Chemical Ionization Source for GC-MS. Ph.D. thesis, University of Wuppertal, 2021.

(39) Sahling, P. Charakterisierung Helikaler Resonatorspulen Zum Betrieb von Niederdruck Kryptonplasmen Für VUV-Lampen., University of Wuppertal, Wuppertal, 2018.

(40) Haberer, K. B. Befüllung Und Spektroskopische Charakterisierung von VUV Lampen., University of Wuppertal, Germany, 2017.

(41) Kutsch, T. Ionenextraktion Aus Einem Wasserstoffplasma in Einem Helikalen Resonator., University of Wuppertal, Germany, 2017.

(42) *Operating Instruction of TURBOVAC*; Cologne, Germany, 2013.

(43) Pfeiffer Vacuum. *Technical Data in Operating Instruction, PKX*; 2014.

(44) A. Lieberman, M.; J. Lichtenberg, A. *Principles of Plasma Discharges and Materials Processing*, 2nd ed.; John Wiley & Sons, Inc.: New Jersey, 2005.

(45) Niazi, K.; Lichtenberg, A. J.; Lieberman, M. A.; Flamm, D. L. Operation of a Helical Resonator Plasma Source. *Plasma Sources Sci. Technol* **1994**, *3*, 482–495.

(46) Cook, J. M.; Ibbotson, D. E.; Foo, P. D.; Flamm, D. L. Etching Results and Comparison of Low Pressure Electron Cyclotron Resonance and Radio Frequency Discharge Sources. *Journal of Vacuum Science & Technology A: Vacuum, Surfaces, and Films* **1990**, *8* (3), 1820–1824. https://doi.org/10.1116/1.576809.

(47) Niazi, K.; Lichtenberg, A. J.; Lieberman, M. A. *The Dispersion and Matching Characteristics of the Helical Resonator Plasma Source*; 1995; Vol. 23.

(48) Lieberman, M. A.; Lichtenberg, A. J.; Flamm, D. L. *Theory of a Helical Resonator Plasma Source*; University of California at Berkeley, 1990.

(49) Kersten, H. Spark, Helical Resonator and Laser Plasmas, Investigations and Applications. Habilitationsschrift, University of Wuppertal, 2025.

(50) Park, C. J.; Ahn, J. R. A Closed Ion Source with a Cylindrical Repeller for Sensitivity Enhancement in Quadrupole Mass Spectrometry. *Review of Scientific Instruments* **2005**, *76, 044101* (4), 044101(1)-(5). https://doi.org/10.1063/1.1889447.

(51) Microsoft. Microsoft Excel 365.

(52) Dempster, A. J. The Ionization and Dissociation of Hydrogen Molecules and the Formation of $H_3$. *The London, Edinburgh, and Dublin Philosophical Magazine and Journal of Science* **1916**, *31* (185), 438–443. https://doi.org/10.1080/14786440508635520.

(53) Anicich, V. G. *An Index of the Literature for Bimolecular Gas Phase Cation-Molecule Reaction Kinetics*; 2003.

(54) Demtröder, W. *Atoms, Molecules and Photons: The Quantum Structure of Atoms*, 2nd edt.; Springer Berlin Heidelberg: Berlin, Heidelberg, 2010. https://doi.org/10.1007/978-3-642-10298-1.

(55) Amrani, D. Hydrogen Balmer Series Measurements and Determination of Rydberg's Constant Using Two Different Spectrometers. *Eur. J. Phys.* **2014**, *35* (4), 45001. https://doi.org/10.1088/0143-0807/35/4/045001.

(56) Ramachandran, B. R.; Halpern, A. M. The Balmer Spectrum of Hydrogen: An Old Experiment with a New Twist. *Laboratory 1266 Journal of Chemical Education* **1999**, *76* (9), 1266–1268.

(57) Kramida, A.; Ralchenko, Y. *Atomic Spectra Database: NIST Standard Reference Database 78*. https://doi.org/https://dx.doi.org/10.18434/T4W30F.

(58) Fite, W. L.; Rutherford, J. A.; Snow, W. R.; Van Lint, V. A. J. Ion-Neutral Collisions in Afterglows. *Discuss. Faraday Soc.* **1962**, *33*, 264–272. https://doi.org/10.1039/df9623300264.

(59) Plemmons, D. H.; Parigger, C.; Lewis, J. W. L.; Hornkohl, J. O. Analysis of Combined Spectra of NH and $N_2$. *Appl. Opt.* **1998**, *37* (12), 2493–2498. https://doi.org/10.1364/AO.37.002493.

(60) Kim, J. K.; Theard, L. P.; Huntress, W. T. Reactions of Excited and Ground State H3+ Ions with Simple Hydrides and Hydrocarbons: Collisional Deactivation of Vibrationally Excited $H_3^+$ Ions. *International Journal of Mass Spectrometry and Ion Physics* **1974**, *15* (3), 223–244. https://doi.org/10.1016/0020-7381(74)85001-1.

(61) Carrasco, E.; Jiménez-Redondo, M.; Tanarro, I.; Herrero, V. J. Chemistry in Low-Pressure Cold Plasmas: Ions of Astrophysical Interest. *Plasma Phys. Control. Fusion* **2012**, *54* (12), 124019(1)-(6). https://doi.org/10.1088/0741-3335/54/12/124019.

(62) Carrasco, E.; Jiménez-Redondo, M.; Tanarro, I.; Herrero, V. J. Neutral and Ion Chemistry in Low Pressure Dc Plasmas of $H_2/N_2$ Mixtures: Routes for the Efficient Production of $NH_3$ and $NH_4^+$. *Physical Chemistry Chemical Physics* **2011**, *13* (43), 19561–19572. https://doi.org/10.1039/c1cp22284h.

(63) DeMonchy, A. R.; Oskam, H. J. Production and Loss of $N_2^+$ Ions during the Decay Period of Plasmas Produced in Helium-Nitrogen Mixtures. *Zeitschrift für Physik* **1969**, *224* (4), 324–334. https://doi.org/10.1007/BF01393060.

(64) Bai, K. H.; Lee, D. S.; Chang, H. Y.; Uhm, H. S. Control and Analysis of Ion Species in $N_2$ Inductively Coupled Plasma with Inert Gas Mixing. *Appl. Phys. Lett.* **2002**, *80* (21), 3907–3909. https://doi.org/10.1063/1.1479452.

(65) Hemsworth, R. S.; Payzant, J. D.; Schiff, H. I.; Bohme, D. K. Rate Constants at 297°K for Proton Transfer Reactions with $NH_3$. Comparisons with Classical Theories and Exothermicity. *Chem. Phys. Lett.* **1974**, *26* (3), 417–421. https://doi.org/https://doi.org/10.1016/0009-2614(74)89061-5.

(66) Milligan, D. B.; Wilson, P. F.; Freeman, C. G.; Meot-Ner (Mautner), M.; McEwan, M. J. Dissociative Proton Transfer Reactions of $H_3^+$, $N_2H^+$, and $H_3O^+$ with Acyclic, Cyclic, and Aromatic Hydrocarbons and Nitrogen Compounds, and Astrochemical Implications. *Journal of Physical Chemistry A* **2002**, *106* (42), 9745–9755. https://doi.org/10.1021/jp014659i.

(67) Wright, P. G. The Variation of Viscosity with Temperature. *Phys. Educ.* **1977**, *12* (5), 323–325. https://doi.org/10.1088/0031-9120/12/5/012.

(68) Spanel, P.; Smith, D. Mass Spectrometry and Ion Processes SIFT Studies of the Reactions of $H_3O^+$, $NO^+$ and with a Series of Alcohols. *Int. J. Mass Spectrom. Ion Process.* **1997**, *167*, 375–388.

(69) Spanél, P.; Smith, D. Reactions of Hydrated Hydronium Ions and Hydrated Hydroxide Ions with Some Hydrocarbons and Oxygen-Bearing Organic Molecules. *J. Phys. Chem* **1995**, *99*, 15551–15556.

(70) Sung Leei, H.; Drucker, M.; Adams, N. G. Thermal Energy Reactions of $H_3^+$ and $H_3O^+$ with a Series of Small Organic Molecules. *Int. J. Mass Spectrom. Ion Process.* **1992**, 101–114.

(71) Spanel, P.; Pavlik, M.; Smith, D. Reactions of $H_3O^+$ and OH-Ions with Some Organic Molecules; Applications to Trace Gas Analysis in Air. *Int. J. Mass Spectrom. Ion Process.* **1995**, *145*, 177–186.

(72) Blanksby, S. J.; Ellison, G. B. Bond Dissociation Energies of Organic Molecules. *Acc. Chem. Res.* **2003**, *36* (4), 255–263. https://doi.org/10.1021/ar020230d.

(73) Lippert, E. The Strengths of Chemical Bonds, von T. L. Cottrell. Butterworths Publications Ltd., London 1958. 2. Aufl., X, 317 S., Geb.t—/32/—. *Angewandte Chemie* **1960**, *72* (16), 602–602. https://doi.org/10.1002/ange.19600721618.

(74) Španěl, P.; Smith, D. A Selected Ion Flow Tube Study of the Reactions of $NO^+$ and $O_2^+$ Ions with Some Organic Molecules: The Potential for Trace Gas Analysis of Air. *Journal of Chemical Physics* **1996**, *104* (5), 1893–1899. https://doi.org/10.1063/1.470945.

(75) Lyman, T. The Spectrum of Hydrogen in the Region of Extremely Short Wave-Lengths. *Astrophys. J.* **1906**, *23*, 181–220. https://doi.org/10.1086/141330.

(76) Luo, Y.-R. *Comprehensive Handbook of Chemical Bond Energies*; CRC Press, 2007. https://doi.org/10.1201/9781420007282.

(77) Anicich, V. G. Evaluated Bimolecular Ion-Molecule Gas Phase Kinetics of Positive Ions for Use in Modeling Planetary Atmospheres, Cometary Comae, and Interstellar Clouds. *J. Phys. Chem. Ref. Data* **1993**, *22* (6), 1469–1569. https://doi.org/10.1063/1.555940.

(78) Nordstrom, R. J.; Chan, W. H.; Phys Chem, J.; Smith, R. D.; Futrell, J. H. Reaction of $N_2H^+$ with Methanol. Internal Energy Effects in Proton Transfer Reactions. *J. Phys. Chem.* **1977**, *81* (3), 195–198.

(79) Rohrbaugh, D. K. Methanol Chemical Ionization Quadrupole Ion Trap Mass Spectrometry of O-Ethyl S-[2-(Diisopropylamino)Ethyl] Methylphosphonothiolate (VX) and Its Degradation Products. *J. Chromatogr. A* **2000**, *893* (2), 393–400. https://doi.org/10.1016/S0021-9673(00)00752-4.

(80) Schubert, A. J.; Enke, C. G. Methanol Chemical-Ionization Mass Spectrometry for the Determination of Polar Compounds in Fuels. *Anal. Chim. Acta* **1988**, *211*, 83–89. https://doi.org/10.1016/S0003-2670(00)83670-3.

(81) Pal, J.; Patla, A.; Subramanian, R. Thermodynamic Properties of Forming Methanol-Water and Ethanol-Water Clusters at Various Temperatures and Pressures and Implications for Atmospheric Chemistry: A DFT Study. *Chemosphere* **2021**, *272*, 129846(1)-(12). https://doi.org/10.1016/j.chemosphere.2021.129846.

(82) Munson, M. S. B. Reactions of Gaseous Bronsted Acids. *J. Am. Chem. Soc.* **1965**, *87* (23), 5313–5317. https://doi.org/10.1021/ja00951a009.

(83) Ewing, R. G.; Eiceman, G. A.; Stone, J. A. Proton-Bound Cluster Ions in Ion Mobility Spectrometry. *Int. J. Mass Spectrom.* **1999**, *193*, 57–68.

(84) Mi, D.; Xu, J.; Zhang, Y.; Zhu, T.; Ouyang, J.; Dong, X.; Chingin, K. Formation of Protonated Water–Hydrogen Clusters in an Ion Trap Mass Spectrometer at Room Temperature. *Physical Chemistry Chemical Physics* **2022**, *24* (12), 7180–7184. https://doi.org/10.1039/D1CP04516D.

(85) Kawai, Y.; Yamaguchi, S.; Okada, Y.; Takeuchi, K.; Yamauchi, Y.; Ozawa, S.; Nakai, H. Reactions of Protonated Water Clusters $H^+(H_2O)$ (N=1–6) with Dimethylsulfoxide in a Guided Ion Beam Apparatus. *Chem. Phys. Lett.* **2003**, *377* (1–2), 69–73. https://doi.org/10.1016/S0009-2614(03)01095-9.

(86) Yost, R. A.; Enke, C. G. Selected Ion Fragmentation with a Tandem Quadrupole Mass Spectrometer. *J. Am. Chem. Soc.* **1978**, *100* (7), 2274–2275. https://doi.org/10.1021/ja00475a072.

(87) Yu, T.-Y.; Cheng, T. M. H.; Kempter, V.; Lampe, F. W. Ionic Reactions in Monosilane. Radiation Chemistry Implications. *J. Phys. Chem.* **1972**, *76* (23), 3321–3330. https://doi.org/10.1021/j100667a005.

(88) de Hoffmann, E. Tandem Mass Spectrometry: A Primer. *Journal of Mass Spectrometry* **1996**, *31* (2), 129–137. https://doi.org/https://doi.org/10.1002/(SICI)1096-9888(199602)31:2<129::AID-JMS305>3.0.CO;2-T.

(89) Langner, M. Investigation of the Mechanism Causing Baseline Shift in Single Stage Quadrupole Mass Spectrometers. Ph.D thesis, University of Wuppertal, 2023.